Computational mining of meso-scale physics from high-energy X-ray data sets

by

Siddharth Maddali

Submitted in partial fulfillment of the
requirements for the degree of
Doctor of Philosophy
at
Carnegie Mellon University
Department of Physics
Pittsburgh, Pennsylvania

Advised by Professor Robert M. Suter

Abstract

Migration of grain boundaries in an idealized, well-ordered polycrystalline sample is an often-studied phenomenon in microstructural materials science. It is the subject of many imaging experiments in two dimensions and simulations in two and three dimensions, the collective knowledge of which has given us many insights into behavior of specific materials. This thesis describes the characterization of the grain boundaries in a specially prepared polycrystalline aggregate of high-purity iron with a body-centered cubic lattice whose microstructure was imaged non-destructively in three dimensions with near-field high-energy diffraction microscopy (nf-HEDM) which uses synchrotron X-rays as a probe. The sample was imaged using nf-HEDM before and after a cycle of annealing in order to activate boundary migration for a short interval of time. Also described are the development of computational techniques for denoising grain boundary images in three dimensions as well as a scheme to solve the inverse problem of computing the dynamical parameters influencing boundary migration from the observed boundary geometries and transport. The two snapshots of the full three-dimensional grain boundary network were used to quantify the geometry and transport of individual grains and track their progress through the annealing. A study of the influence of grain boundary curvature on boundary velocity revealed a weak correlation for a large fraction of the boundaries.

Acknowledgments

I would first like to thank the members of my multi-disciplinary thesis committee, namely Dr. Robert Suter and Dr. Michael Widom of the Department of Physics, Dr. Shlomo Ta'asan of the Department of Mathematical Sciences and Dr. Anthony Rollett of the Department of Materials Science and Engineering for agreeing to be a part of it, providing valuable feedback and engaging in many riveting discussions over the years. It has truly been a pleasure to address a specific scientific problem from the experimental, theoretical and computational points of view under their guidance. Special thanks to my advisor Dr. Suter for the opportunity to work with him on this intriguing problem and the opportunity to meet many highly skilled and talented people in the process, as well as his enduring patience with an absolute beginner in the trade.

I would also like to thank Ulrich Lienert, Jonathan Almer, Peter Kenesei, Jun-Sang Park and Ali Mashayekhi at the Advanced Photon Source at Argonne National Laboratory for their invaluable assistance regarding the use of the onsite X-ray imaging apparatus. The long hours without proper food or sleep would have all been for nought had it not been for their support. In this regard I am also extremely thankful to my friend, colleague and office-mate David Menasche, for being an indispensable part of the data collection process and also the many highly interesting and entertaining conversations (talking shop and banter included) over the course of four years. I thank also the former members of Dr. Suter's research group, Christopher Hefferan, Jonathan Lind, Reeju Pokharel and Xi Tan who patiently guided me as I was starting out, both with the experiment at the APS as well as the esoteric computational tools developed in the group, the mastery of which is indeed a rite of passage; particularly Chris and Reeju for training me on the tube furnace; former post-docs in the group Euan Wieliewski and Patrick Callaghan; current group member Rulin Chen, who now carries forward the expertise of high-energy diffraction microscopy.

With regards to the preparation of the high-purity iron sample and an earlier aluminum alloy sample, I would like to sincerely thank friends over at the MSE department, particular Bill Pingitore and Adam Wise for the sample preparation, the rolling mill and the Vickers hardness testers, etching and polishing; Clayton Stein, Brian Lin, Stephanie Bojarski and Patrick Callahan for help with the scanning electron microscope.

I'd also like to thank Loïc Renversade at École des Mines de Saint-Étienne, whose brief summer stint with us was academically productive and great fun as well.

On to the various driving forces in my life, first and foremost my wife Ranjini who has shared the tumultuous experience of this last stage of formal education from 700 miles away in Atlanta and has been the pillar against which I have propped up my tired mind every now and then over the last 6 years; my family in Bangalore, India, starting with my parents Vivekanand and Lakshmi, who are the biggest sources of inspiration in my life, scientific or otherwise, whose unwavering support and guidance

Contents

List of Tables

List of Figures

Chapter 1

Introduction

1.1 Background

The relationship between the structure and properties of solids has been a never-ending source of curiosity ever since matter was discovered to consist of a variety of atoms. Every area of science and technology owes the march of its progress either directly or indirectly to at least one solid whose atomic structure serves a very specific purpose. The quest to understand (and consequently exploit) the properties of solids has consistently been responsible for improving our quality of life ever since humans started using tools and implements and has inevitably spawned terminology that has since passed into common parlance: the science of the solid state. Applications of solids with crystalline structure (a regular arrangement of constituent atoms over significant distances in space), in particular metals, being abundant in nature, have seen multiple eventful eras of frenzied research and development. These periods are characterized by technology and entire economies advancing by leaps and bounds (the Industrial Revolution in the United Kingdom and the attendant innovations in metallurgy that saw the technological rise of Europe; the steel boom in Pittsburgh, Pennsylvania, USA) and are sometimes literally named for the material in question (*e.g.* the Bronze and Iron Ages; the long-sustained explosion of the micro-electronics industry originating in Silicon Valley, California, USA).

At the heart of solid state physics, then, is the general understanding that material configurations in which atomic positions are regularly spaced are energetically favorable compared to disordered positioning. There is a rich and well-documented phenomenology of material properties due to disruptions in this atomic regularity that has spawned avenues of theoretical inquiry not only in materials engineering and physics at various length scales, but in mathematics as well, with the geometric modeling of regular lattices and characterization of these crystalline 'defects' and 'dislocations' being an intricate field in itself. Further, a beautiful visual manifestation of regular atomic positions and the sporadic irregularities therein is seen in the exper-

imental method of choice in this thesis: a unique microscopy technique that makes use of the phenomenon of X-ray diffraction. The technique, the 'near-field' variant of high-energy diffraction microscopy (nf-HEDM), is one of a few novel techniques riding the current wave of third- and fourth- generation synchrotron sources that are capable of producing directed electromagnetic radiation of high energy and monochromaticity, and extremely high brilliance by accelerating charged particles through strong magnetic fields. nf-HEDM uses these high-energy photons as a non-destructive probe to query the structure of crystalline materials at the appropriate length scale. The usefulness of X-rays as a probe for material lattice structures stems from the nominal wavelength of the X-rays being of the order of the spacing between the atomic planes in the crystalline lattice (~ 0.1Å). A more detailed discussion of X-ray diffraction and the nf-HEDM technique is deferred to Chapter 2. A dedicated experimental setup for nf-HEDM is located at the Advanced Photon Source in Argonne national Laboratory, near Chicago, IL.

The research presented in this thesis focuses on the phenomenology of crystalline materials in what is known as the meso-scale regime, whose characteristic length scales can range from that of large groups of constituent atoms ($\sim 10^{-5}$mm) to about the thickness of a human hair (~ 0.08mm). Further, this research is focused on a particular type of crystalline defect in which the regularity of the lattice is broken along an interface inside the bulk of the solid. The presence of the interface is indicated by a region around it in which atoms are not in their regular lattice positions and therefore represents a higher energy configuration of the material lattice. The interface delineates regions of the crystal structure which are differently oriented with respect to each other. When these interfaces border other interfaces in the material bulk they form an interface network akin to a soap bubble foam that partitions regions of the material into distinct volumes, each with its own crystallographic orientation with respect to its neighbors. These volumes are known in materials science literature as **grains** and the interfaces as **grain boundaries**. The sample is said to be in the polycrystalline state. Grain boundaries are distinguished from interfaces on the edges of a sample in which atoms in a particular crystallographic orientation meet a free surface, the latter being fundamentally different in a thermodynamic sense. Grain boundaries are by definition found in the bulk of a material. The study of grain boundaries is of great interest in industrial applications as well as basic science since their presence can alter physical properties of a material like thermal and electrical conductivity, hardness and susceptibility to deformation. Techniques like grain boundary engineering seek to manipulate material properties for specific purposes.

Our interest in grain boundaries lies in the manner in which a sample with no excess source of lattice energy other than the presence of grain boundaries (a 'well-ordered' sample in a crystallographic sense) achieves a minimum energy configuration through an activated external stimulus (namely, annealing treatment in an inert atmosphere).

The mechanism of said energy minimization is the migration of boundaries through the sample during annealing, which is actually caused by energetically activated atoms in lattice positions corresponding to one side of a grain boundary switching to lattice positions on the other side of the boundary. On migration of boundaries in a sample, some grains shrink in favor of others growing, a phenomenon generally termed as 'grain coarsening'. This process continues on continued activation until there are no grain boundaries in the sample *i.e.* it has attained the lowest-energy 'single crystal' configuration. The migration of grain boundaries has been modeled in simple terms since the days of John von Neumann and countless simulations have been performed of simplified configurations using different dynamic models. Even so, the phenomenon of coarsening is ill-understood in terms of fundamental physics owing to (1) the lack of non-destructive imaging techniques of a grain boundary network before and after differential migration and (2) the enormous complexity of modeling an entire network of grain interfaces in a sample without full knowledge of the nature of the interfacial free energy and the nontrivial effect of grain boundary geometry.

It is the aim this thesis to characterize to a high experimental resolution a polycrystalline aggregate with a large number of grain boundary network elements and hopefully extract meaningful information about the driving forces of grain coarsening. This is achievable by harnessing the sophistication of non-destructive imaging techniques such as nf-HEDM, the prerequisite of *non-destructive* being crucial to measuring migration of boundaries. This is contrasted to a destructive technique such as electron back-scatter diffraction (EBSD), a surface measurement in which grain are imaged one planar cross-section at a time by alternate imaging and grinding away. Complementing the measurement is the development of sophisticated computational techniques capable of mining useful information about grain boundary geometry and transport during migration. We develop an optimization-based technique to solve the inverse problem of computing interfacial energy and boundary mobility given the (filtered) geometry and transport of individual grain boundaries. This last project involves the development of a generalized theory of interface migration, which is the content of Chapter 5.

1.2   Motivation

The goals of this thesis are multifold:

1. To develop and validate generalized models for the behavior of interface ensembles in samples of well-ordered polycrystalline material, with the eventual aim of obtaining sophisticated computational schemes to quantify interface dynamics.

2. To utilize the development of sophisticated synchrotron-based imaging techniques that make use of high-energy beam probes with improving resolution capabilities in order to *non-destructively* obtain high-quality microstructure data

3

from real material samples, particularly *ex situ* measurements that permit the imaging of migrating boundaries in three dimensions in a manner that would have not been possible otherwise.

3. Complementary to the above, to leverage the immense power of high-performance computing resources in order to analyze mathematically the microstructure data to eventually attain a better understanding of bulk interface phenomenology.

In trying to achieve these goals, this thesis touches upon experimental, theoretical and computational aspects.

1.3   Outline

This thesis is organized in the following manner: Chapter 2 describes the material chosen for study (α-iron with a BCC crystal lattice), the properties of the sample at the time of acquisition and the subsequent processing in order to tailor it to our precise requirements and generate a polycrystalline sample suitable for imaging with high-energy X-rays. It also describes in brief the intermediate annealing routine to which the sample was subjected in order to coarsen the grains. Following a brief primer of scattering physics and the principles of crystallography, the chapter goes on to describe the non-destructive imaging technique itself (near-field high-energy diffraction microscopy), that spatially resolves the orientation field of the material up to sub-degree resolution from hundreds of gigabytes of diffraction data, a massive computational task that requires the resources of advanced supercomputing facilities around the country. The chapter details in particular the post-acquisition processing of the data collected during the experiment, which takes typically over the span of a few days at the Advanced Photon Source (APS) at Argonne National Laboratory. This post-processing, which involves signal extraction from the noisy detector data and a forward modeling algorithm that exhaustively searches the space of crystal orientations and pieces together the digital three-dimensional image of the sample orientation field, layer by layer, by matching simulated diffraction to observed signal, is achieved using in-house parallel computing code written in C++. Chapter 3 gives the mathematical basis of an assortment of computational techniques used in the afore-mentioned post-processing, as well as some refining techniques applied to the high-resolution orientation images of the sample in order to quantify boundary geometry and migration in a consistent and automated manner.

One of these techniques is a novel surface smoothing algorithm, the typical preserve of computer vision engineers, that is specially tailored to an imaged three-dimensional network of grain boundaries. The technique, called 'hierarchical smoothing' in reference to its ability to classify the topological elements of a grain boundary network into an intuitive ranking system and smooth them in order while heeding the boundary

constraints obeyed by each, comprises a submitted manuscript and is the entire focus of Chapter 4.

Chapter 5 introduces in exhaustive detail a numerical scheme to compute the grain boundary interfacial energy and mobility from local geometry and transport information of the imaged network of grain boundaries (the geometry being obtained from the hierarchical smoothing algorithm). The chapter begins with the fundamental theory of interface migration and describes using variational principles the derivation of a dynamic equation that links the migration of a single boundary to the interfacial energy density and mobility, expressed in a tractable subspace of grain boundary parameter descriptors. The numerical discretization of this equation and its solution for a select ensemble of observed grain boundaries in a sample (namely, those of the same disorientation) is described, as the solution to a generalized eigenvalue problem. The rest of the chapter is dedicated to the resolution of the various attendant issues that arise with the numerical discretization, such quantification of boundary transport given before- and after-migration of snapshots of a grain boundary, the ramifications of applying crystal symmetry to the space of grain boundaries and an elegant scheme to perform calculus and interpolation on the subspace thus obtained.

Chapter 6 discusses experimental results pertaining to the imaged volume of α-iron before and after the annealing cycle. On the imaging side, the number of Bragg peaks per point in the sample space is estimated, this quantity being a measure of how reliable an obtained sample reconstruction is. The appearance of possible voids in the sample image due to fracture yield is discussed. A good portion of the chapter is dedicated to the measurement of bulk statistics of the material microstructure and how the anneal possibly influences them. This includes qualitative descriptions of the texture and the grain boundary character distributions, the latter being of particular interest when juxtaposed with accepted knowledge of the grain boundary energy distributions as obtained from earlier simulation works. The chapter considers the set of grains and grain boundaries tracked between the anneal states and the computations that become possible thereby, namely the correlation coefficients between the local curvatures and normal velocities to test for closeness to the simple von Neumann-Mullins model of grain boundary motion. In addition, the results of two proof-of-concept validations of the coarsening theory and numerical technique of Chapter 5 is presented, these last two items still being a work in progress.

Chapter 7 briefly summarizes the results described in Chapter 6 and point to future work that is necessary to close the loop between the experimental observations and the theoretical approach described in chapter 5.

Chapter 2

Sample preparation and the experiment

The computational tools developed in the bulk of this thesis require as input the appropriate microstructure geometry data before and after material processing. In order to demonstrate the feasibility of these computational techniques on real-world microstructures a variety of issues had to be addressed on the experiment/data acquisition side of things, ranging from the choice of material to its initial and intermediate heat treatment and the manner of imaging of its microstructure. Each of these is addressed in detail in this chapter. We describe in order the following things:

1. The choice of polycrystalline material and the necessary pre-processing in order to ready it for imaging.

2. The intermediate process of annealing in order to change the microstructure differentially.

3. A brief description of the mathematics of scattering and how it informs the imaging technique, namely the near-field variant of high-energy diffraction microscopy (nf-HEDM).

4. The procedure to spatially resolve the orientation field of the polycrystalline solid from the collected diffraction data.

2.1 Sample preparation and processing

The choice of material was motivated by ease of availability and preparation, as well as high crystallographic symmetry, even though the computational methods developed in subsequent chapters are generally applicable to polycrystals of all symmetries. 'Preparation' here stands for the creation of a grain structure with a relatively uniform boundary inclination distribution, followed by the machining of a piece of the

material to dimensions suitable to the nf-HEDM imaging experiment. The sample of choice was electrolytically grown high-purity iron (obtained from Center for Iron and Steelmaking Research at Carnegie Mellon University) and with an elongated grain structure. At temperatures below 912°C, iron exists in its α-allotropic form, which has a body-centered cubic (BCC) crystal structure [1], a fact that could not be ignored when choosing a suitable annealing schedule for the sample.

The requirement of (statistically) isotropic grain boundary inclinations required the destruction of the elongated grain structure followed by regrowth through metallurgical annealing and quenching. Accordingly the sample was rolled in a mill from an original thickness of about 5 mm to about 1 mm and annealed in a tube furnace for 2 hours at 600°C in an atmosphere of forming gas ($N_2 + 3\% H_2$) and then quenched. The N_2 component provides an inert atmosphere while the H_2 prevents any residual oxidation at the surface of the sample, to which α-iron is particularly susceptible. This annealing step (determined by trial and error) caused recovery and recrystallization of the microstructure to give new grains that were relatively more spherical in shape than that of the rolled grains. It was anticipated that the anneal would at least partially remove the incurred crystallographic texture of the plastically deformed grains due to the rolling. The results of an investigation into this as well as the 'shape' texture of the grains (*i.e.* preferential elongation along the rolling direction and how it changes with annealing) are described in Chapter 6. A key goal of the sample preparation was to grow a large population of grains in order to obtain a satisfactory number of grain boundaries. The grains were ascertained to be sufficiently isotropic by imaging two mutually perpendicular surface planes in a piece of the sample that was rolled and then annealed (Figure 2.1).

The sequence of preparation of the final sample (to be taken to the APS) is shown in Figure 2.2. This sample was annealed at 600°C for 2 hours.

2.2 Near-field high-energy diffraction microscopy

Nondestructive techniques for imaging materials using high-energy X-rays ($30\text{keV} - 100\text{keV}$) owe their development to the advent of synchrotron facilities that generate intense beams of high-energy photons by accelerating bunches of ultra-relativistic electrons through magnetic insertion devices. Imaging techniques vary depending on whether the entire spectrum of this synchrotron radiation ('white beam') is being used or only radiation belonging to a narrow range of wavelengths, with each being suitable for different experiments. The technique known as high-energy diffraction microscopy belongs to the latter family, along with sister techniques such as diffraction contrast tomography[2, 3]. Owing to the monochromaticity of the incident radiation, these techniques rely on capturing of scattered X-rays at very specific sample orien-
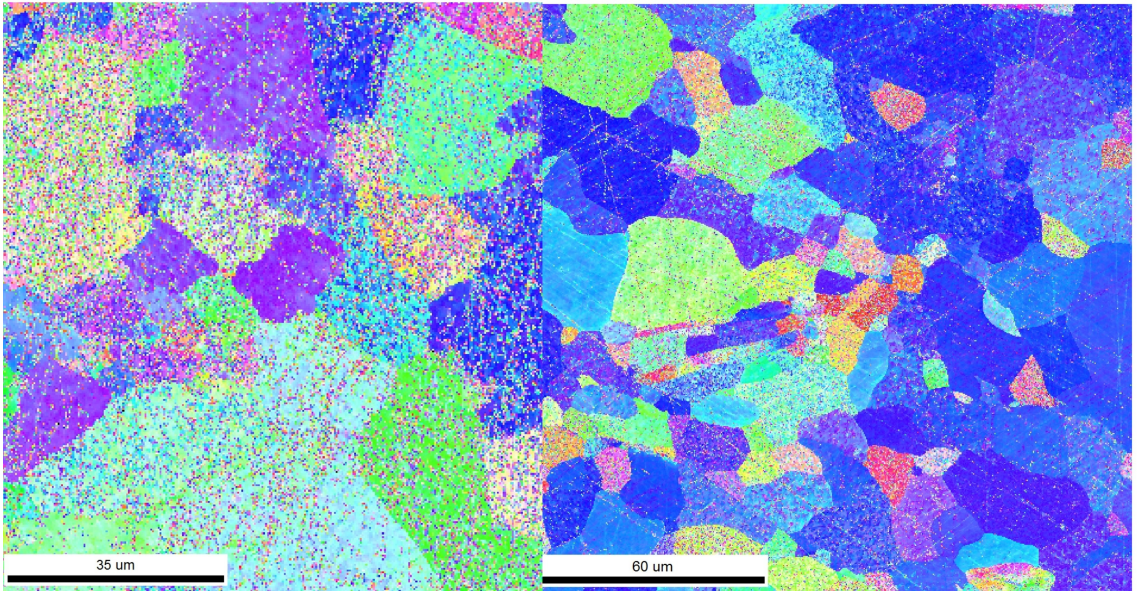
Figure 2.1: EBSD images of two mutually perpendicular surfaces of the rolled and annealed iron, showing grain sizes roughly the same in both cases.

(a) (b) (c)
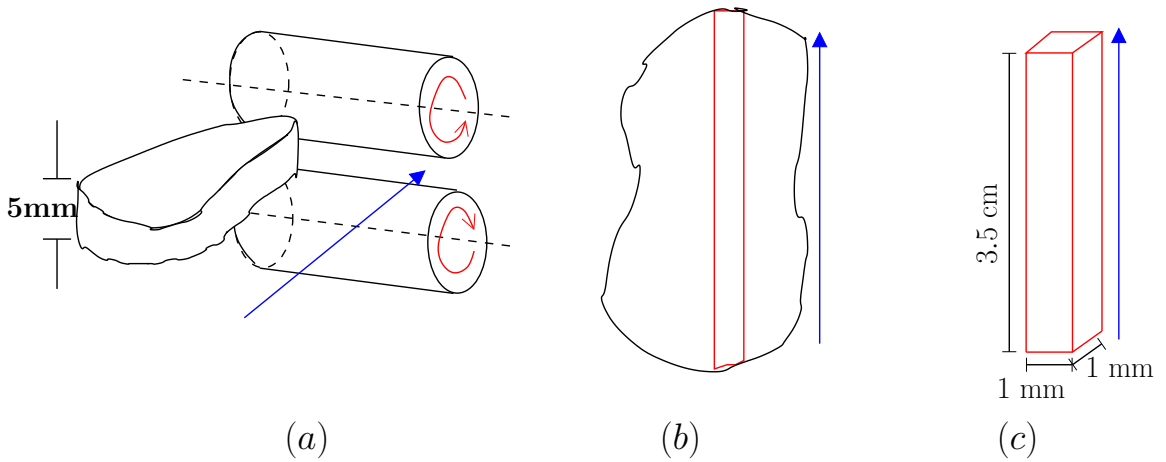
Figure 2.2: **(a)** Raw sample rolled in a mill; **(b)** Long piece cut out of the rolled sample; **(c)** Approximate final dimensions of the cut and ground piece. The rolling direction is shown as a blue arrow in all three images.

8

tations with respect to the beam (according to Bragg's law, explained presently) and therefore subsequent investigation of material structure from the diffraction data is usually an intricate task involving understanding the complex interplay of the experimental geometry with the material crystallography. This section describes briefly the nf-HEDM technique, beginning with the basics of scattering physics and crystallography followed by the geometric conditions for diffraction and by a description of the experimental setup and geometry. We close with a brief description of image processing techniques implemented to denoise the area detector images and finally the forward modeling method of determining crystal orientations. For a more thorough description of the nf-HEDM experiment, the reader is referred to the PhD theses of Li [4], Hefferan [5] and Lind [6], as well as the works of Lienert *et al.* [7] and Li *et al.* [8].

2.2.1   Scattering physics

Diffraction as a tool for imaging structure is predicated upon elastic scattering of the sufficiently coherent incident wave by the regular array of atomic scatterers in a lattice. We discount in the following treatment inelastic scattering of X-rays in which the energy of each outgoing photon is different from that of the incoming photon. Inelastic X-ray scattering from solids involves the target atoms transitioning between electronic energy states and as such the incoming and outgoing photons do not have a geometrically consistent phase relationship. As a result, inelastic scattering is incoherent and unsuitable for diffraction experiments that probe lattice structure (it is more suited to probing of electronic and phononic band structures). It is in fact a source of detector noise.

At the root of elastic scattering theory (whether classical or quantum mechanical) is the Helmholtz equation $\left(\nabla^2 + k^2\right)\Phi(\boldsymbol{x}) = \widetilde{\rho}(\boldsymbol{x})$ which is describes the behavior of an incident plane wave denoted by the field $\Phi(\boldsymbol{x})$ interacting with a scatterer whose spatial distribution is given by $\widetilde{\rho}(\boldsymbol{x})$. In the realm of classical electromagnetics, $\Phi(\boldsymbol{x})$ can be the components of an electromagnetic field and $\widetilde{\rho}(\boldsymbol{x})$ a charge distribution, say an electron cloud. The mathematical formalism of X-ray diffraction has its roots in modeling the scattering off of a point scatterer ($\widetilde{\rho}(\boldsymbol{x})$ is a delta function) at a distance much greater than the dimensions of the scatterer (known as the 'radiation zone' in classical electromagnetic theory). The solution to the free-boundary Helmholtz equation in this regime can be approximated to a good degree by a spherical wave emanating from the point scatterer. What follows is the simplified treatment of scattering as described by Warren [9]. The optical path length in the presence of a point scatterer and hence phase difference $e^{ik\Delta x}$ can be calculated using Figure 2.3 as

Figure 2.3: Plane wave with wave vector $\boldsymbol{k}_i$ interacting with a point scatterer at position $\boldsymbol{x}'$ relative to the origin O. The phase of the wave at a position $\boldsymbol{x}$ can be computed from the optical path length Δx from the origin through the position of the scatterer to the final point of observation ($x \gg x'$ and $k_f = k_i$ because of elastic scattering)
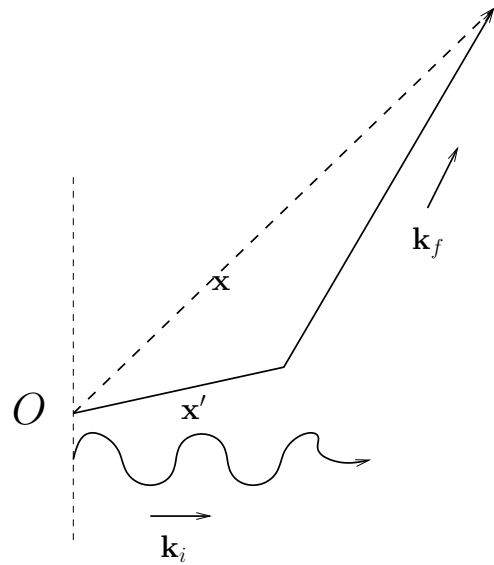
a reference:

$$\Delta x = \boldsymbol{x}' \cdot \hat{\boldsymbol{k}}_i + \left[x'^2 + x^2 - 2\boldsymbol{x} \cdot \boldsymbol{x}' \right]^{1/2}$$
$$\implies k\Delta x \simeq \boldsymbol{x}' \cdot \boldsymbol{k}_i + kx - \boldsymbol{k}_f \cdot \boldsymbol{x}'$$
$$= kx - \boldsymbol{q} \cdot \boldsymbol{x}' \qquad\qquad (\boldsymbol{q} = \boldsymbol{k}_f - \boldsymbol{k}_i)$$
$$e^{ik\Delta x} = e^{i(kx - \boldsymbol{q} \cdot \boldsymbol{x}')} \tag{2.1}$$

The correction to the amplitude of the wave scattered by the atoms of a real-world material is modeled by adding up these phase differences for an array of such point scatterers placed at the points of a Bravais lattice, and whose *identical* scattering centers are not point charges, but are positionally delocalized according to a probability density $\widetilde{\rho}(\boldsymbol{x}')$. If the periodic lattice positions are given by the set of vectors $\mathbf{R}_i$, then density field of each atomic scatterer i is $\widetilde{\rho}(\boldsymbol{x}' - \mathbf{R}_i)$ and the multiplicative factor for the amplitude of the scattered wave at position $\boldsymbol{x}$ is:

$$\sum_n \int_{\mathbb{R}^3} d^3x' \; e^{i(kx - \boldsymbol{q} \cdot \boldsymbol{x}')} \widetilde{\rho}(\boldsymbol{x}' - \mathbf{R}_n) \tag{2.2}$$

$$= e^{ikx} \underbrace{\sum_n e^{-i\boldsymbol{q} \cdot \mathbf{R}_n}}_{\text{structure factor}} \underbrace{\int_{\mathbb{R}^3} d^3y' \; e^{-i\boldsymbol{q} \cdot \boldsymbol{y}'} \widetilde{\rho}(\boldsymbol{y}')}_{\text{form factor}}$$

$$(\boldsymbol{y}' = \boldsymbol{x}' - \mathbf{R}_n)$$

the squared modulus of which is proportional to the ratio of scattered to incident intensity $I_{\text{out}}/I_{\text{in}}$. Thus the scattering from a set of identical scattering centers can be seen as the product of two factors, a *form factor* which is the Fourier transform of the charge density of each scatterer, and a purely geometric *structure factor* which is agnostic of the specific nature of each scatterer and derives only from the geometry of the underlying Bravais lattice. It is because of the structure factor that one observes highly preferential directions of scattering from crystals.

An additional effect is observed when the thermal vibrations of the scattering centers about their mean positions is taken into account. In Equation (2.2) if the atomic positions are corrected for the instantaneous displacements: $\mathbf{R}_n \longrightarrow \mathbf{R}_n + \Delta_n$, the scattered intensity when averaged over many successive vibration cycles contains an additional correction:

$$I_{\text{out}} = I_{\text{in}} \left| \int_{\mathbb{R}^3} d^3x' \; e^{-i\boldsymbol{q} \cdot \boldsymbol{x}'} \widetilde{\rho}(\boldsymbol{x}') \right|^2 \sum_{m,n} e^{-i\boldsymbol{q} \cdot (\mathbf{R}_m - \mathbf{R}_n)} \underbrace{\langle e^{-i\boldsymbol{q} \cdot (\Delta_m - \Delta_n)} \rangle}_{\text{Debye-Waller factor}} \tag{2.3}$$

The Debye-Waller correction, which is also agnostic to the underlying lattice of the scatterers, causes a reduction in the observed intensity. As explained later, there is yet another correction to the observed intensity that arises from the specific experimental

11

geometry, the Lorentz factor. We note the following caveats on the simple scattering model described above:

- The incident radiation should have a coherence length that is significantly greater than the dimension of the scattering object (in this case, the array of atoms).

- The extent of spatial delocalization of each of the electron clouds is significantly smaller than the inter-atomic separations, which in turn are significantly smaller than the distance between the scattering ensemble and the point of observation on the detector.

2.2.2 Basics of X-ray crystallography

We examine the structure factor in Equation (2.2) more closely to determine exactly what relation between the scattering vector $\boldsymbol{q}$ and the placement $\mathbf{R}_i$ of the lattice points gives nonzero scattering. To do this we consider the primitive vectors $\{\boldsymbol{a}_0, \boldsymbol{a}_1, \boldsymbol{a}_2\}$ that generate the lattice points: $\{\mathbf{R}_i\} = \{m_i\boldsymbol{a}_0 + n_i\boldsymbol{a}_1 + p_i\boldsymbol{a}_2 \,|\, m_i, n_i, p_i \in \mathbb{Z}\}$ and the reciprocal lattice vectors that span the dual space to $\{\mathbf{R}_i\}$:

$$\boldsymbol{b}_0 = \alpha \boldsymbol{a}_1 \times \boldsymbol{a}_2$$
$$\boldsymbol{b}_1 = \alpha \boldsymbol{a}_2 \times \boldsymbol{a}_0$$
$$\boldsymbol{b}_2 = \alpha \boldsymbol{a}_0 \times \boldsymbol{a}_1$$
$$\text{where } \alpha = \frac{2\pi}{\boldsymbol{a}_0 \cdot \boldsymbol{a}_1 \times \boldsymbol{a}_2}$$

It is clear that $\boldsymbol{a}_i \cdot \boldsymbol{b}_j = 2\pi\delta_{ij}$. If in the expression for the structure factor, $\boldsymbol{q} \in \{h\boldsymbol{b}_0 + k\boldsymbol{b}_1 + l\boldsymbol{b}_2 \,|\, h, k, l \in \mathbb{Z}\}$ then the structure factor reduces to: $\sum_i e^{-2\pi i(m_i h + n_i k + p_i l)} = N$, where N is of the order of the number of scattering centers within the coherence volume. It can be shown quite simply that for a scattering array of this size, even a slight deviation of $\boldsymbol{q}$ from an integer linear combination of $\boldsymbol{b}_0$, $\boldsymbol{b}_1$ and $\boldsymbol{b}_2$ will not be tolerated *i.e.* the structure factor will tend to zero and there will be no diffraction in that direction. Thus we arrive at the von Laue criterion for diffraction, that the scattering vector has to be a reciprocal lattice vector: $\boldsymbol{q} = \boldsymbol{k}_f - \boldsymbol{k}_i = \boldsymbol{G} \in \{h\boldsymbol{b}_0 + k\boldsymbol{b}_1 + l\boldsymbol{b}_2 \,|\, h, k, l \in \mathbb{Z}\}$ (Figure 2.4). (h, k, l) are the Miller indices for a particular reciprocal lattice vector $\boldsymbol{G}$. The von Laue condition is completely equivalent to the Bragg condition for diffraction. The von Laue formulation of the diffraction condition will be useful in the subsequent analysis of the nf-HEDM experiment. As will be described in Section 2.3.3, an important input parameter to the reconstruction algorithm that determines the orientation field of the sample is a maximum value of $|\boldsymbol{G}|$ for the purposes of simulating diffraction. This parameter is labeled $Q_{\max}$.

(a)

(b)
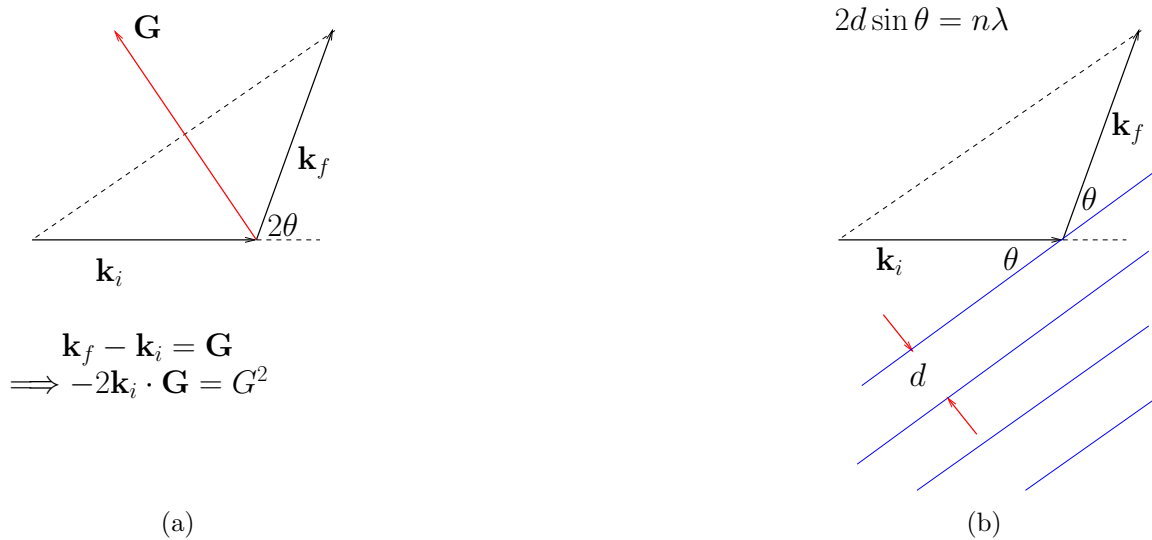
Figure 2.4: **(a)** Illustration of the von Laue condition for non-zero scattering in reciprocal space, **(b)** the equivalent Bragg condition in real space, with the reflecting atomic planes shown in blue.

We now delve deeper into the manner in which the geometrical structure factor mediates Bragg reflections for materials with cubic lattices. In order to do this, we regard the Bravais lattice in the context of a mathematical group: a Bravais lattice is defined as a set of discrete Cartesian points or position vectors that is closed under addition *i.e.* the addition of any two elements of this set also belongs to the set. This group-based definition of the Bravais lattice automatically accounts for the discrete translational symmetry. There are three generators of this group, collectively known as the primitive vectors of the lattice, that physically represent the smallest translations possible between lattice points. By definition, a Bravais lattice is cubic if it has four axes of threefold rotational symmetry [10, 11]. This seemingly non-intuitive yet more fundamental definition of the cubic lattice properly accounts for the different possibilities of regular atomic placements. We demonstrate in detail how one such configuration of primitive vectors results in the well-known body-centered cubic (BCC) lattice structure of α-iron.

Without loss of generality, we assume an axis threefold symmetry to be about the $[1\ 1\ 1]^T$ direction, relative to a fixed coordinate system. For some constant $A_0 > 0$, we consider the Bravais lattice $\{\mathbf{R}_i\}$ generated by the following primitive vectors:

$$\boldsymbol{a}_0 = \frac{A_0}{2} \begin{bmatrix} -1 \\ 1 \\ 1 \end{bmatrix}, \quad \boldsymbol{a}_1 = \frac{A_0}{2} \begin{bmatrix} 1 \\ -1 \\ 1 \end{bmatrix}, \quad \boldsymbol{a}_2 = \frac{A_0}{2} \begin{bmatrix} 1 \\ 1 \\ -1 \end{bmatrix}$$

$$\mathbf{R}_i = m_i \boldsymbol{a}_0 + n_i \boldsymbol{a}_1 + p_i \boldsymbol{a}_2, \ m_i, n_i, p_i \in \mathbb{Z}$$

This lattice is easily shown to have four distinct threefold symmetry axes. Clearly, a 120° rotation of this basis about the axis $[1\ 1\ 1]^T$ rotates these basis vectors into each other cyclically and the rotation applied thrice restores the original configuration. To show that the span of this primitive basis is in fact a cubic lattice in the conventional sense, we express a general $\mathbf{R}_i$ as a sum of special combinations of the primitive basis vectors:

$$\begin{aligned} \mathbf{R}_i &= m_i \boldsymbol{a}_0 + n_i \boldsymbol{a}_1 + p_i \boldsymbol{a}_2 & (m_i, n_i, p_i \in \mathbb{Z}) \\ &= M_i (\boldsymbol{a}_1 + \boldsymbol{a}_2) + N_i (\boldsymbol{a}_2 + \boldsymbol{a}_0) + P_i (\boldsymbol{a}_0 + \boldsymbol{a}_1) + \alpha_i (\boldsymbol{a}_0 + \boldsymbol{a}_1 + \boldsymbol{a}_2) \\ & \hspace{7cm} (M_i, N_i, P_i, \alpha_i \in \mathbb{Z}) \\ &= \frac{A_0}{2} \left(M_i \begin{bmatrix} 2 \\ 0 \\ 0 \end{bmatrix} + N_i \begin{bmatrix} 0 \\ 2 \\ 0 \end{bmatrix} + P_i \begin{bmatrix} 0 \\ 0 \\ 2 \end{bmatrix} + \alpha_i \begin{bmatrix} 1 \\ 1 \\ 1 \end{bmatrix} \right) \end{aligned}$$

Equating coefficients on both sides of the above equation in the three Cartesian dimensions, we get:

$$\begin{bmatrix} 1 & 0 & 0 & 0.5 \\ 0 & 1 & 0 & 0.5 \\ 0 & 0 & 1 & 0.5 \end{bmatrix} \begin{bmatrix} M_i \\ N_i \\ P_i \\ \alpha_i \end{bmatrix} = -\frac{1}{2} \begin{bmatrix} -m_i + n_i + p_i \\ m_i - n_i + p_i \\ m_i + n_i - p_i \end{bmatrix} \tag{2.4}$$

14

If we consider the possible cases for m_i, n_i, p_i (*i.e.* all even, one odd and two even, two odd and one even, all odd), equation (2.4) tells us that no matter what their values, we can always find integers M_i, N_i, P_i, α_i such that $\alpha_i \in \{0, 1\}$. In other words, the entire lattice generated by the original primitive vectors can be expressed as an integer combination of the *new* basis vectors $\boldsymbol{a}'_0 = A_0 [1\ 0\ 0]^T$, $\boldsymbol{a}'_1 = A_0 [0\ 1\ 0]^T$ and $\boldsymbol{a}'_2 = A_0 [0\ 0\ 1]^T$, along with a possible additional shift of $\boldsymbol{\alpha} = (A_0/2) [1\ 1\ 1]^T$. Put yet another way, the entire original lattice can be generated by translating the set $\mathcal{B} = \{[0\ 0\ 0]^T, \boldsymbol{\alpha}\}$ of lattice points by integer multiples of the new basis of vectors $\{\boldsymbol{a}'_i\}$ which is recognized as the conventional basis for the cubic lattice, while the set $\mathcal{B}$ of repeating lattice points is called the *atomic basis*. The original lattice is thus shown to be completely equivalent to a simple cubic lattice of conventional unit cell size A_0 (the familiar lattice constant), with an additional lattice point at the center of each unit cell.

The description of the lattice in terms of the conventional cubic unit cell and the attendant atomic basis $\mathcal{B}$ allows the computation of the structure factor in terms of the simple cubic reciprocal lattice vectors. Given a BCC lattice of conventional unit cell side-width A_0 and basis $\mathcal{B} = \{[0\ 0\ 0]^T, (A_0/2)[1\ 1\ 1]^T\}$, the corresponding reciprocal lattice vectors are:

$$\boldsymbol{b}_0 = \frac{2\pi}{A_0} \begin{bmatrix} 1 \\ 0 \\ 0 \end{bmatrix}, \quad \boldsymbol{b}_1 = \frac{2\pi}{A_0} \begin{bmatrix} 0 \\ 1 \\ 0 \end{bmatrix}, \quad \boldsymbol{b}_2 = \frac{2\pi}{A_0} \begin{bmatrix} 0 \\ 0 \\ 1 \end{bmatrix}$$

and the contribution to the structure factor from each atomic basis in the coherence volume is:

$$\sum_{\mathbf{x} \in \mathcal{B}} e^{-i\boldsymbol{G} \cdot \mathbf{x}} = 1 + e^{-i\pi(h+k+l)}$$

Thus for solids with BCC crystal structure, the only Bragg reflections that have non-zero intensity are whose for which the Miller indices sum up to an even number.

2.2.3 nf-HEDM experimental setup

The nf-HEDM apparatus was set up in the E-hutch of Beamline 1-ID in the Advanced Photon Source (APS) at Argonne National Laboratory. Figure 2.5 shows a photograph of the sample along with the relevant physical components labeled. The sample was mounted upright in a drill bit holder that served as a rotary clamp, which was mounted upon a mobile stage that has translational degrees of freedom along mutually perpendicular Cartesian axes, as well as a rotation degree of freedom about the sample axis. the APS standard laboratory coordinate frame is shown in the figure: $+Z$ points downstream, in the direction of the incident X-ray beam, $+Y$ is vertically upward, along the sample axis of rotation, and $+X$ is mutually perpendicular to these two axes. The detector system consisted of a scintillator that responded

15

Figure 2.5: Photograph of the nf-HEDM apparatus showing the direction of the incident beam along with:

1. Camera optics

2. Sample

3. Rotary clamp mount

4. Z stage (APS convention)

5. Rotation stage

6. X stage (APS convention)

7. Beam-block

8. Scintillator
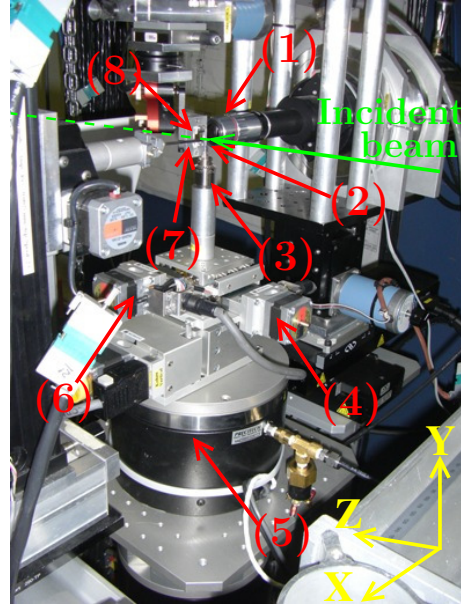
to the incident X-days and a CCD camera with focusing optics that captured the light from the scintillations for the required acquisition time and dumped the image data to a `.tiff` file. The distance between the sample and the scintillator was a few millimeters, of the order of the sample width (hence the name 'near-field', as opposed to 'far-field' measurements for strain resolution in which the separation is of the order of meters and a different detector is used). A tungsten beam-block was inserted in the path of the direct X-ray beam in between the sample and the detector in order to prevent detector pixel burnout. Further upstream of the sample stage (not shown in the photograph) are the focusing and collimating lenses that allow us to focus the beam into a plane. Preliminary calibrations of the experimental apparatus prior to introducing the sample include steps to choose the appropriate beam energy by using one of many available metallic foil filters, horizontally level the moving stages to sub-micron precision and focus the beam and the camera optics.

An experimental schematic is shown in Figure 2.6(a) with a simplified detector system. A single sample layer is illuminated by the beam that has been focused down to a plane (whose projection on the detector is a line of approximate dimensions 1 mm $\times$ 3 μm). This layer contains cross sections of grains whose lattice orientations periodically satisfy the Bragg condition as the sample is rotated about the Z axis (**note**: these default coordinates of the reconstruction software differ from the lab frame coordinates at APS by a simple rotation). As the sample is continuously rotated about this axis through a total angle of 180°, the detector is exposed in turn to the *aggregate* diffraction corresponding to each successive angular interval $\delta\omega$
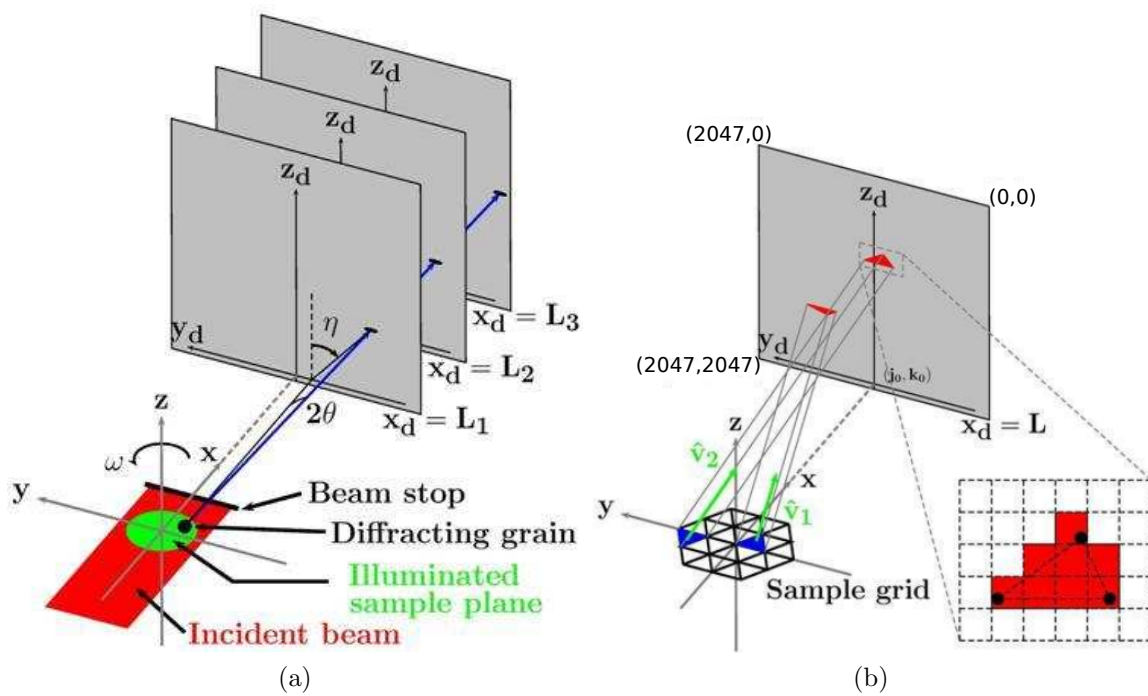
Figure 2.6: **(a)** Simplified experimental schematic, **(b)** Reconstruction of orientations by simulating diffraction from the sample space upon which is superposed a triangular grid (whose elements are called 'voxels') to a 2048 × 2048-pixel detector.

of the sample rotation, which constitutes a separate detector image. For example, if by choice $\delta\omega = 1°$, all the diffraction incident on the detector during angular sweeps of the rotating sample from $-90° \rightarrow -89°$, $-89° \rightarrow -88°$, and so on up to $89° \rightarrow 90°$ respectively constitute separate detector images. A smaller value of $\delta\omega$ naturally implies the ability to resolve more precisely the configuration at which Bragg diffraction took place and therefore the orientations of the diffracting grains. The choice of $\delta\omega = 0.25°$ was finally settled upon by optimizing the scattered intensity on the detector for different image acquisition times and choosing an appropriate value given the size of the target volume and the schedule of available beam time at the synchrotron facility. The process is typically repeated for progressively larger detector distances from the sample, all within the 'near-field' regime (L_1, L_2, L_3 in Figure 2.6(a)) in order to be able to track Bragg peaks during reconstruction of the microstructure orientation field. The fixed spatial resolution is determined by the pixel size of the CCD camera ($\sim 1.48\mu$m) while the tunable angular resolution is determined by the choice of angular integration interval of the sample rotation [12]. The latter is limited by the physical spread of the energy about the nominal value corresponding to monochromatic radiation (from Bragg's law $\delta(E\sin\theta) = 0 \implies |\Delta E/E| = \Delta\theta/\tan\theta \sim 10^{-3}$ for the monochromator used in the experiment). The entire process decribed above is repeated for multiple equally-spaced sample layers and in this manner diffraction data from an entire volume is collected (in our case, 65 layers spaced by 3μm).

It is usual practice in an nf-HEDM experiment to collect the diffraction data of a single layer of a calibration sample whose orientations can be reconstructed easily, before we commence scanning our sample. For this purpose we use a gold wire which is about 30 μm in diameter and has only five well-ordered grains in its cross section. The reconstruction can be achieved in a few hours, which usually fits well into the typical beamline schedule. The purpose of imaging and reconstructing the gold beforehand is to obtain rough initial estimates for the experimental parameters (see Section 2.3.2), owing to the fact that the experimental stage would not have moved significantly in the process of switching out the gold sample with the α-iron.

It is evident from the geometry described in Figure 2.4(a) that scattering corresponding to higher magnitudes of $\boldsymbol{G}$ are found higher up on the detector (i.e. 2θ increases). The exact geometric criterion for satisfying the von Laue condition is visualized in Figure 2.7. For a given magnitude of reciprocal lattice vector $\boldsymbol{G}$ (i.e. 'order' of scattering), the set of all possible $\boldsymbol{q} \equiv \boldsymbol{k}_f - \boldsymbol{k}_i$ of magnitude $|\boldsymbol{G}|$ sweeps out a cone of opening half-angle $90° - \theta$ (shown in blue in Figure 2.7). During the rotation of the crystal, $\boldsymbol{G}$ itself sweeps out the cone shown in green. The intersection of these two cones implies that for those particular sample orientations, $\boldsymbol{q} = \boldsymbol{G}$, which is in fact the von Laue condition for visible diffraction. Under this precise condition, a Bragg peak is observed at the point that the corresponding ray $\boldsymbol{k}_f$ intersects the
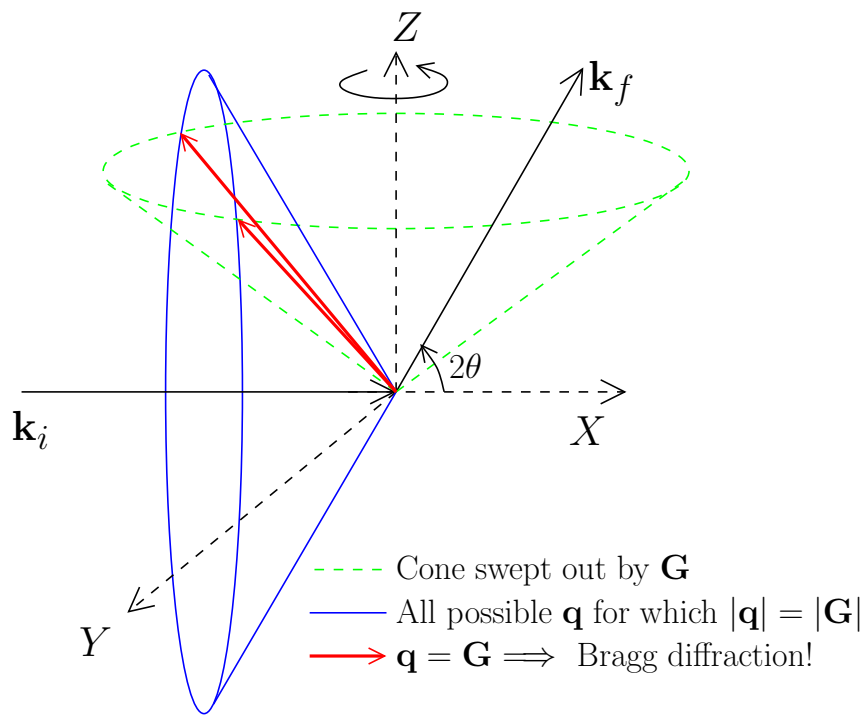
Figure 2.7: Condition for Bragg scattering for a reciprocal lattice vector of given magnitude G in which the cone swept out by $\boldsymbol{G}$ in the rotating crystal experiment intersects the cone of all possible scattering vectors $\boldsymbol{q}$ of magnitude G.

--- - Cone swept out by $\mathbf{G}$
——— All possible $\mathbf{q}$ for which $|\mathbf{q}| = |\mathbf{G}|$
——→ $\mathbf{q} = \mathbf{G} \implies$ Bragg diffraction!

detector. This geometry indicates that an eligible Bragg peak will cause diffraction at most twice in the sample rotation interval from 0° to 180°. In practice, owing to the finite angular resolution of the experiment each eligible G satisfies the Bragg condition for a finite interval of time, which is heavily dependent on the scattering geometry for that particular G. The aggregated intensity of the corresponding Bragg peak on the detector is proportional to this finite time. This multiplicative factor of intensity of different Bragg peaks that was alluded to earlier is known as the Lorentz factor and is different for scattering onto different regions of the detector.

The form factor, structure factor, Debye-Waller and Lorentz factors all contribute significantly to the observed intensity of the Bragg peaks. However, nf-HEDM has historically been concerned with scattered intensity only to the extent of discerning the projection of a grain cross-section on the detector, and not the actual peak intensity profiles *per se*. This might soon change with future releases of the reconstruction software in which peak intensity information, including the tails are utilized to pinpoint the geometric parameters of the experiment to high precision.

2.3 Post-acquisition data processing

2.3.1 Peak extraction from diffraction data

The diffraction signal obtained in an nf-HEDM experiment consists of the geometric projections of the microstructural features of the sample onto the detector plane (*i.e.* the ideal shape of a Bragg peak on the detector is in fact the projection of the cross section of the grain that it came from). Estimations of grain cross-sections depends upon successful deconvolution of the true geometric projections from ambient detector noise and smearing effects, the primary causes of which are:

- Cosmic rays and stray electromagnetic radiation.

- Inherent Poissonian counting noise.

- Inelastic and diffuse scattering from the sample.

- The inherent point spread function of the detector pixels.

- The finite width of the energy spectrum of the X-ray beam which causes tails in the intensity at the edges of the Bragg peak.

Cosmic rays are typically responsible for 'hot' pixels *i.e.* isolated pixels on the detector that are brightly lit in contrast to their immediate neighbors. The typical post-processing treatment to rid the detector image of them is a simple median filter with a sufficiently small kernel (in the case of α-iron, this was set to a 1 pixel radius, which effectively means a kernel of the central pixel and its immediate 4-neighbors). Stray
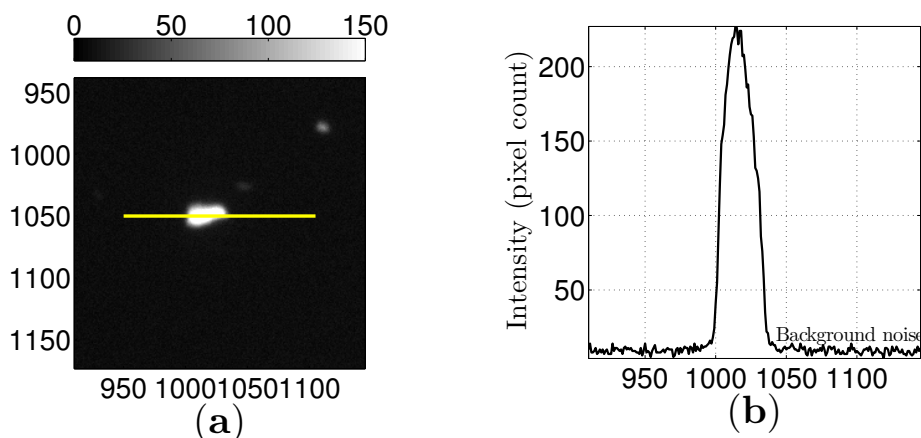
Figure 2.8: **(a)** 2D intensity plot of a Bragg peak found on the detector, with the maximum displayed intensity thresholded to make the peak more prominent, along with a line along which the intensity profile is plotted in **(b)**.

electromagnetic radiation is minimized by darkening the inside of the hutch during the image acquisition. Counting noise and inelastic scattering are in general responsible for a relatively constant background noise on the detector with small fluctuations, as can be seen from the intensity line profile of a typical peak in Figure 2.8. For the last two items listed above, one of the required steps is a robust edge-detection technique to remove the tails and estimate the true edge of the peak and thereby the true edge of the grain cross section. This is a mathematically involved task and is the subject of Section 3.1 in Chapter 3.

The issue of constant background noise is addressed by subtracting an estimate of the constant background from each of the acquired detector images. The background image is determined by setting the value of each image pixel to be the median count of that detector pixel, taken over all $180/\delta\omega$ images acquired for a fixed detector-sample distance (where $\delta\omega$ is the sample rotation interval over which diffraction is aggregated). The connected components are then identified and the image is further denoised by removing those connected components whose constituent pixels number fewer than a fixed threshold, which is a parameter of the signal detection algorithm. This threshold is set by the user as the minimum number of pixels that should be in a connected component for it to be considered diffraction from a grain. This procedure has the inherent risk of ignoring very small grains which are of the order of the pixel size and yet produce non-negligible diffraction. The threshold number must therefore be carefully chosen. For the detection of the α-iron peaks, this threshold was chosen to be 3 pixels. We point out, however, that the connected component procedure also tends to keep large collections of pixels on the detector that may not constitute diffraction signal from a grain at all. This is not a concern owing to the

fact that the orientation reconstruction is done not by back-projecting Bragg peaks to the sample space, but by forward-modeling the orientation and then inferring what its diffraction would look like. Therefore any spurious detector peaks will be ignored. The discussion of the forward modeling algorithm is deferred to Section 2.3.3.

Final steps in the image detection sequence include:

- The clipping of a constant fraction of the maximum intensity of each peak from the bottom of the peak. If this constant is chosen to be f where $f \in [0, 1]$, then the top $1 - f$-fraction of the peak height is retained. This is another input parameter of the detection algorithm that should be judiciously chosen, and in the case of the α-iron was set to 0.1 (*i.e.* the top 90% of the peak was retained). This step combined with the edge detection step mentioned earlier (Section 3.1) together address the issue of Bragg peak tails due to the detector point spread function and the finite energy width.

- A blanket subtraction of intensity from the entire detector in order to clean up any residual isolated pixels of low intensity. This was set to 3 counts in the case of the α-iron.

This signal detection algorithm was implemented by Lind [6] using C++ bindings of the open-source Insight Toolkit (ITK) image processing library.

2.3.2 Parameters Monte Carlo

The first step in extracting useful information from the denoised diffraction data is the precise determination of the relevant parameters of the experimental geometry as they were at the time of data acquisition. These include, for every possible detector-sample separation:

1. The projection of the origin of the sample frame on the detector, in pixel coordinates (*i.e.* the point (j_0, k_0) in Figure 2.6(**b**))

2. The distance of the sample frame origin from the detector (x_d in Figure 2.6(**b**))

3. The $SO(3)$ transformation that takes the sample frame from the convention adopted at the APS ($+Z$-downstream) to the convention adopted by the reconstruction software ($+x$-downstream)

This is a necessary step in the eventual generation of high-resolution orientation maps of the images microstructure. We have no way of measuring these quantities precisely at the beamline and therefore they must be obtained entirely from the diffraction data itself. We choose to adopt a two-step algorithm in which (1) the crystal orientations of a select few voxels in the sample space (shown in blue in Figure 2.6(**b**)) are estimated by initially selecting random orientations and adjusting them until the total diffraction

simulated from them overlaps maximally with the observed diffraction on the detector (global optimization), and then (2) optimizing this initial overlap further against the experimental parameters to be determined (a more thorough local optimization). This is achieved by a parallel algorithm built into the reconstruction software that simultaneously performs a Monte Carlo search in different regions of a windowed subspace of geometric parameters, centered about initial rough estimates. The success of the local step is predicated upon that of the global step, which in turn depends on the user-provided initial guess of the experimental parameters. Typically better and better parameters are obtained by repeating the local optimization step with smaller and smaller tolerances.

A highly reliable method of refining parameters is to optimize them against the voxels along grain boundaries obtained from a preliminary reconstruction using less refined parameters. This is because boundary voxels are highly sensitive to small changes in experimental parameters, owing to a relatively large change in overlap fraction between simulated and observed diffraction due to even a slight change in the experimental parameters. A more detailed description of the reconstruction algorithm and and the 'confidence' metric that quantifies the goodness of a reconstruction is described in Section 2.3.3

We note that the all-important step of simulating diffraction, performed in the global optimization step described above and which also forms the basis of the forward modeling algorithm described in Section 2.3.3, relies on specifying the magnitude of the largest scattering vector Q_{max} to be simulated. This is typically done by examining the distribution of the $|\boldsymbol{G}|$ for different Bragg peaks on the detector and choosing an appropriate value based on how much of the detector area should be queried for a reliable, high-quality reconstruction.

2.3.3   Orientation reconstruction

Having satisfactorily denoised the diffraction data and obtained precise estimates of the experimental parameters, the final step is the application of the forward modeling algorithm used in simulating diffraction, to determine the orientation field in 2 dimensions that generated the observed Bragg diffraction. A thorough description of this is given in the PhD thesis of Li [4]. For reference, we return to Figure 2.6(**b**). In short, this is achieved on a voxel-by-voxel basis (a voxel being an element of the triangular grid imposed on the sample space) by assuming a crystal orientation for each voxel and then transforming that orientation in a direction that maximizes the fraction of overlap between the observed diffraction and diffraction simulated from the voxel. Broken down, this statement implies that we require two things:

1. A means to navigate and interpolate between points of the space of crystal orientations.

2. Given an orientation for a voxel, a convenient metric that quantifies the extent of overlap of simulated diffraction with the denoised detector intensity, taken over *all* detector coordinates, including stepping along successive detector images.

The first of these issues is addressed briefly in Section 3.2, Chapter 3. For the second we begin with the definition of the set of *qualified peaks* $\mathbb{Q}$ for a given voxel orientation and a maximum order of scattering (the latter is an input parameter to the reconstruction algorithm, $Q_{\max}$), which denotes all the permitted Bragg peaks that should be present on the detector at all sample-detector separations, over the entire range of sample rotation. $\mathbb{Q}$ is completely determined given the knowledge of the lattice structure of the scattering material, the direction of the incident beam and the orientation associated with the voxel. If for any peak $i \in \mathbb{Q}$, the geometric projection of the voxel onto the detector covers $N_{\mathrm{sim}}^{(i)}$ detector pixels (where 'sim' denotes simulated diffraction) and if these pixels overlap with $N_{\mathrm{obs}}^{(i)}$ pixels' worth of observed diffraction on the *denoised* detector image, then the **quality metric** $\mathcal{Q}$ of the voxel orientation is given by:

$$\mathcal{Q} = \frac{1}{N_{\mathbb{Q}}} \sum_{i \in \mathbb{Q}} \frac{N_{\mathrm{obs}}^{(i)}}{N_{\mathrm{sim}}^{(i)}} \tag{2.5}$$

where $N_{\mathbb{Q}}$ is the number of qualified peaks for that voxel in its current orientation. $\mathcal{Q}$ is essentially the mean fraction of pixel overlap of all qualified peaks of a voxel. In the case of the voxel size being smaller than the detector pixel size, $N_{\mathrm{sim}}^{(i)} = 1$ and $N_{\mathrm{obs}}^{(i)} \in \{0, 1\}$ for all $i \in \mathbb{Q}$. The quality is then termed the **confidence** $\mathcal{C}$:

$$\mathcal{C} = \frac{1}{N_{\mathbb{Q}}} \sum_{i \in \mathbb{Q}} N_{\mathrm{obs}}^{(i)} \tag{2.6}$$

$$\text{where } N_{\mathbb{Q}} = \sum_{i \in \mathbb{Q}} N_{\mathrm{sim}}^{(i)}$$

As far as terminology goes, quality and confidence are used interchangeably. The goal, then, is to find that orientation of the voxel that maximizes its quality. As a rough guideline (assuming the appropriate value of $Q_{\max}$ has been chosen), it is expected that the quality of a fit voxel in the interior of a well-ordered grain would be close to 100% because it would diffract into the interior of a Bragg peak, whereas a fit voxel along a grain boundary would have a quality of $\sim 50\%$ because half of its detector projection on average would lie outside the edge of a Bragg peak. Quality also decreases due to scattering from deformed microstructure owing to the absence of a regular atomic lattice. This makes nf-HEDM useful for identifying regions of strain, elastic and plastic deformation [13, 14, 15, 16, 17]. The direction of navigation in the space of orientations is determined by a Monte Carlo algorithm whose iterations minimize the cost $1 - \mathcal{Q}$ at every step ('zero-temperature' Monte Carlo).

The ability of the forward modeling algorithm to adjust voxel orientations in order to obtain maximum pixel overlap has some interesting consequences for reconstruction of orientations at the physical sample edges. Essentially, reconstructions just beyond the sample edges display not an abrupt drop in voxel quality as one would expect, but a gradual decrease for significant lengths beyond the sample edge, falsely indicative of the presence of microstructure in regions of free space. This makes nf-HEDM unsuitable for imaging microstructures with voids, and such samples must also be accompanied by tomographic reconstructions in order to describe their morphologies completely. Some results addressing this issue are described in Chapter 6.

Since the orientation of each voxel is determined by optimizing against the entire diffraction data set independently of the other voxels, the reconstruction is embarrassingly parallel. A master process distributes voxels to waiting slave processes and takes care of the book-keeping while the slaves simultaneously determine the orientations of their assigned voxels. This has been implemented using C++ bindings for Message Passing interface (MPI) standard by S. F. Li [8]. This is the most computationally intensive component of this thesis and requires hundreds of thousands of CPU hours for a complete volume.

Chapter 3

Numerical techniques

In this chapter we describe established numerical techniques implemented at various stages of the data analysis. This part of the analysis pipeline deals with processing data up to the point of being able to use it for computations involving energetics of grain boundaries, which is the eventual goal. These subsequent computations are described separately in Chapter 5. The preliminary computations described here broadly fall into the following theoretical categories and are listed in the order of implementation downstream from the collection of the diffraction data onward. We focus on the underlying mathematical theory and highlight its use in specific components of the computational pipeline as and when necessary.

1. **Digital signal processing I**: Basic image filtering techniques.

2. **Differential geometry**: The properties of the space of crystallographic orientations and the sampling and interpolation scheme used to navigate it in the orientation search.

3. **Volume registration**: The physical alignment of the two scanned volumes to the best of our abilities so that we may directly track the transformations of individual microstructural features.

4. **Meshing**: A basic characterization of node connectivity of the gridded grain surfaces.

5. **Digital signal processing II**: A novel surface smoothing technique specifically tailored to the grid-induced coarseness of microstructure elements in order to obtain smooth features.

6. **Optimization**: The underlying mathematics of linear optimization and standard algorithms to solve such problems.

Of these, all are briefly described in this chapter with appropriate references for the reader who wishes to go deeper, except for item 5. This is a filtering technique

specially tailored to the intricacies of interface network geometry and topology and is sufficiently different from most existing smoothing techniques in computer vision to warrant a separate and detailed description, in Chapter 4. The content of Chapter 4 constitutes a submitted manuscript.

3.1   Edge detection

The first order of business after collecting the diffraction data is to deconvolve the various dispersion effects from the observed Bragg peaks on the area detector in order to delineate to the best of our abilities the true geometric projection of the grain onto the are detector. The small spread in the wavelength of the incident X-ray beam ($\Delta\lambda/\lambda \sim 10^{-3}$) results in some of the incident energy being diffracted in a direction slightly different from that predicted by the Born approximation at the nominal wavelength. This physically manifests as tails in the two-dimensional distribution of intensity on the detector. We describe briefly in this section the edge-detection technique used to estimate the location and shape of the Bragg peaks on the detector. The basic mathematics is explained through one-dimensional examples and is followed by the straightforward generalization to the two-dimensional case. The edge-detection is a crucial step in the reduction process of the noisy detector data and has the demonstrated ability to differentiate Bragg peaks on the detector with substantial tail overlap [6]. Briefly, the edge-detection method is implemented as a zero-crossing detection of a convolution of the signal with a smoothing function.

Consider an one-dimensional intensity profile viewed as a unimodal distribution $f_0(x) \geq 0$ over some independent variable x. The energy content of this signal is assumed to be finite: there exists $M \in \mathbb{R}^+$ such that $\int_{-\infty}^{\infty} dx \; |f_0(x)| < M$ *i.e.* $f_0(x)$ has a bounded L^1 norm. We wish to remove the tails of this intensity distribution and retain its central portion as representative of the true diffraction from the cross section of a grain in the sample, as dictated by the Born approximation.

While this prescription is straightforward for smooth profiles (Figure 3.1), the effect of counting noise due to integration of the signal for a finite time on the pixels of the CCD camera requires us to perform this edge detection on a kernel-smoothed version of the noisy intensity profile. The noise can be modeled as a random variable $\eta(x)$ which is a function of the spatial coordinate. This amounts to picking the zero-crossings of a convolution of the original signal with the second derivative of the smoothing kernel. If our noisy signal is $f(x) \equiv f_0(x) + \eta(x)$ and the kernel function $g(x)$ have bounded L^1 norms, then this equivalence can be shown quite simply:
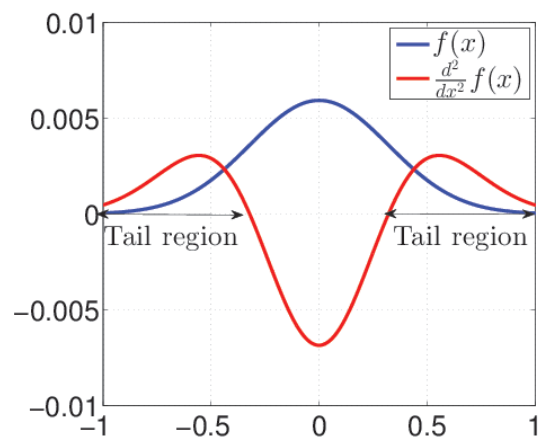
Figure 3.1: Estimated edges of a 1-dimensional intensity peak at the locations of the zero-crossings of the second derivative. We require to remove the tail regions and retain the central part.

Proof.

$$\frac{d^2 h}{dx^2} = \frac{d^2}{dx^2} \left(f * g \right)(x)$$

$$= \frac{d^2}{dx^2} \int_{-\infty}^{\infty} dx' \; f(x - x')g(x)$$

$$= \int_{-\infty}^{\infty} dy' \; \frac{d^2}{dy'^2} f(y')g(x - y') \qquad\qquad (y' = x - x')$$

$$= \frac{d}{dy'} f(y')g(x - y') \Big|_{y'=-\infty}^{\infty} \;{}^{0} + \int_{-\infty}^{\infty} dy' \; f'(y')g'(x - y')$$

$$= f(y')g'(x - y') \big|_{y'=-\infty}^{\infty} \;{}^{0} + \int_{-\infty}^{\infty} dy' \; f(y)g''(x - y')$$

$$\square$$

Thus, the zero crossings of $h''(x)$ are also those of $\int_{-\infty}^{\infty} dx' \; f(x')g''(x - x')$. The boundary terms go to zero because of the boundedness of the norms of f and g. The choice of the Gaussian of standard deviation σ for g results in what is variously called the Mexican hat, Rickers, blob detector or Laplacian-of-Gaussian (LoG) convolution kernel.

$$g(x; \sigma) = \frac{1}{\sqrt{2\pi}\sigma} \exp\left[-\frac{x^2}{2\sigma^2}\right]$$

$$\frac{d^2}{dx^2} g(x; \sigma) = -\frac{1}{\sqrt{2\pi}\sigma^3} \left(1 - \frac{x^2}{\sigma^2}\right) \exp\left[-\frac{x^2}{2\sigma^2}\right]$$

As can been seen in Figure 3.2, the zero crossings of the convolution correspond to the beginnings of the tails of the original noiseless function $f_0(x)$. We note that convolution with a smoothing kernel inevitably results in the broadening of the original signal. A good choice of kernel is informed by a knowledge of the qualitative features of the signal as well as the noise.

The extension to image processing in two-dimensional coordinates $\mathbf{x} = [x \; y]^T$ is done in general by the two-dimensional Gaussian kernel:

$$g(\mathbf{x}; R) = \frac{1}{\sqrt{(2\pi)^2 \det(R)}} \exp\left[-\frac{1}{2}\mathbf{x}^T R^{-1} \mathbf{x}\right] \qquad\qquad (3.1)$$

where R is the 2×2 covariance matrix that generalizes the role of σ in the one-dimensional case. The second derivative is now replaced by the Laplacian operator ∇^2 in two dimensions and the generalization is straightforward. The edge-detection of diffraction peaks of a two-dimensional image $f(\mathbf{x})$ is done by locating the zero-crossings of the smoothed function $f(\mathbf{x}) * \nabla^2 g(\mathbf{x}; R)$. For the simple case of diagonal

29
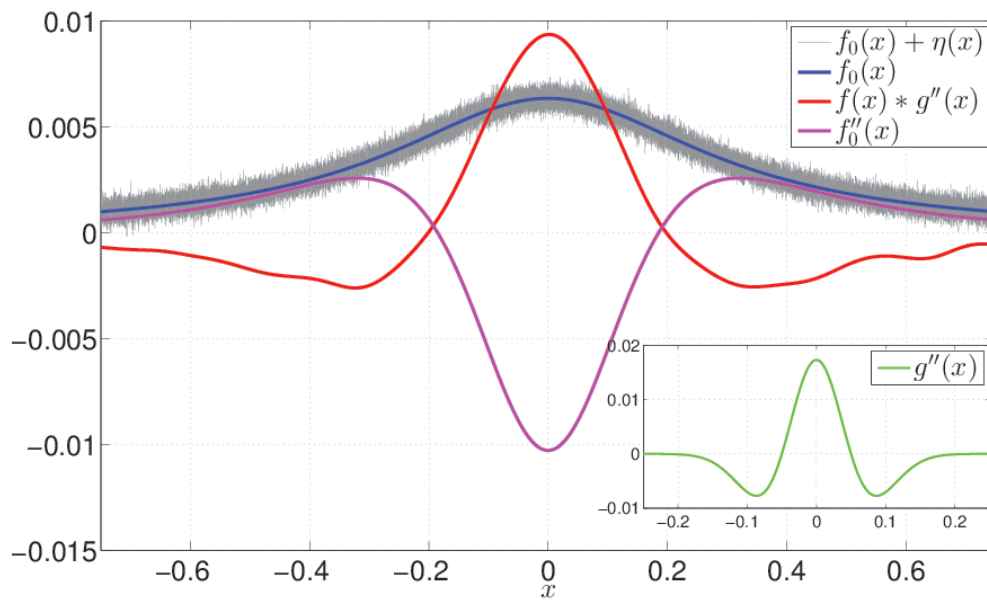
Figure 3.2: Edge detection in a signal $f_0(x)$ superposed with noise $\eta(x)$ using a Laplacian-of-Gaussian filter, with the convolution kernel $g''(x; \sigma)$ shown inset.

$$R = \begin{bmatrix} a & b \\ b & c \end{bmatrix}$$

$$\lambda_1 \neq \lambda_2$$

$$R = \begin{bmatrix} \lambda_1 & 0 \\ 0 & \lambda_2 \end{bmatrix}$$

$$\lambda_1 \neq \lambda_2$$

$$R = \begin{bmatrix} \lambda_1 & 0 \\ 0 & \lambda_2 \end{bmatrix}$$

$$\lambda_1 = \lambda_2$$

(a) (b) (c)
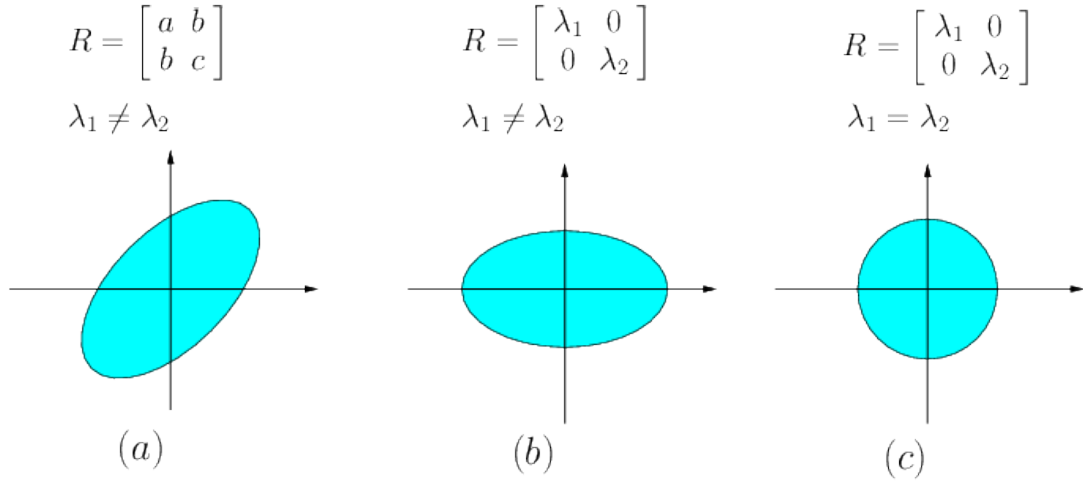
Figure 3.3: **(a)** General configuration of a smoothing kernel, with corresponding covariance matrix R and its eigenvalues λ_1 and λ_2; **(b)** grid-aligned kernel but not isotropic; **(c)** grid-aligned and isotropic.
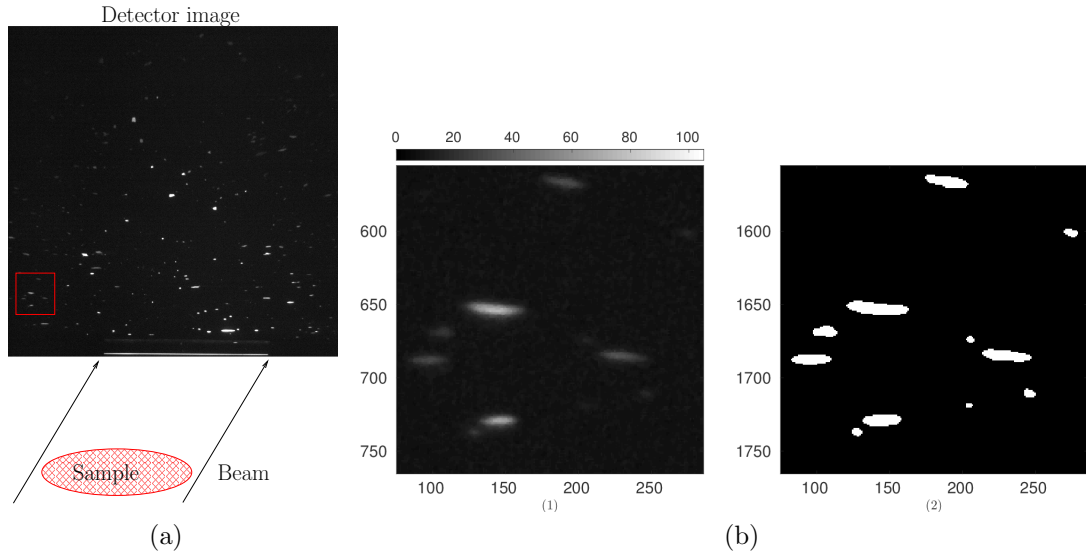
Figure 3.4: Edge detection of peaks on a typical detector image. **(a)** Detector geometry highlighting the region of interest; **(b)**(1) region of interest zoomed in; **(b)**(2) binarized intensity of peaks whose edges were estimated using a LoG filter with an isotropic kernel.

R with degenerate eigenvalues (Figure 3.3**(c)**), the results of edge detection are shown in Figure 3.4 for a region of an actual nf-HEDM detector image, and superposed raw data for a particular Bragg peak in Figure 3.5. The case of grid-aligned but anisotropic smoothing kernel (Figure 3.3**(b)**) may be implemented in order to offset

31
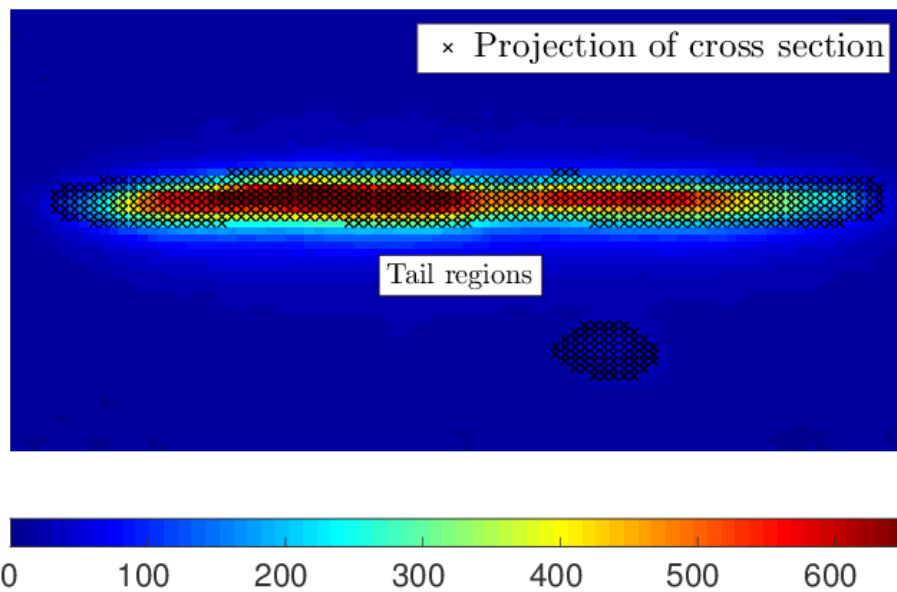
Figure 3.5: Estimating the projection of the cross section of grains by eliminating the surrounding tail regions from the intensity profile. The color scale denotes the pixel-wise intensity count returned by the CCD camera while the 'x' markers are those pixels estimated by the edge detection algorithm to be inside the geometric projection of the grain.

the bias in sensitivity of edge detection along the vertical direction on the near-field detector [6]. We close by noting that the edge detection process described here does not constitute the entire data reduction pipeline, but is a crucial part of it. The entire process involves steps of median filtering and background subtraction as well and is described in more detail in Chapter 2.

3.2 Orientation gridding and interpolation

The forward modeling method of reconstruction of an image from nf-HEDM data is predicated upon a search for the crystal orientations that are most likely to cause the observed diffraction. This requires a reliable means of parameterizing and navigating the space of orientations. In this section we briefly address this aspect of the data processing pipeline. For a more thorough description the reader is referred to [4].

Any orientation, essentially being a rotation of the frame of Bravais lattice basis vectors from some reference position, is representative of an element of the abstract rotation group $SO(3)$. The name derives from its most common representation by **S**pecial **O**rthogonal matrices in **3** dimensions. However, in the presence of crystal symmetry, one must account for multiplicity of orientations under the set of N rotations $\mathbb{S}_N$ that leave a particular lattice invariant. The relevant set of orientations is therefore reduced to an effective subspace: $SO(3) \longrightarrow SO(3) \,(\text{mod } \mathbb{S}_N)$ known as the *fundamental zone* of orientations. The orientation search is carried out in this symmetry-reduced subspace instead of the entirety of $SO(3)$. Owing to the ease of interpolation using existing prescriptions, we turn to the set of unit quaternions $\mathbb{H}$ as an alternative representation of $SO(3)$. If an orientation is viewed as a rotation of an angle θ about an axis $\hat{\boldsymbol{n}} = [n_0 \; n_1 \; n_2]^T$ and symbolized as $(\theta, \hat{\boldsymbol{n}})$, then the unit quaternion $\mathbf{q} \equiv \left[\cos\frac{\theta}{2} \; \sin\frac{\theta}{2} \,(n_0 \; n_1 \; n_2)\right]^T$ represents the orientation and maintains the composition relation between the corresponding group elements under quaternion multiplication. Since $\mathbf{q}^T\mathbf{q} = 1$, the task of sampling $SO(3)$ reduces to the problem of sampling the unit 3-sphere S^3, far easier to parameterize than the set of 3×3 special orthogonal matrices. We note however that $\mathbb{H}$ is not a faithful representation of $SO(3)$ (they are not *isomorphic*). $\mathbb{H}$ is a double cover of $SO(3)$; both $\mathbf{q}$ and $-\mathbf{q}$ denote the same orientation: $(\theta, \hat{\boldsymbol{n}}) = (2\pi - \theta, -\hat{\boldsymbol{n}})$.

The general technique of sampling $SO(N)$ through the hypersphere S^{N-1} is described in detail by Yershova [18]. We summarize the technique for the special case of $N = 3$. Consider a regular polytope in 4 dimensions centered at the origin and circumscribed in the hypersphere S^3. The samples of S^3, which bear a one-to-one relationship to the samples of $SO(3)$, are obtained by projecting the uniform sample points of the faces of the polytope (a layered Sukharev grid) on to the surface of S^3. Owing to the double coverage of $SO(3)$ by $\mathbb{H}$, it is sufficient to sample only one of the

two hemi-hyperspheres. We choose to sample those orientations with rotation angle $\theta \in [-\pi, \pi]$, which correspond to the first component of $\mathbf{q}$ being non-negative. This sampling method can be shown to have an upper bound for the *sampling dispersion* δ which is defined for a point set X sampling a volume V as:

$$\delta(X) = \sup_{v \in V} \min_{x \in X} \rho(x, v) \tag{3.2}$$

In other words, the dispersion is the radius (according to metric of choice ρ) of the largest ball in the sampled space that does not contain any sample point. For the sampling method implemented in the orientation reconstruction algorithm, it can be shown [18] that

$$\delta \leq \frac{2\pi}{[1 + 7n]^{1/3}} \tag{3.3}$$

where n is the number of sample points in the Sukharev grid.

Having achieved a reasonable sampling of $SO(3)$, a smooth interpolation between two given sample points can be achieved using spherical linear interpolation [19], which is parameterized by a scalar $t \in [0, 1]$:

$$\mathbf{q}(t) = \text{Slerp}(\mathbf{q}_0, \mathbf{q}_1, t) = \mathbf{q}_0 \left(\mathbf{q}_0^{-1}\mathbf{q}_1\right)^t \tag{3.4}$$

$$= \frac{\sin(1 - t)\theta}{\sin \theta}\mathbf{q}_0 + \frac{\sin t\theta}{\sin \theta}\mathbf{q}_1 \tag{3.5}$$

where $\theta = cos^{-1}\left(\mathbf{q}_0 \cdot \mathbf{q}_1\right)$

Equations (3.4) and (3.5) give a prescription for interpolation between a pair of quaternions $\mathbf{q}_0$ and $\mathbf{q}_1$. One can extend this to interpolate in two dimensions between quaternions $\mathbf{q}_0$, $\mathbf{q}_1$, $\mathbf{q}_2$ and $\mathbf{q}_3$ taken in cyclic order, that delineate a square patch on S^3:

$$\text{Slerp2D}(\mathbf{q}_0, \mathbf{q}_1, \mathbf{q}_2, \mathbf{q}_3;\ t, u) = \text{Slerp}\left[\text{Slerp}(\mathbf{q}_0, \mathbf{q}_3, t), \text{Slerp}(\mathbf{q}_1, \mathbf{q}_2, t), u\right] \tag{3.6}$$
$$\text{where } 0 \leq t, u \leq 1$$

3.3 Volume registration

Tracking microstructural features from the data from an *ex situ* experiment is contingent upon the correct alignment of the 3D images corresponding to before and after the processing (in our case, the annealing in a tube furnace). The reason for misalignment is simple; it is almost certain that the sample would have not been re-mounted in exactly the same position and orientation with respect to the X-ray beam. Time and infrastructure constraints at the beamline dictate that this part of the data processing be done at leisure further downstream from the data collection.

For historical reasons, we chose to operate directly on the output files of the native HEDM format. To reiterate, these are ASCII files (typically with the extension '`.mic`') that simply list the positions and crystal orientations of all the sample space voxels, for a single layer. A set of such files corresponding to a list of contiguous layers, with advance knowledge of the layer spacing, constitutes data of an entire scanned volume. The availability of two contiguous volumes corresponding to essentially the same region of the α-iron sample enables us to stick to the following simple sequence of steps for registration:

1. Determine the single rigid-body registration that aligns a single layer in the post-anneal volume with its corresponding layer in the pre-annealed volume. Apply this transformation to all layers in the post-anneal volume.

2. Pick one grain that is present in both volumes and rotationally align the entire post-anneal volume such that the two orientations of the grain coincide. We assert that this brings the volumes into angular alignment to within experimental resolution, as is demonstrated in the relevant section in the results (Chapter 6).

3.3.1 Single layer registration

This subsection concerns the in-plane alignment of two microstructures representing the same slice of a sample, physically translated and rotated away from each other, but subject to the same grid discretization. We denote the starting configuration as the 'source', and the one to be attained as the 'target'. The rigid body transformation that takes the source to the target can be viewed as a combination of a uniform translation by $\boldsymbol{r}_{tr}$ in the plane and a rotation R about the centroid $\boldsymbol{r}_{CM}$ of the 2D microstructure:

$$\begin{aligned} \boldsymbol{r}' &= \boldsymbol{r}_{tr} + \boldsymbol{r}_{CM} + R\left(\boldsymbol{r} - \boldsymbol{r}_{CM}\right) \\ &= \boldsymbol{r}_{tr} + R\boldsymbol{r} + \left(\mathbb{1} - R\right)\boldsymbol{r}_{CM} \end{aligned} \tag{3.7}$$

where $\boldsymbol{r}$ and $\boldsymbol{r}'$ are the initial and final positions of each point in the microstructure. The voxels of the source microstructure transformed in this manner to their new positions represented by $\boldsymbol{r}'$ should be representative of the target microstructure. This sequence of steps is shown in Figure 3.6. Since the `.mic` file is structured to describe the triangular area elements obtained from the recursive division of a triangular grid, a naïve planar rotation is insufficient since the orientational sense of the grid elements (*i.e.* pointing up or down) must be maintained, as opposed to the orientation *field* at that point in the microstructure. The task at hand is achieved by generating a blank grid of the same resolution of the target `.mic` file, and updating the information in its voxels according to where in the source configuration it might have come from prior to transformation (Figure 3.7). This involves not only applying the rigid body transformation, but also modifying the orientation of each voxel appropriately.
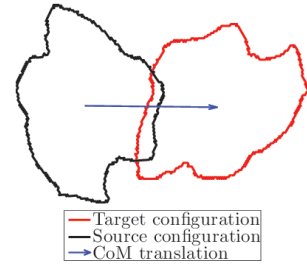
Figure 3.6: **(a)** Structure of three adjacent grains with uneven boundary features; the sequence of alignment is shown in the sequence *(b) - (c) - (d)*: **(b)** The centroid of the source microstructure is translated to that of the target; **(c)** the translated source is rotated about its new centroid to attain maximum overlap with the target configuration; **(d)** Final registered layers.
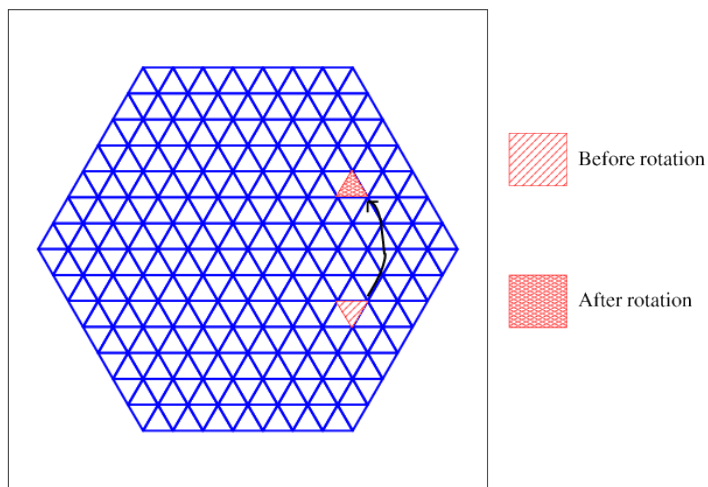
Figure 3.7: Rotation of a microstructure while adhering to the hexagonal grid involves transformation of orientations as well. The part of the microstructure in the region of the 'before' voxel moves to region of the 'after' voxel after the rigid body transformation. The orientation of the crystal at that location changes as well, all the while adhering to the original triangular grid.

The question of crystal lattice transformations is more involved. Orientation space is 3-dimensional and the set of all orientations forms a group under composition that is isomorphic to the rotation group $SO(3)$. Thus, orientations/misorientations can be represented by rotation matrices and unit quaternions. Although theoretical physics has adopted rotation matrices as standard and convenient notation, unit quaternions are computationally more efficient. A good reference for unit quaternions and the space of rotations is [20].

Let the orientation of a voxel before and after sample rotation be denoted by unit quaternions Q_{before} and Q_{after} respectively. Let the sample rotation itself be represented by Q_{rot}. A vector $\mathbf{v}$ in the sample frame becomes $\mathbf{v}'$ after (active) rotation given by:

$$\mathbf{v}' = Q_{\text{rot}} \mathbf{v} Q_{\text{rot}}^{-1} \tag{3.8}$$

The vector $\mathbf{v}$ in the original crystal frame is given by a (passive) rotation and becomes $\mathbf{v}_{\text{before}}$ given by:

$$\mathbf{v}_{\text{before}} = Q_{\text{before}}^{-1} \mathbf{v} Q_{\text{before}} \tag{3.9}$$

Similarly the vector $\mathbf{v}'$ when seen in the *rotated* crystal frame looks like:

$$
\begin{aligned}
\mathbf{v}_{\text{after}} &= Q_{\text{after}}^{-1} \mathbf{v}' Q_{\text{after}} \\
&= Q_{\text{after}}^{-1} \left(Q_{\text{rot}} \mathbf{v} Q_{\text{rot}}^{-1} \right) Q_{\text{after}} \\
&= \left(Q_{\text{rot}}^{-1} Q_{\text{after}} \right)^{-1} \mathbf{v} \left(Q_{\text{rot}}^{-1} Q_{\text{after}} \right)
\end{aligned}
\tag{3.10}
$$

But both $\mathbf{v}_{\text{before}}$ and $\mathbf{v}_{\text{after}}$ are essentially expressions for an *arbitrarily chosen* vector in the crystal frame which doesn't change relative to that frame before and after rotation. Thus equating (3.9) and (3.10), we get *for all possible vectors* $\mathbf{v}$:

$$\boxed{Q_{\text{after}} = Q_{\text{rot}} Q_{\text{before}}} \tag{3.11}$$

This is the expression for the orientation of the voxel after sample rotation.

Given a pair of 2D source and target microstructures, we now turn to the problem of actually determining the rigid body transformation of the source that brings it into alignment with the target. This step is preliminary in performing a full 3D volume alignment. We start by translating the source so that its centroid coincides with that of the target. The remaining alignment simply involves rotation of the source about the new common centroid until sufficient coincidence is achieved with the target. This can be done in many ways, the most robust being suggested by minimizing the voxel-to-voxel misorientation between the source and the translated target. We opt for a simpler metric that maximizes the number of overlapping 'fit' voxels by rotation about the centroid, in favor of the more complicated orientation-based registration in the second step. While this is a faster computation, it relies heavily on features

that break the rotational symmetry of the microstructure. This could be anything from fiducial markers on the sample, to notches or bulges on one side of the sample resulting from uneven machining.

3.3.2 Single grain alignment

The second step in registration is the more complicated three-dimensional alignment of two microstructure volumes. This follows the intermediate step described in Subsection 3.3.1 in which the entire source microstructure underwent a rigid body transformation that aligned one of its layers with the corresponding layer in the target microstructure. We use the new centroid $\boldsymbol{r}_{CM}$ as the center of rotation of the entire 3D source volume *i.e.* it is about this point that we rotate the source microstructure in the next step. We would hence prefer this coinciding layer to be in the middle of both microstructures.

After the layer registration we pick a single grain that is present in both volumes and rotate the source about $\boldsymbol{r}_{CM}$ so that the two orientations of the grain coincide. In practice this can be done with each of N grains in turn identified as present in both volumes, and choosing the rotation that causes the least aggregate misorientation of all N grains. In Chapter 6, we compare the misorientations of $N = 7231$ grains that were identified by hand as being in both volumes, before and after the 3D alignment. We demonstrate that the misorientations lie well within the angular resolution of the nf-HEDM experiment and for all practical purposes are aligned.

3.4 Initial meshing

Central to the subsequent grain boundary geometry and transport analysis is the presence of a pliable mesh on these interfaces. We demand of such a mesh the following bookkeeping requirements:

- Each mesh node is unambiguously classified as belonging to a grain boundary interior, triple line or quad point.

- Each interior mesh element is unambiguously associated with a single pair of grains, corresponding to those on opposite sides of a grain boundary.

- Each edge of a mesh element along a triple line is associated with exactly three grains, the ones neighboring it.

- Each node corresponding to a quad point be associated with a unique set of four grains, the ones in contact with it.
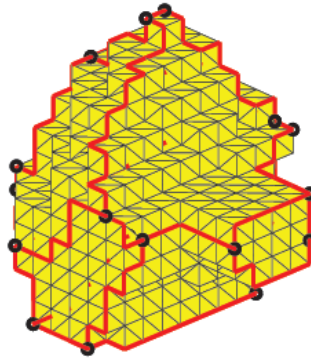
Figure 3.8: Stepped mesh of a single grain. This mesh is the input to the smoothing algorithm. The red lines signify edges identified as triple lines while the black dots are identified as quad points.

These requirements are sufficient to obtain an unambiguous boundary sampling and local connectivity in order to perform more advanced operations like surface smoothing (as described in Chapter 4) and boundary transport. The smoothing implements a technique that preserves the number of nodes and connectivity in the original mesh and simply moves the nodes around. In this section we describe a simple technique to obtain such a preliminary mesh.

We start with the microstructure data on a Cartesian grid with cubic voxels, as obtained by re-rastering the raw output of the 'IceNine' program (Chapter 2). Each voxel is associated with an orientation and a unique integer identification for the grain it belongs to. Voxels along a grain boundary are identified by whether they have neighbors of a different grain identification (specifically, whether they share a face). The vertices of these voxels common to such neighboring voxels form the nodes of our preliminary mesh, and their common faces form the area elements. The triangulation is obtained by dividing each square face into two isosceles triangles (Figure 3.8). This 'QuickMesh' routine is already implemented in the open-source Dream.3D package [21] and satisfies the bookkeeping requirements laid out earlier. The mesh returned by QuickMesh is highly stepped and is by no means representative of a smooth grain boundary. The smoothing algorithm is addressed in Chapter 4.

3.5 Linear optimization

We describe briefly in this section the theory of constrained optimization of multi-variable functions with a special focus on linear optimization and methods to solve a linear programming problem. The application of linear optimization to front-tracking

and interface velocity computations is discussed in Chapter 5. The treatment presented here is by no means rigorous or complete; The complete theory of numerical optimization is a mathematically rich topic with applications in virtually every quantitative field from science and engineering to commerce and logistics. Only the components of the theory relevant to our specific application are discussed here. We begin with a few preliminaries:

1. All optimization problems, whether minimization or maximization, can be cast as that of the minimization of an objective function $f : \mathbb{R}^N \longrightarrow \mathbb{R}$ subject to M constraints defined by the functions $f_i : \mathbb{R}^N \longrightarrow \mathbb{R}$ such that $f_i(\mathbf{x}) \leq 0$; mathematically the problem of finding $\mathbf{x}^* \in \mathbb{R}^N$ such that:

$$\mathbf{x}^* = \arg\min_{\mathbf{x}} f(\mathbf{x})$$

$$\text{subject to: } f_i(\mathbf{x}) \leq 0 \ \forall i = 1, \ 2, \ \ldots, \ M$$

2. The region bound by $f_i(\mathbf{x}) \leq 0$ is called the feasible region $\mathcal{D}$. In order to find a unique minimum $\mathbf{x}^* \in \mathcal{D}$, we require that the domain $\mathcal{D}$ and the objective function $f(\mathbf{x})$ be *convex*, that is, $\forall \ \mathbf{x}, \ \mathbf{y} \in \mathcal{D}$ and $0 \leq \epsilon \leq 1$,

   - $(1 - \epsilon)\mathbf{x} + \epsilon\mathbf{y} \in \mathcal{D}$
   - $f\left((1 - \epsilon)\mathbf{x} + \epsilon\mathbf{y}\right) \leq (1 - \epsilon)f(\mathbf{x}) + \epsilon f(\mathbf{y})$

   The interested reader is referred to the popular treatise by Boyd [22] for further instruction on the theory of convex optimization.

3. The case of linear objective function and constraints is of special interest to us. In this case the optimization of an objective function of N unknowns can be written in canonical form as:

$$\text{Maximize } f(\mathbf{x}) \equiv \mathbf{c}^T\mathbf{x} \tag{3.12}$$

$$\text{subject to: } A\mathbf{x} \leq \mathbf{b} \tag{3.13}$$

$$\text{and } \mathbf{x} \geq 0 \tag{3.14}$$

   where $\mathbf{b}$ and $\mathbf{c}$ are constant vectors of size M and N respectively (M is the number of nontrivial constraints), while A is an $M \times N$-matrix of coefficients of the non-trivial constraints. We also note that maximization of $f(\mathbf{x})$ is equivalent to minimizing $-f(\mathbf{x})$ subject to the same constraints.

From here on in we focus on linear optimization. We see that a linear function is trivially convex. The set of constraints $\mathbf{x} \geq 0$ and $A\mathbf{x} = \mathbf{b}$ can be shown to bound a convex feasible region $\mathcal{D}$ that is a polytope in N dimensions, known as a *simplex*. The set of points at which objective function $f(x) = \mathbf{c}^T\mathbf{x} = \sum_i c_i x_i$ is at a fixed value, is an N-dimensional plane. It can be shown that the plane $\mathbf{c}^T\mathbf{x} = \mathbf{c}^T\mathbf{x}^*$ (where
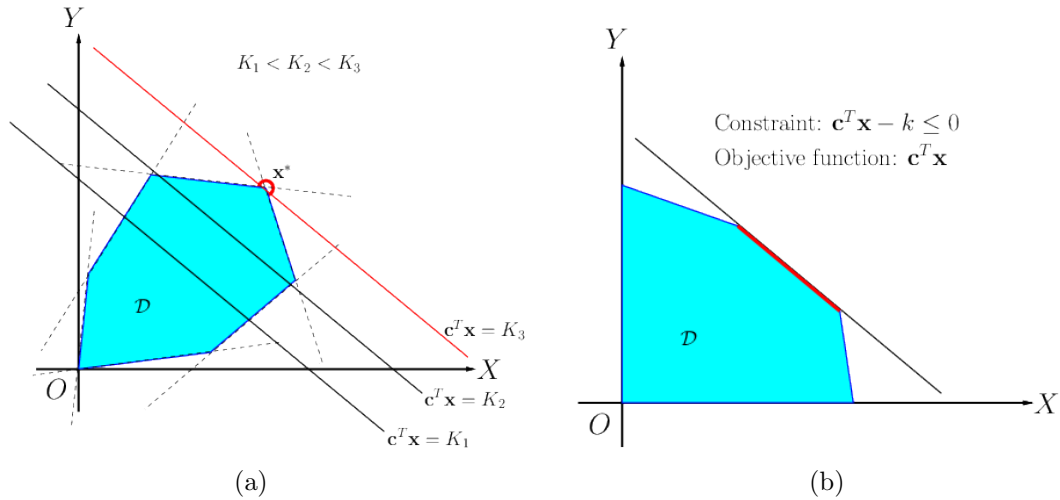
Figure 3.9: **(a)** A two-dimensional case of linear optimization with the feasible region $\mathcal{D}$ shown in shaded color. $\mathbf{c}^T\mathbf{x} = K$ denotes the family of straight lines represented by the objective function, whose value K is to be maximized. The maximum value of K that falls in the feasible region is precisely at the maximizer $\mathbf{x}^*$, which is a vertex of the simplex. **(b)** A case of an ill-posed problem in which the expression for one of the linear constraints is the same as the linear objective function. In this case the maximizer is not unique, in fact every point on the red line is a solution to the problem.

$\mathbf{x}^* = \arg\max_{\mathbf{x}} f(\mathbf{x}))$ touches the simplex at exactly one vertex (barring the case of ill-posed problems). Thus, the optimal solution $\mathbf{x}^*$ lies on one of the vertices of the simplex (Figure 3.9).

We now give the basic principles behind two popular methods of solving a linear optimization problem: the simplex and interior point methods.

3.5.1 The simplex algorithm

The simplex method was developed by George Dantzig [23]. It is an iterative method that approaches the simplex vertex that corresponds to the maximizer by starting at a convenient vertex (usually the origin $\mathbf{x} = 0$) and stepping to adjoining vertices in the direction of maximum increase of the objective function. It can be shown that given a vertex of the simplex that is not the maximizer, there is at least one connected edge along which the objective function is strictly increasing. The simplex method approaches the optimum along the surface of the simplex by traversing each such successive edge. It time-scales relatively inefficiently with increasing number of unknowns compared with more modern algorithms. Currently linear optimization problems are solved with the much more efficient interior point methods.

3.5.2 Interior point methods

The rise of popularity of the interior point methods began with a paper by Narendra Karmarkar [24] which described a polynomial-time algorithm that was a marked improvement from an earlier suggested algorithm by John von Neumann [25]. A good review of interior point methods is given by Potra and Wright [26]. As opposed to simplex methods, interior points methods traverse the interior of the simplex along the 'central path' to reach the optimum. This results in a marked increase in efficiency for large optimization problems. The central path is characterized by the points $\mathbf{x}^* = \mathbf{x}^*(\mu)$ such that:

$$\mathbf{x}^*(\mu) = \arg\max_{\mathbf{x}} f_{LB}(\mathbf{x}; \mu) \tag{3.15}$$

$$f_{LB}(\mathbf{x}; \mu) = f(\mathbf{x}) - \mu \sum_{i=1}^{M} \log\left(-f_i(\mathbf{x})\right) \tag{3.16}$$

This linear optimization algorithm was implemented with the GNU Linear Programming Kit (GLPK) C++ software package with wrappers bindings to call the routine from Matlab.

Chapter 4

Hierarchical smoothing

The morphology of surfaces and interfaces has garnered great interest in many fields of scientific and engineering research. Such studies have implications in applied physics, materials science, biology, pharmacology, chemical engineering and computer vision [27, 28, 29]. A vast part of this research is predicated on the proper imaging of interfaces in the medium of interest. Interfacial networks are composed of two-dimensional, potentially curved interfaces that separate two distinct regions of homogeneous matter, such as gas in bubble foams, or phases or crystalline orientations in solids. We use in this paper language relevant to interfaces in polycrystalline materials but the methods described are equally applicable in other fields by straightforward adaptation of the terminology. The three dimensional entities with more or less uniform crystalline characteristics henceforth will be referred to as 'grains'. The grain boundaries terminate at triple lines where three grains meet and triple lines terminate typically at quadruple or 'quad' points.

A particular type of grain boundary can be specified by five parameters on the meso-scale where 'meso-' refers to a length scale that is large compared to interatomic distances but small compared to a typical grain size. Among the several possible parameterizations; we choose the set of three specifying the relative crystal orientations of the grains, and two specifying the local normal direction relative to the crystal axes in one of the grains. The normal direction in the other crystal frame can be computed from these five parameters. This parameterization ignores a microscopic relative translation on the atomic scale. The set of these five parameters is said to specify the grain boundary character (GBC). Note that the character between two grains can vary over the two-dimensional boundary between them because, while the misorientation is fixed, the local normal typically varies significantly over a curved grain surface. Similar characterizations can be made for triple lines (two misorientations and a tangent line) and quad points (three misorientations). Finally, we note that crystal symmetry is typically exploited to reduce these specifications to unique 'fundamental zones' that span physically distinct ranges of orientations or misorientations.

Whether from a basic or applied science viewpoint, the importance of characterizing grain boundaries in this manner cannot be overstated. In polycrystalline materials, the local interfacial energy density and mobility are known to be sensitive to the five grain boundary parameters at each location [30, 31, 32, 33]. It also informs applications like grain boundary engineering whose eventual goal is to precisely manipulate bulk material properties [34, 35, 36, 37]. Further, it is well-known that the topological elements of a grain boundary network like triple junctions and quad points are hotbeds of activity with respect to precipitate diffusion [38, 39, 40] and strain accumulation [41, 42]. Real grain boundary networks are usually the starting point for atomistic and continuum simulations of microstructure evolution, the physics of which is most difficult to model at triple lines and quad points.

All these applications are predicated upon measurements of the various topological features of a grain boundary network, which are inevitably subject to noise, whether through experimental resolution or image gridding. This necessitates the use of a smoothing routine prior to any further analysis. Owing to the diverse roles of topological elements such as triple lines and quad points in microstructure phenomenology, an important motivation for this novel smoothing technique and other recent ones [43] is to give them their due importance through explicit denoising.

Other factors motivating this work are:

- Unlike voxelized images of most everyday objects, there exists no general intuition for the form of a grain in a sample, and therefore a grain boundary. In the former case, iterative smoothing algorithms such as Laplace and Taubin smoothing [44] yield an acceptable result that is partially helped along by the user's advance knowledge of the object in question. However these methods can suffer from under- or over-smoothing if the number of iterations or step size are not chosen properly.

- Explicit modeling techniques [45] more often than not belie the sheer variety in the observed structure of grain boundaries and network topologies.

- Existing nonparametric techniques [46] require the use of a smoothing window of a user-defined size.

The methodology described here internally optimizes a compromise between fidelity to the input data points and a constrained Laplacian smoothing. An objective function is minimized with respect to this compromise. The algorithm requires no user input in terms of smoothing parameters, only that the connectivity of the nodes be specified in advance, in the form of a graph. We distinguish the type of kernel resulting from graph-connectedness to a given node from a fixed-size window centered on that node since the former, which we rely upon, does not take into consideration the physical distance between neighboring nodes, and only keeps track of the connectivity.

We first describe the topological hierarchy in general terms and then address the smoothing procedure, which is a modification of Laplacian smoothing of a set of

meshed surface points. This is followed by the application of the smoothing algorithm to pixelated versions of easily parameterized geometric primitives, in particular circles, spheres and cylinders. Post-smoothing errors are quantified in terms of estimated sizes of these primitives as well as estimated normals for specific geometries. We then address specific cases of interest in meso-scale materials science: two- and three-dimensional grain boundary networks. The former finds relevance in the study of thin films and the latter in that of bulk material behavior. We demonstrate how the user is freed from the largely intuitive choices of smoothing parameters that is characteristic of iterative or windowed techniques. Maximizing the extent of automation in these things is of great importance to software pipelines that streamline the processing and analysis of digital microstructure data [21]. The application of the resultant smoothed meshes to finite element calculations is also briefly discussed.

4.1   General formalism

We consider a set of N noisy sample points in $\mathcal{D}$-dimensional Cartesian coordinates: $\mathbb{X} = \{\boldsymbol{x}_1, \boldsymbol{x}_2, \ldots, \boldsymbol{x}_N\}$ that denote an imaged grain boundary. A subset $\mathbb{X}_S \subset \mathbb{X}$ of these points is tagged as a 'perimeter' that samples the edges of the grain boundary with the same grid resolution as the interior. We also assume a connectivity scheme for every point relative to the others, described by a graph Laplacian matrix $L^{(0)}$:

$$L_{ij}^{(0)} = \begin{cases} N(i) & \text{If } i = j \\ -I(j; i) & \text{if } i \neq j \end{cases}$$

where $N(i)$ is the number of connected components of the i-th element and $I(j; i)$ is an indicator function that is 1 if component j is connected to component i and 0 otherwise. We require that all $\boldsymbol{x}_i \in \mathbb{X}_S$ remain constrained to their initial positions while the $\boldsymbol{x}_i \in \mathbb{X} - \mathbb{X}_S$ are smoothed, all the while adhering to the same node connectivity. We denote this smoothing operation notionally by $SMOOTH(\mathbb{X}, \mathbb{X}_S)$.

As a general rule, we enter points $\boldsymbol{x}_i$ into our imagined hierarchy such that all $\boldsymbol{x}_i \in \mathbb{X}_S$ are at one level above all $\boldsymbol{x}_i \in \mathbb{X} - \mathbb{X}_S$. Notationally the hierarchy level or 'rank' is denoted by a function $H(\boldsymbol{x}_i)$ such that $H(\mathbb{X}_S) = 1 + H(\mathbb{X} - \mathbb{X}_S)$; the sole purpose of H being to distinguish points of different ranks and the actual returned value being a matter of choice.
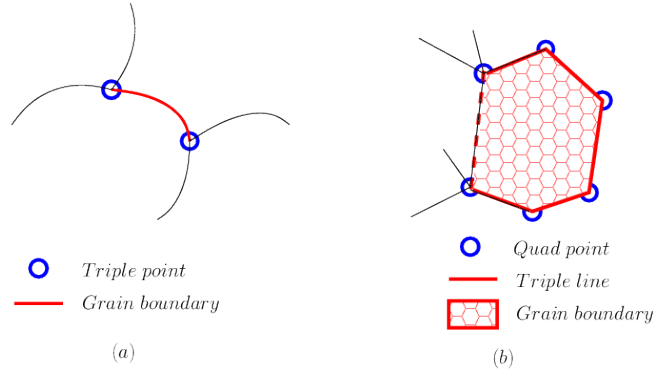
Figure 4.1: **(a)** Hierarchy for a two-dimensional microstructure in which all sample points in the interior of the grain boundary belong to $\mathbb{X} - \mathbb{X}_S$ and the triple points belong to $\mathbb{X}_S$; **(b)** Three-dimensional microstructure in which the interior points of the grain boundary belong to $\mathbb{X} - \mathbb{X}_S$ while the boundary perimeter points belong to $\mathbb{X}_S$. The perimeter points themselves can be seen to belong to a union of two-dimensional hierarchies of the type described in **(a)**.

Figure 4.1 visualizes two common systems with different hierarchy sizes. Keeping in mind that in an interface network in $\mathcal{D}$-dimensional space there exist in general objects of dimensionality $d = 0, 1, \ldots, \mathcal{D} - 1$, we define the rank function $H(\boldsymbol{x}_i) \equiv \mathcal{D} - d$, where d corresponds to the lowest-dimensional object in the network to which $\boldsymbol{x}_i$ belongs. For example, a triple point in a 2-dimensional image is assigned a rank of 2 because it is a zero-dimensional object, while a grain boundary interior point has a rank of 1.

Table 4.1: Hierarchy table for a 2-dimensional network

Type of $\boldsymbol{x}_i$	d	$H(\boldsymbol{x}_i)$
Triple point	0	2
boundary interior	1	1

Table 4.2: Hierarchy table for a 3-dimensional network

Type of $\boldsymbol{x}_i$	d	$H(\boldsymbol{x}_i)$
Quad point	0	3
Triple line	1	2
Boundary interior	2	1

Tables 4.1 and 4.2 show the general rule that for a given network, $d_i + H(\boldsymbol{x}_i) = \mathcal{D}$. We note that the feature of a topological element that decides its rank is its

dimensionality rather than its name. For example, if a quad line existed in a network for which $\mathcal{D} = 3$ (*i.e.* intersection of four grain boundary surfaces) its rank would be 2. Based upon these definitions, the smoothing algorithm for a set of N interface points in a $\mathcal{D}$-dimensional network is as follows:

> **START**
> $N_h \leftarrow$ *Max. rank in hierarchy*
> $MOV \leftarrow \{\}$, $FIX \leftarrow \{\}$
> **while** $N_h > 0$ **do**
> $MOV \leftarrow MOV \cup \{\boldsymbol{x}_i \,|\, H(\boldsymbol{x}_i) = N_h\}$
> $SMOOTH\,(MOV, FIX)$
> $FIX \leftarrow FIX \cup MOV$
> $N_h \leftarrow N_h - 1$
> **end while**
> **return** MOV
> **STOP**

In summary, points of rank N_h are smoothed while holding in place all previously smoothed connected points of rank $N_h' > N_h$, with highest-rank points essentially undergoing unconstrained smoothing (since FIX is initially an empty set). If the highest rank elements have $d = 0$ as do quad points when $\mathcal{D} = 3$ or triple points when $\mathcal{D} = 2$, then one can skip 'smoothing' them altogether. This scheme gives the aforementioned topological features their due importance relative to one another. The prerequisite of having points labeled according to their rank in the hierarchy is readily achievable by nearest neighbor-based clustering algorithms [21].

4.2 Constrained smoothing

$SMOOTH(\mathbb{X}, \mathbb{X}_S)$ is based on a nonparametric regression that involves penalizing, in Cartesian component-by-component fashion, the displacement between each estimated smoothed point and its *unsmoothed* neighbors. If M of N initial points are mobile $(M < N)$, a measure of the nearest neighbor fluctuations of each Cartesian component s_i of $\boldsymbol{x}_i \in \mathbb{X}$ can be estimated with $\left| L\boldsymbol{\sigma} + \mathbf{s}^{(b)} \right|^2$, where $\boldsymbol{\sigma} \equiv [s_1 \; s_2 \; \dots \; s_M]^T$ represents a vector of only the s_i that require smoothing, L is a modified graph Laplacian operator expressing the connectivity of the mobile nodes and $\mathbf{s}^{(b)}$ denotes constants that are determined from the remaining $\boldsymbol{x}_i \in \mathbb{X}_S$. $\mathbf{s}^{(b)}$ in fact specifies the Dirichlet boundary conditions to Laplace's equation. Specific examples of L and $\mathbf{s}^{(b)}$ are described presently. In the case of no constraints, $M = N$, $\mathbb{X}_S$ is an empty set and L is the full graph Laplacian. $SMOOTH$ performs simultaneous filtering of each component $s_i \rightarrow \chi_i$ by negotiating a tradeoff between fidelity to the raw data and minimization of fluctuations between *smoothed* neighbors through a scalar control

parameter ϵ. A control function $F(\boldsymbol{\chi})$ is defined to this end:

$$F(\boldsymbol{\chi}) = (1 - \epsilon) \left|\boldsymbol{\chi} - \boldsymbol{\sigma}\right|^2 + \epsilon \left|L\boldsymbol{\chi} + \mathbf{s}^{(b)}\right|^2 \tag{4.1}$$
$$\text{where } 0 \le \epsilon \le 1$$

Here $\boldsymbol{\chi} \equiv [\chi_1 \ \chi_2 \ \ldots \ \chi_M]^T$ represents the array corresponding to $\boldsymbol{\sigma}$ that is further along in the smoothing process. At the extreme ϵ-values of 0 and 1, the minimizer $\boldsymbol{\chi}_{opt}(\epsilon)$ of $F(\boldsymbol{\chi})$ respectively favors complete data fidelity ($\boldsymbol{\chi} = \boldsymbol{\sigma}$) and complete Laplace-smoothing ($L^T L \boldsymbol{\chi} + L^T \mathbf{s}^{(b)} = 0$). We further define an objective function that penalizes fluctuations between each smoothed point and its nearest *unsmoothed* neighbors based on the connectivity specified in the full $N \times N$ graph Laplacian $L^{(0)}$:

$$F_{obj}(\boldsymbol{\chi}(\epsilon)) = \sum_{i=1}^{N} \left| \sum_{\{j \mid L_{ij}^{(0)} = -1\}} \chi_i - \sigma_j \right|^2 \tag{4.2}$$

Crucially, we require that the minimizer of F_{obj} be reached by always satisfying the optimality condition of the control function in (4.1) with respect to $\boldsymbol{\chi}$ and therefore indirectly through variation of the parameter ϵ alone. This makes the smoothing operation on the s_i a one-dimensional minimization in ϵ that can easily be achieved by a binary search in the interval $[0, 1]$. Briefly, the objective function F_{obj} is the actual quantity being minimized in the regression, but the path taken in the objective function landscape is decided by the control function F.

We define the matrix $\mathbf{x}_0$ of unsmoothed starting points as having N rows and $\mathcal{D}$ columns where $\mathcal{D}$ is the dimensionality of the points. Similarly we define the identically-sized matrix $\boldsymbol{\chi}^{(0)}$ as the solution resulting from applying $SMOOTH$ to $\mathbf{x}_0$. We define D and A as the diagonal and adjacency matrices respectively of $L^{(0)}$. We rely on the following intermediate definitions to obtain the reduced Laplacian and constant matrices:

1. Let the integer set $\mathbb{I}$ denote the indices of the points that remain fixed (*i.e.* $\mathbb{I} \equiv \{i \mid \boldsymbol{x}_i \in \mathbb{X}_S\}$ or equivalently $\mathbb{X}_S \equiv \{\boldsymbol{x}_i \mid i \in \mathbb{I}\}$)

2. If for an integer $N > 0$, $\mathbb{S} = \{n_1, \ n_2, \ldots\}$ is an integer set such that $1 \le n_i \le N \ \forall n_i \in \mathbb{S}$, then let $\widetilde{\mathbb{S}} \equiv \{i \in \mathbb{Z} \mid 1 \le i \le N, \ i \notin \mathbb{S}\}$, *i.e.* the complement of $\mathbb{S}$ with respect to N.

3. Let the submatrix of a matrix $\mathbb{M}$ formed by:

   - the rows whose indices are in $\mathbb{S}$ be denoted by $SM_{\text{rows}}(\mathbb{M}, \mathbb{S})$.

   - the rows *and* columns whose indices are in $\mathbb{S}$ be denoted by $SM_{\text{both}}(\mathbb{M}, \mathbb{S})$.

then the reduced Laplacian and constant matrix are defined:

$$L = SM_{\text{both}}\left(L^{(0)}, \widetilde{\mathbb{I}}\right) \tag{4.3}$$

$$\mathbf{s}^{(b)} = SM_{\text{rows}}\left(R\mathbf{x}_0, \widetilde{\mathbb{I}}\right) \tag{4.4}$$

where R is defined by: $R_{ij} = \begin{cases} L_{ij}^{(0)} & \text{if } j \in \mathbb{I} \\ 0 & \text{otherwise} \end{cases}$

For example, if $N = 5$ points $\{\boldsymbol{x}_i = [x_i \ y_i \ z_i]^T \,|\, x_i, y_i, z_i \in \mathbb{R}, \ i = 1, 2, \ldots, 5\}$ in $\mathcal{D} = 3$ dimensions are to be smoothed in which the $\boldsymbol{x}_i$ are connected sequentially with $\boldsymbol{x}_1$ and $\boldsymbol{x}_5$ to be fixed, then:

$$\mathbb{I} = \{1, \ 5\}, \ \widetilde{\mathbb{I}} = \{2, \ 3, \ 4\}$$

$$\mathbf{x}_0 = [\boldsymbol{x}_1 \ \boldsymbol{x}_2 \ \boldsymbol{x}_3 \ \boldsymbol{x}_4 \ \boldsymbol{x}_5]_{3\times5}^T, \ \mathbf{x} = SM_{\text{rows}}\left(\mathbf{x}_0, \widetilde{\mathbb{I}}\right) = [\boldsymbol{x}_2 \ \boldsymbol{x}_3 \ \boldsymbol{x}_4]_{3\times3}^T$$

$$L^{(0)} = \begin{bmatrix} 1 & -1 & 0 & 0 & 0 \\ -1 & 2 & -1 & 0 & 0 \\ 0 & -1 & 2 & -1 & 0 \\ 0 & 0 & -1 & 2 & -1 \\ 0 & 0 & 0 & -1 & 1 \end{bmatrix}, \ L = \begin{bmatrix} 2 & -1 & 0 \\ -1 & 2 & -1 \\ 0 & -1 & 2 \end{bmatrix}$$

$$\mathbf{s}^{(b)} = \begin{bmatrix} -x_1 & -y_1 & -z_1 \\ 0 & 0 & 0 \\ -x_5 & -y_5 & -z_5 \end{bmatrix}$$

$$D_{ij} = \begin{cases} L_{ij}^{(0)} & \text{If } i = j \\ 0 & \text{Otherwise} \end{cases}$$

$$A_{ij} = \begin{cases} L_{ij}^{(0)} & \text{if } j = i \pm 1 \\ 0 & \text{Otherwise} \end{cases}$$

$$\boldsymbol{\chi}^{(0)} \equiv \left[\boldsymbol{x}_1 \ \boldsymbol{\chi}^T \ \boldsymbol{x}_5\right]^T \tag{4.5}$$

Equation (4.5) denotes the full smoothed solution including the constrained points. If $\boldsymbol{\chi}^{(0)}$ and $\boldsymbol{\chi}$ respectively satisfy the free-boundary and constrained Laplace equations, then is it clear that $L^{(0)}\boldsymbol{\chi}^{(0)} = 0_{5\times3}$ and $L\boldsymbol{\chi} + \mathbf{s}^{(b)} = 0_{3\times3}$. The smoothing problem is stated more compactly as the following optimization problem:

$$F_{obj}(\boldsymbol{\chi}^{(0)}) = \text{Tr}\left[\left(D\boldsymbol{\chi}^{(0)} - A\mathbf{x}_0\right)^T \left(D\boldsymbol{\chi}^{(0)} - A\mathbf{x}_0\right)\right] \tag{4.6}$$

$$\boldsymbol{\chi}(\epsilon) = \left[(1-\epsilon)\mathbb{1} + \epsilon L^T L\right]^{-1} \left((1-\epsilon)\mathbf{x} - \epsilon L^T \mathbf{s}^{(b)}\right) \tag{4.7}$$

$$\epsilon_{opt} = \arg\min_{\epsilon} F_{obj}\left(\boldsymbol{\chi}^{(0)}(\epsilon)\right)$$

$$\boldsymbol{\chi}_{opt}^{(0)} = \boldsymbol{\chi}^{(0)}(\epsilon_{opt})$$

We note from Equation (4.7), which is derived from the minimizer of the control function in Equation (4.1), that $\boldsymbol{\chi}(\epsilon)$ is an $M \times \mathcal{D}$ matrix and that in Equation (4.6) the argument of the trace operator is a $\mathcal{D} \times \mathcal{D}$ symmetric matrix with non-negative eigenvalues (the case of zero eigenvalues implies that the sample points are flattened in at least one dimension). Significantly, the trace of this matrix and therefore the objective function itself represents the aggregate squared Euclidean distance of each node from its unsmoothed neighbors. The equivalence of Equations (4.2) and (4.6) is seen in the simple one-dimensional smoothing example ($\mathcal{D} = 1$): $\boldsymbol{\sigma}^{(0)} = [\ldots \sigma_{N-1}\ \sigma_N\ \sigma_{N+1} \ldots]^T \longrightarrow \boldsymbol{\chi}^{(0)} = [\ldots \chi_{N-1}\ \chi_N\ \chi_{N+1} \ldots]^T$. Each column in in the $N \times \mathcal{D}$-matrix $D\boldsymbol{\chi}^{(0)} - A\mathbf{x}_0$ corresponds to one such Cartesian component in the sample frame of reference and each element is of the form $2\chi_N - (\sigma_{N-1} + \sigma_{N+1})$. This is precisely the argument of the $|\cdot|^2$ operation in (4.2). The objective function in (4.6) represents the operation in (4.2) being performed simultaneously on all $\mathcal{D}$ Cartesian components. Minimizing them simultaneously is completely equivalent to minimizing the (reference frame-invariant) trace of the matrix $\left(D\boldsymbol{\chi}^{(0)} - A\mathbf{x}_0\right)^T \left(D\boldsymbol{\chi}^{(0)} - A\mathbf{x}_0\right)$.

The $SMOOTH$ algorithm is finally given by:

START
$\epsilon \leftarrow 0.5, \Delta\epsilon \leftarrow 0.25$
$\boldsymbol{\chi} \leftarrow \left[(1 - \epsilon)\mathbb{1} + \epsilon L^T L\right]^{-1} \left[(1 - \epsilon)\mathbf{x} - \epsilon L^T \mathbf{s}^{(b)}\right]$
$\boldsymbol{\chi}^{(0)} \leftarrow \boldsymbol{\chi} \cup \mathbb{X}_S$ $\triangleright$ *i.e.* add the points that are held fixed
$F_{\text{obj}} \leftarrow \text{Tr}\left[\left(D\boldsymbol{\chi}^{(0)} - A\mathbf{x}_0\right)^T \left(D\boldsymbol{\chi}^{(0)} - A\mathbf{x}_0\right)\right]$
while $|\partial F_{\text{obj}}/\partial\epsilon| \geq Threshold$ **do**
    if $\partial F_{\text{obj}}/\partial\epsilon > 0$ **then**
        $\epsilon \leftarrow \epsilon - \Delta\epsilon$
    else
        $\epsilon \leftarrow \epsilon + \Delta\epsilon$
    end if
    $\Delta\epsilon \leftarrow \Delta\epsilon/2$
    $\boldsymbol{\chi} \leftarrow \left[(1 - \epsilon)\mathbb{1} + \epsilon L^T L\right]^{-1} \left[(1 - \epsilon)\mathbf{x} - \epsilon L^T \mathbf{s}^{(b)}\right]$
    $\boldsymbol{\chi}^{(0)} \leftarrow \boldsymbol{\chi} \cup \mathbb{X}_S$ $\triangleright$ *i.e.* add the points that are held fixed
    $F_{\text{obj}} \leftarrow \text{Tr}\left[\left(D\boldsymbol{\chi}^{(0)} - A\mathbf{x}_0\right)^T \left(D\boldsymbol{\chi}^{(0)} - A\mathbf{x}_0\right)\right]$
end while
return $\boldsymbol{\chi}^{(0)}$
STOP

The resulting surface consisting of the smoothed points with the preserved original connectivity is nonparametric. Qualitatively, the algorithm attempts to determine the least jagged surface passing in between the sample points, thus maintaining data fidelity. This precludes a major problem in applying iterative Laplace-like techniques, that of over- or under-smoothing. For the applications of $SMOOTH$ in the remainder of this text, the threshold value of $\partial F_{\text{obj}}/\partial\epsilon$ was taken to be 10^{-7}.

We point out that the smoothing scheme outlined in this section allows users

to define the components of the algorithm for specific requirements. For instance, users of mesh smoothing algorithms like finite element method (FEM) might want to explicitly incorporate mesh quality metrics into the objective function as an alternative to remeshing. This in turn may well decide the manner of stepping in the objective function landscape and therefore shape the control function. Our smoothing paradigm permits the flexibility of user-defined objective and control functions, all the while heeding the hierarchy between the components of the grain boundary network. We address the applicability of smoothed meshes obtained from the objective function in Equation (4.6) to finite element applications in Section 4.7.

4.3 *SMOOTH*ing a digitized planar curve

We describe as a first demonstration of $SMOOTH$ the problem of smoothing a set of pixelated points $\mathbb{X} \equiv \{(i, y_i) \,|\, i = 1, 2, \ldots, N \text{ and } s_i \in \mathbb{Z}\}$ representative of a curve in a plane. We list the following general properties of such a set of points:

1. The coordinates are integral multiples of some basis of vectors in the plane. This could indicate either a square or triangular grid as implemented in commercial electron backscatter diffraction (EBSD) [47] software or near-field high-energy diffraction microscopy (nf-HEDM) [7, 8].

2. Every point has at least one nearest neighbor in at least one direction on this integer grid. This is characteristic of discretized sampling of continuous curves and surfaces in general.

Such points can be obtained from pixelated images in standard formats by first generating a phase field (for instance a field of unique integers assigned to each grain), taking the magnitude of the gradient of this field and binarizing it. A morphological 'skeletonizing' operation can then be applied to this binarized field [48, 49, 50]. This same technology is used in the field of biometrics, for example, to thin down high-resolution images of fingerprints to features of single-pixel thickness for further analysis. For nf-HEDM images, one can collect directly the voxel (**vo**lume pi**xel**) edges that border two different grains, as decided by some segmentation criterion. In our example the coordinates of the sample points are integers on a square grid. The image of the curve has been skeletonized to ensure that each sample point has no more than two of the 8 immediate square-grid neighbors belonging to the pixelated line (interior points have two 8-neighbors and the terminal points have one). The results of constrained smoothing on such a pixelated curve is shown in Figure 4.2 with the perimeter points fixed at the unsmoothed grid point locations.
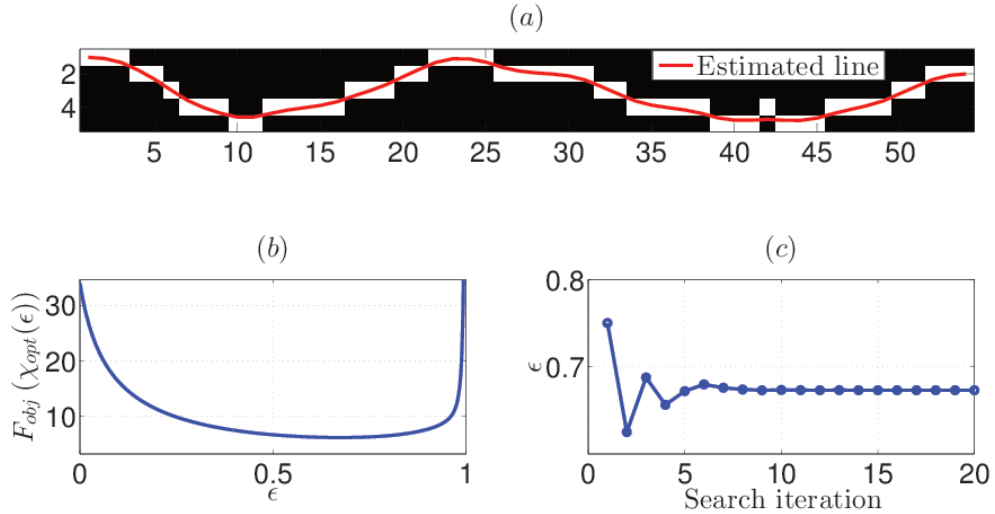
Figure 4.2: **(a)** Pixelated and thinned line and its smooth estimate; **(b)** A plot of the objective function in its domain $[0, 1]$ shows a shallow minimum; **(c)** Search for the optimal value of the control parameter ϵ that strikes the best balance between data fidelity and smoothness.

4.4 *SMOOTH*ing known shapes

In this section the hierarchical $SMOOTH$ algorithm is applied to open surfaces that are geometry primitives in two and three dimensions. Simple parameterizations for these primitives provide a means of comparison with a smoothed solution on a point-to-point basis. We describe trends in the errors for different primitives as a function of voxel density. Focusing attention on open surfaces allows us to simulate smoothing in the presence of topological features characteristic of a grain boundary network. The three primitives chosen are a 2D circle, a 3D sphere, and a 3D cylinder. Surface slices from these primitives were characterized by the following:

- The gridding resolution was chosen in terms of the number of voxels per unit length, N.

- **Circle**: A semicircular arc of unit radius, whose endpoints were reset to unit radius after discretization. These endpoints were held constrained during smoothing.

- **Sphere**: A square patch spanning $100°$ in two mutually perpendicular directions cut out from the surface of a sphere of radius 0.03 units, with the edges of the square treated as triple lines and the vertices as quad points. The quad points alone were constrained to lie on the sphere, while the others were subject to discretization on a cubic lattice.

- **Cylinder**: A rectangular patch cut from the surface of a cylinder of radius 0.03 units, parallel to its axis and spanning 150° along the azimuth. The edges of the rectangle were treated as triple lines and the vertices as quad points. The quad points were constrained to remain on the surface of the cylinder.

The choice of the sphere and cylinder radii are indicative of the typical size of a grain from earlier nf-HEDM measurements [12]. The quality of smoothing was expressed as the error in the estimated radius of the primitive in question. Specific examples smoothing on these primitives are shown in Figure 4.3.
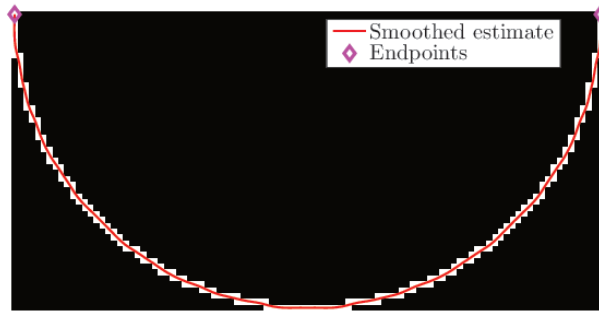
(a)
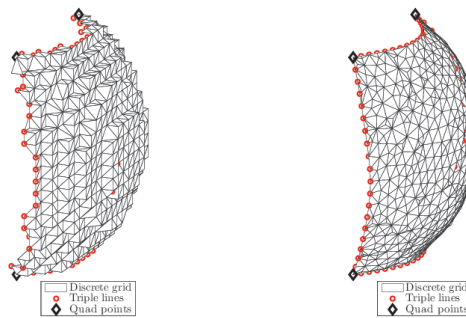
(b)

(c)
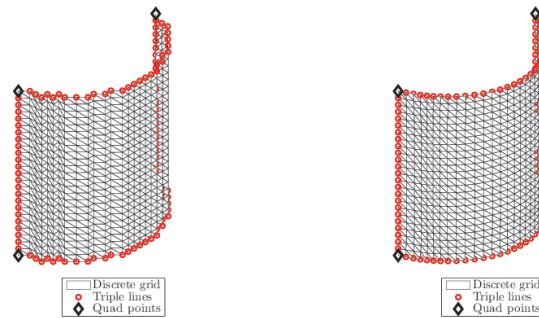
Figure 4.3: **(a)** Semicurcular arc with a 50 pixel radius; **(b)** A discretized spherical patch (400 voxels per unit length) spanning equal angles (100°) in mutually perpendicular directions and its smoothed version; **(b)** A cylindrical patch discretized to 400 voxels per unit length and its smoothed version.

The fidelity of the final smoothed result to the original primitive was quantified in terms of the point-to-point difference in radii of the original and smoothed surfaces. In the case of the sphere and the cylinder, the first spherical and cylindrical polar

coordinates are respectively used (*i.e* r and ρ). Shown in Figure 4.4 are trends in the estimated error $\Delta r \equiv r - r_0$ and its standard deviation σ_r, taken over the smoothed mesh nodes, for all three primitives. If the unit of length is taken to be a millimeter, the relative error in the region between $N = 300$ and $N = 1000$ is particularly relevant for techniques like nf-HEDM since they correspond to a pixel size range of $1\mu m$ to $3.33\mu m$, which brackets the known experimental resolution [12]. For comparison, the radii of the spherical and cylindrical patches were chosen to be $30\mu m$.

(a) (b) (c)

(d) (e) (f)
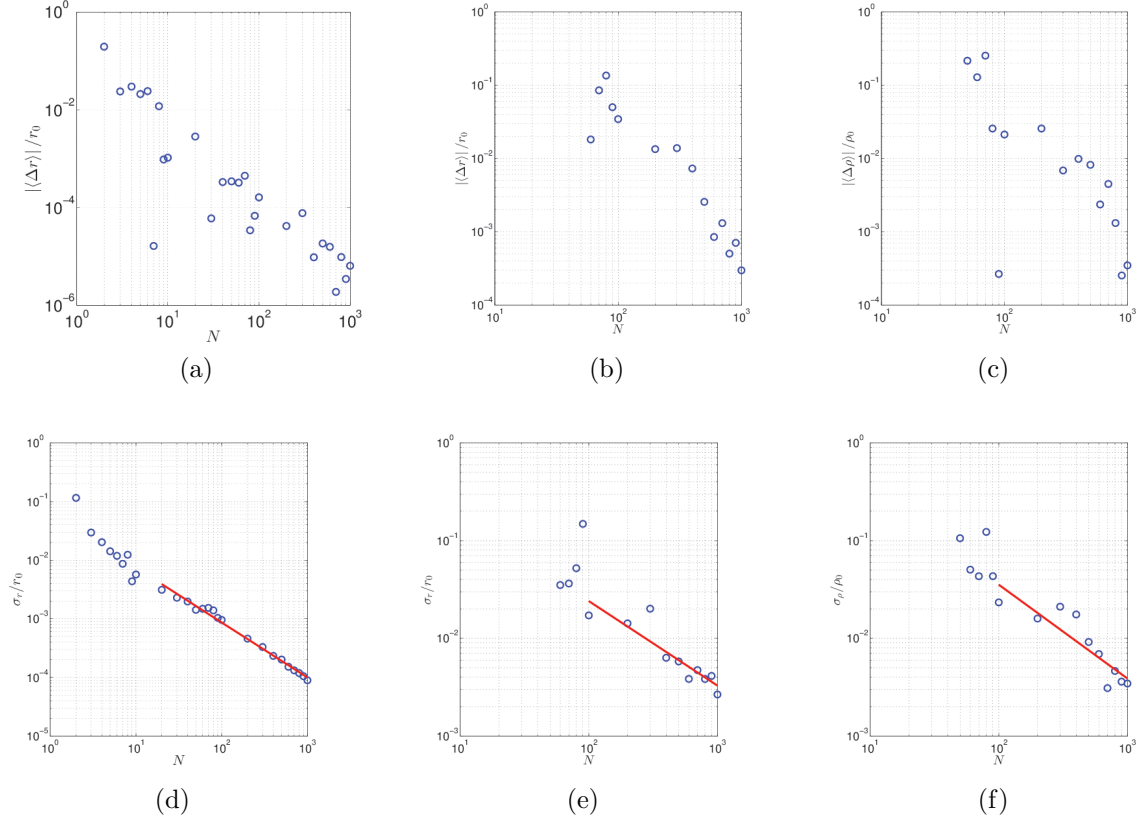
Figure 4.4: Trends in the error in estimated size $\Delta r = r - r_0$ of the (a) circle, (b) sphere and (c) cylinder as a function of voxel density per unit length N. Trends in the error spread $\sqrt{\langle \Delta r^2 \rangle - \langle \Delta r \rangle^2}/r_0$ for the (d) circle, (e) sphere and (f) cylinder as a function of N. The red lines are fits to the power law $\sigma = 10^{p_0} N^{p_1}$ whose determined coefficients are listed in Table 4.3. Not all the points are used in the fits owing to coarse gridding at low values of N.

The power law behavior in the error trends was tested for each primitive as is seen in the straight line fits in Figure 4.4. The coefficients p_0 and p_1 of the estimated power law $f(N) = 10^{p_0} \times N^{p_1}$ are listed in Table 4.3. Of particular interest is p_1 which is seen to lie close to -1 for all three primitives. This is simply explained by the fact

Table 4.3: Estimated power law coefficients of the error trends for various primitives.

Primitive	p_1	p_0
Circle	-0.93724	-1.18898
Sphere	-0.86535	0.11215
Cylinder	-0.96061	0.47041

(a)   (b)
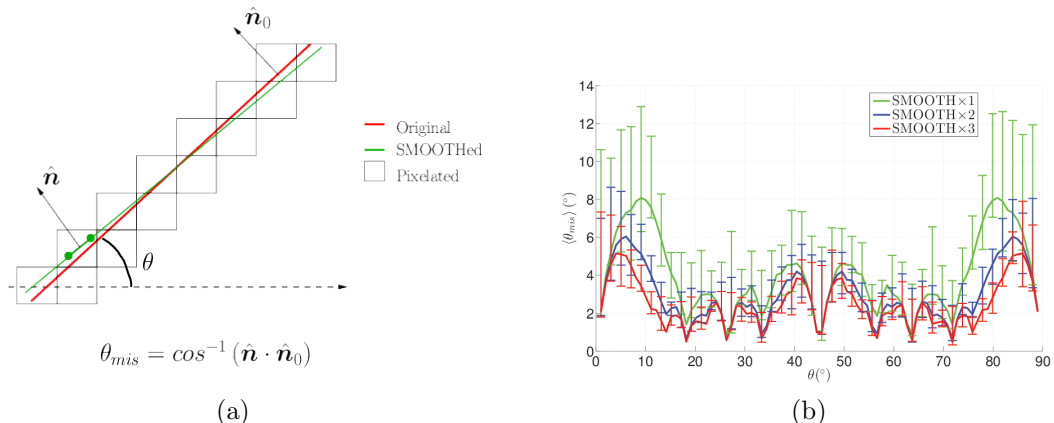
Figure 4.5: Estimation of deviation in expected inclination for a discretization of 600 pixels per unit length, for repeated applications of the $SMOOTH$ algorithm. **(a)** Schematic of a section of the simulated line, **(b)** Mean of θ_{mis} (taken over length of the entire smoothed line) as a function of inclination θ. The error bars denote the standard deviations of the one-sided distribution on either side of the mean.

that the length error is $1/N$, the size of one voxel. The lowered fit quality for the sphere and cylinder is attributed to the difficulty in obtaining a perfect stair-stepped mesh for these primitives. We further note that the relative error for each primitive is around a fraction of a percent ($< 10^{-2}$) at the spatial resolution of nf-HEDM ($1.48\mu m$ or ~ 675 pixels per millimeter).

Another smoothing quality metric that is easily calculated for two dimensions is the error in the local normal of a curve. This is particularly relevant to surface imaging applications. We estimate the local deviation about the known normal of the sections of a pixelated straight line that has been $SMOOTH$ed with its endpoints held at their true positions. This deviation is determined for different inclinations of the original line to the Cartesian grid. A schematic and results for the inclination range of $0°$ to $90°$ is shown in Figure 4.5. It is seen that while the mean deviation varies with the inclination of the original line, it falls within a few degrees of the actual normal which justifies the use of $SMOOTH$ in calculations of grain boundary character distribution [51, 52, 53].

4.5   Results - two-dimensional microstructure smoothing

The constrained smoothing is next demonstrated on a real two-dimensional microstructure imaged with nf-HEDM. The sample points $\mathbf{x}_i \equiv [x_i \ y_i]^T$ of each grain boundary are expressed in integer units of suitable in-plane step size (in this case,

$2\mu m$) and are classified as belonging to a grain interior, grain boundary or triple point depending on the number of unique grains represented in the 8-neighborhood . The optimization is performed simultaneously over x_i and y_i and therefore $\boldsymbol{\chi}^{(0)}$ is an $N \times 2$-matrix. The results on a section of microstructure are shown in Figure 4.6.

4.6   Results - three-dimensional microstructure smoothing

Hierarchical smoothing is demonstrated on select grains of a well-ordered three-dimensional microstructure measured with nf-HEDM and is compared to the results of Laplace smoothing. The prerequisite node connectivity on the grain surfaces was obtained by first segmenting the microstructure into its constituent grains and then triangulating the faces of the cubic voxels along grain boundaries [21]. The result of this operation is a 'quick-and-dirty' Delaunay mesh on stepped grain surfaces characteristic of discrete sampling. A few important points about this bookkeeping process that inform the subsequent smoothing are:

- The grain surface nodes are unambiguously classified into their topological types *i.e.* boundary interiors, triple lines or quad points. It is worth mentioning that the preprocessing described above is external to the hierarchical smoothing algorithm itself and as such is not the focus of this work.

- The meshing and bookkeeping is done in such a manner as to ensure that nodes along triple lines and at quad points are shared between the neighboring topological features.

Figures 4.7, 4.8 and 4.9 show comparisons of hierarchical smoothing with Laplace smoothing in which the ease of movement of the triple points is enhanced by assigning them a greater Laplace smoothing parameter λ. The values of λ for the parent volumes for each of these grains were determined by trial and error (as a user would have to do) by visually minimizing the distortion from the original square-gridded grain. This is a highly inefficient process that is not required in hierarchical smoothing.
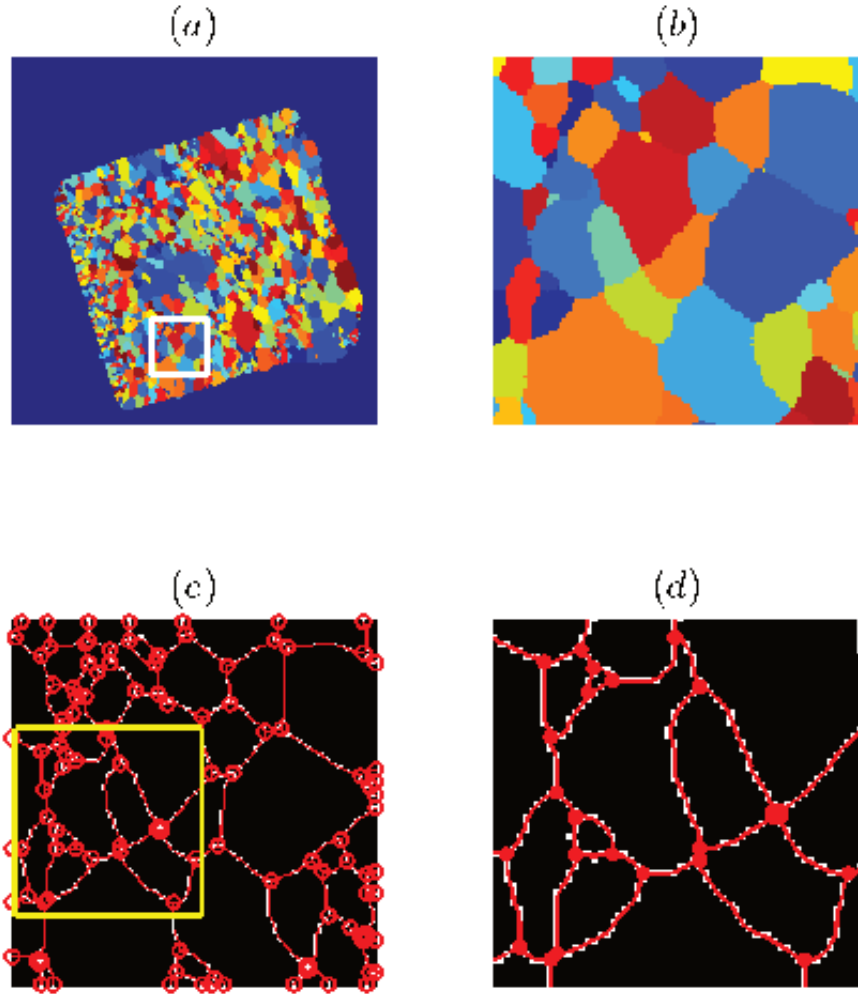
Figure 4.6: **(a)** Discrete phase field of a single layer of well-ordered microstructure imaged by nf-HEDM. Each grain is colored according to a unique integer assigned to it; **(b)** The region of interest in *(a)* zoomed in; **(c)** Image obtained from taking the derivative of the phase field in *(a)* and binarizing it above a chosen threshold, then performing a skeletonizing operation. Triple points were identified as those grain boundary points that have three distinct phase values in their 8-neighborhood, while grain boundary interior points as those having exactly two distinct phase values in their 8-neighborhood. On this is superposed the result of $SMOOTH$ing carried out for each boundary while holding its associated triple points fixed; **(d)** The result of the smoothing operation in the region of interest from *(c)*.
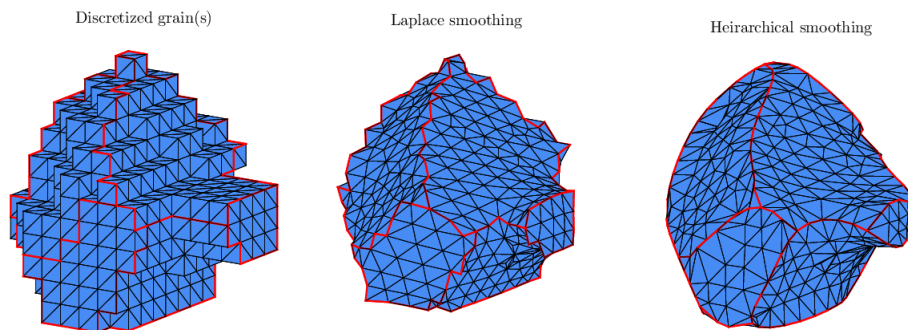
Figure 4.7: Discretized grain mesh smoothed using Laplace smoothing (with 400 iterations and smoothing parameter λ set to 0.025, 0.5 and 0.025 for interior nodes, triple lines and quad points respectively), and parameter-free hierarchical smoothing. The red lines are triple lines.
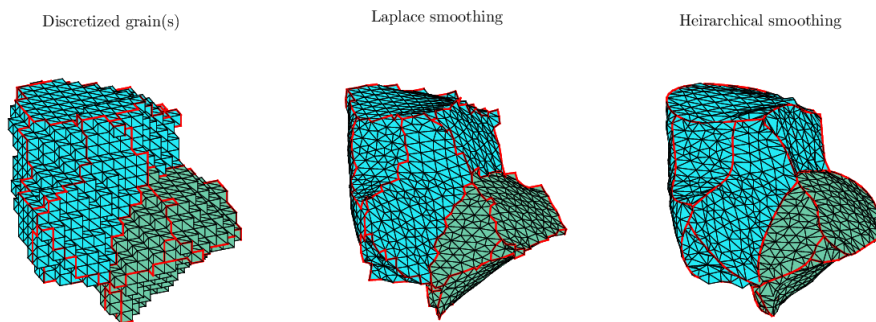
Figure 4.8: Discretized mesh of a pair of neighboring grains smoothed using Laplace smoothing (same parameters as in Figure 4.7) and parameter-free hierarchical smoothing.
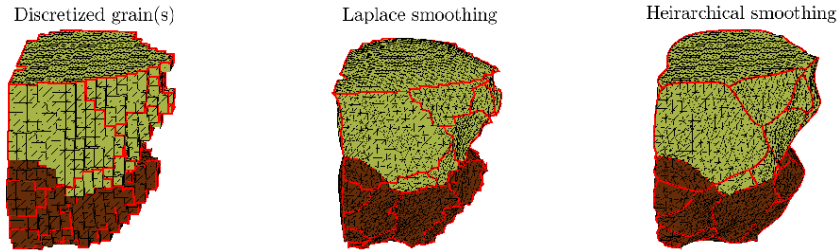
Figure 4.9: A more complicated grain pair structure with a larger number of topological features. In this example, the flatness of the top surface in the discretized grain owing to the grain being on the edge of the sample is preserved with hierarchical smoothing, while Laplace smoothing returns a clearly visible and unphysical bulge along that face.

4.7   Mesh quality

Finally we address the suitability of $SMOOTH$ output for finite element applications, which are predicated on the availability of surface meshes with reasonably isotropic mesh elements (equilateral, in the case of triangular) in order to avoid errors from piecewise linear interpolation. While there exist other sophisticated methods of quantifying the quality of a mesh element [54], we implement a simple metric for triangular elements that tests their closeness to an equilateral triangle [55]. The quality of a triangle of area A and side lengths s_1, s_2 and s_3 is defined to be:

$$Q = \frac{4\sqrt{3}A}{s_1^2 + s_2^2 + s_3^2} \qquad (4.8)$$

which gives $Q = 1$ for an equilateral triangle. Shown in Figure 4.10 are element-wise quality plots of select grains in a 3-dimensional volume. Figure 4.11 histograms the mesh quality over all surface elements in the entire 424 grain volume. The flattening of some of the mesh elements at the triple junctions of the 3-dimensional grains in Figures 4.7, 4.8 and 4.9 is evidenced by the slight peak in the distribution in Figure 4.11 at low qualities (~ 0.1).

4.8   Summary and discussion

A new smoothing technique for interface networks was demonstrated and compared to the performance of an an established but generic smoothing algorithm in current use. The new algorithm organizes the topological elements of the network into an hierarchy depending on which elements physically border other elements and

(a)

(b)

(c)

(d)

Figure 4.10: Mesh quality of select grains in the microstructure volume. The grain in **(d)** is the same as the one in Figure 4.7.
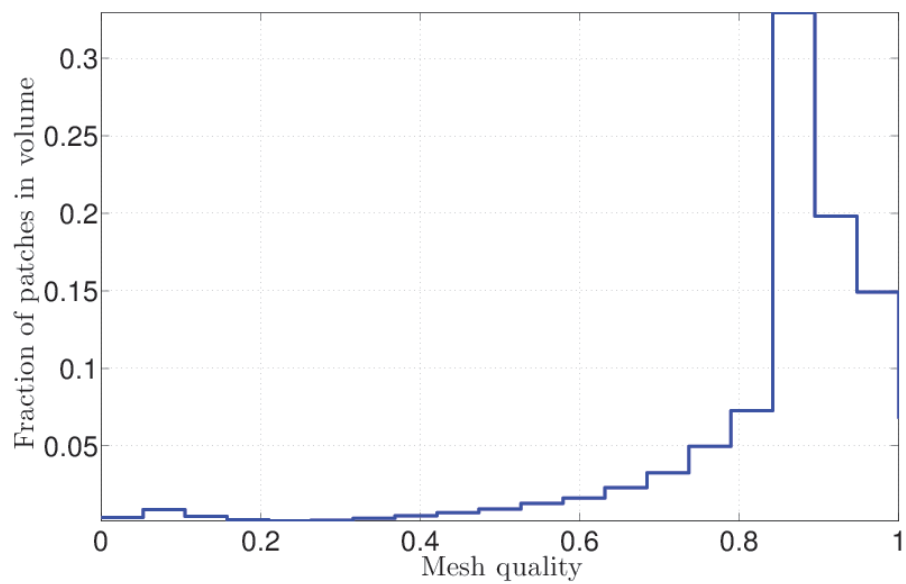
Figure 4.11: Calculated mesh quality over the entire 3-dimensional volume, in which ~ 92% of the patches have a quality above the rule-of-thumb value of 0.6 for simple finite element applications [56].

smooths each element set constraining its bordering elements to their fixed positions. This treatment gives the physically relevant higher-order topolological elements like triple lines and quad points their due consideration and r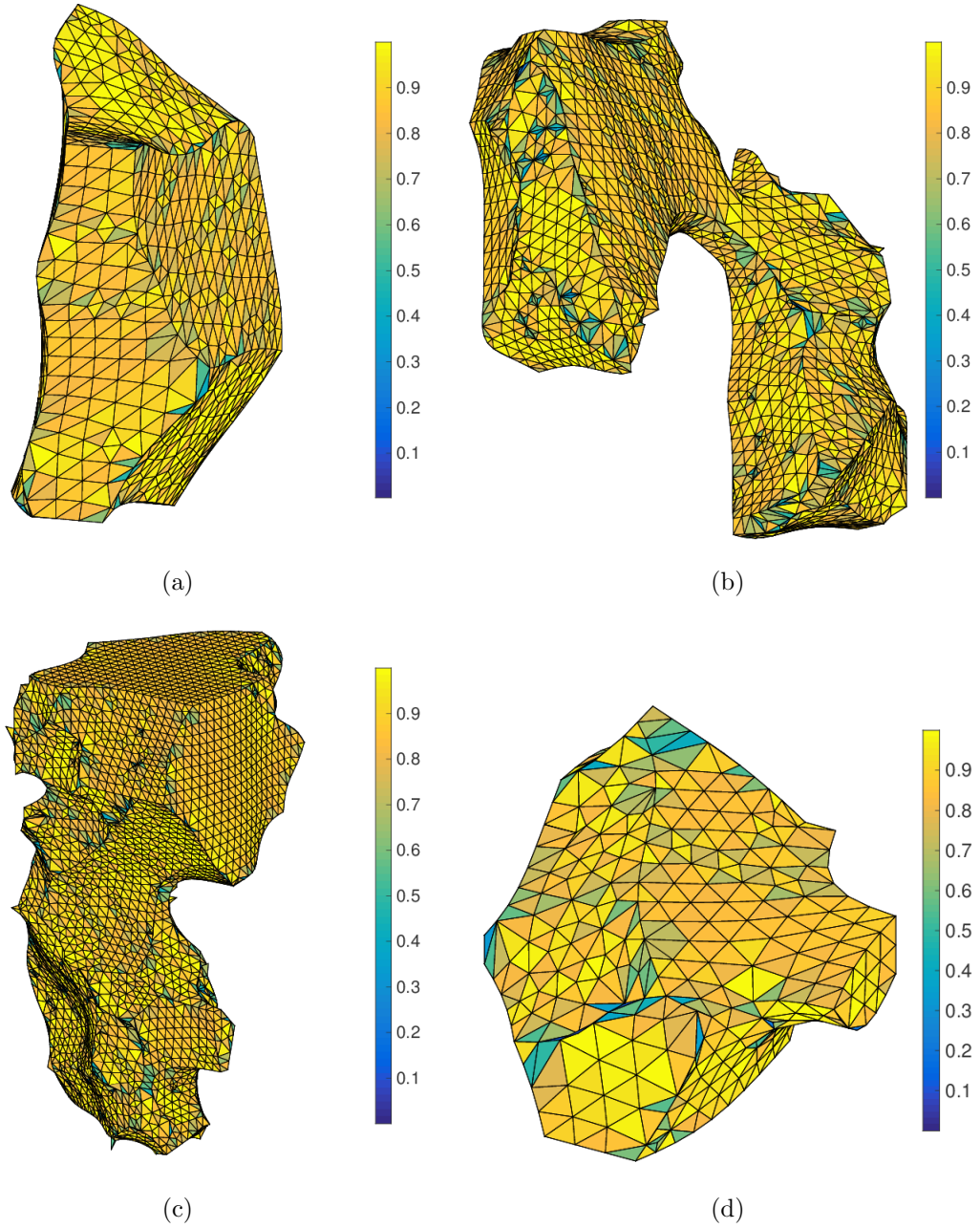etains the geometric discontinuities along a grain surface resulting from their existence. Qualitatively the smoothest curve that passes in between the original noisy sample points is chosen. Further, all elements belonging to a particular hierarchy rank in the entire volume are smoothed simultaneously so that they are ready to be used as Dirichlet boundary conditions for elements of lower rank that connect to them. The method is completely non-parametric, permitting the automated smoothing of imaged bulk structures and does not suffer from user-related effects like over-, under-smoothing or fixed-size window artifacts. Repeated applications of the smoothing on the same point set results in better smooth approximations with decreasing the extent of waviness along the smoothed surface.

The technique is predicated on the nearest neighbor connectivity of the surface nodes being known in advance, which is easily achievable by existing algorithms and is already implemented in open-source microstructure software packages [21]. The relative errors in the smoothing of known shapes are demonstrated to be a fraction of a percent for typical resolutions of microstructure imaging techniques. The estimated normals in the case of two dimensions were found to be within thresholds characteristic of bin sizes used in plots of grain boundary character distribution. The ability to handle data of different dimensions in a generalized manner allows this technique to be used for surface experiments such as optical metallography and EBSD, as well as 3D bulk techniques like nf-HEDM. Computation of the mesh quality on a 3-dimensional grain boundary network consisting of 424 grains revealed that the overwhelming majority of mesh elements have a quality above a comfortable 0.6 as required by simple applications. If need be one may remesh the output of the smoothing routine subject to junction constraints in order to obtain a more uniform meshing of the grain boundary interiors. Further, the separate treatment of the different types topological features suggests parallelizeability in order to reduce computation time.

Chapter 5

Coarsening theory and numerics

The goal of the formalism developed in this section is to solve the inverse problem of computing the dynamical parameters that mediate the migration of grain boundaries in a material sample subject to annealing, given the wealth of geometric and transport data obtainable from nondestructive imaging experiments of material microstructure. This paradigm developed for what is essentially a measurement technique is motivated by a desire to retain generality of the physics by making the fewest assumptions possible in terms of modeling the actual behavior of grain boundaries. This is, of course, complemented by the use of the requisite sophisticated computational techniques, some already established and others specifically crafted for the task at hand. A key principle of the computational analysis is its modularity in which different components may be substituted for schemes that suit specific types of input data. For example, the grid discretization of the domains of the aforementioned dynamical quantities ideally would reflect the crystal symmetry of the material being queried. We further point out that probing of the underlying physics that influence transport of grain boundaries from experimentally measured data necessarily restricts the means of data collection to non-destructive methods. In the context of modern imaging techniques, this implies synchrotron X-ray probing tools like high-energy diffraction microscopy and diffraction contrast tomography.

Also in the interests of simplicity we restrict our analysis to sets of imaged grain boundaries in the sample that have the same difference in crystal orientation across the interface. The set of grain boundaries that are analyzed at a time therefore differ only in their inclination in the crystal frame. This amounts to computing the dynamical parameters in a restricted subspace of the full grain boundary descriptor space, specifically the two-dimensional space of boundary inclinations. The experimental problem of successfully fabricating in a real material sample such a multitude of grain boundaries, and therefore a multitude of grain boundaries of one particular misorientation was achieved by trial and error and is described in **Insert section here**. More precisely, the success of this measurement depends upon the existence of

a suffucient number of grain boundaries to populate the appropriate subsection of the unit sphere S^2, which is the subdomain of interest. The exact means of determining this subdomain is described in subsection 5.5.4.

The chapter is organized as follows: A brief overview of the thermodynamic theory of grain boundaries and description of earlier models of grain boundary motion is followed by the development of a formal physical theory predicated upon the analysis of differential motion of an interface. This will give a dynamical equation that links the geometry and transport of grain boundaries to the underlying physical quantities that drive the motion. We demonstrate the consistency of the developed theory by showing its agreement with theories of grain boundary physics as described in earlier works by John von Neumann and Conyers Herring that are the basis of currently accepted capillarity theories. The rest of the chapter concerns the effective discretization of the dynamical equation and a prescription to solve it numerically for the dynamical quantities. This process in itself contains many components, each of which is described in a fair amount of detail:

1. Quantification and gridding of the domain of the unknowns of the problem, and a satisfactory interpolation and differentiation scheme therein.

2. Smoothing of gridded grain boundary surfaces and extraction of mesh elements (described in detail in Chapter 4.

3. Quantification of interface transport on a point-by-point basis.

4. Crystal symmetry-based transformations and reduction of the domain of unknowns to the smallest possible region.

5. Numerical scheme for solving the evolution equation.

5.1 Thermodynamic formulation of interface free energy

A theoretical description of a system of grain boundaries in the meso-scale from an energetics point of view requires careful justification of the applicability of equilibrium thermodynamics. The equilibrium configurations of thermodynamic systems is usually described in terms of macroscopic state variables (temperature T, pressure P, volume V, entropy S) by the minimization of the appropriate free energy of the system subject to constraints on these variables. A system of grain boundaries in thermodynamic equilibrium with its environment requires the specification of geometric constraints in addition to those on traditional thermodynamic variables. This necessitates the definition of an interface energy density γ which is an intensive thermodynamic parameter in its own right, to account for the breaking of the lattice

symmetry. We consider here only the relevant aspects of the mathematically intricate formalism of solid interfaces, including grain boundaries and interphases [57, 58, 59].

Consider a model system containing a planar interface of area A separating two bulk crystalline lattices α and β of different orientations. This system exchanges atoms from a set of M reservoirs $R_1, R_2, \ldots, R_M$. One can imagine these reservoirs to be neighboring infinite bulks of the same material. In a real polycrystal, the role of such reservoirs is played by the neighboring grains, which is appropriate at least for the analysis of infinitesimal motion of grain boundaries. In this and subsequent treatments of grain boundary systems in this text, we assume the absence of any other significant source of energy such as elastic or plastic deformation, or bulk defects other than the grain boundaries themselves. The differential in energy of the system is restated to account for the presence of the interface as:

$$dE = TdS - PdV + \sum_{i=1}^{M} \mu_i dN_i + \gamma dA \qquad (5.1)$$

where μ_i is the chemical potential corresponding to each reservoir and dN_i is the number of atoms contributed by each. In the presence of the interface, the source of the interface energy density γ is the excess of the Gibbs free energy after the addition of atoms from the reservoirs has been accounted for:

$$G = \sum_{i=1}^{M} \mu_i N_i \qquad \text{(no interface)}$$

$$\gamma = \frac{1}{A} \left[G - \sum_{i=1}^{M} \mu_i N_i \right] \qquad \text{(interface)}$$

To clarify, the bulk chemical potential for identical atomic species in identical crystallographic arrangements is the same. The definition of free energy given above is generalized to account for the cases of multiple atomic species and even different crystallographic arrangements of the same species (in materials science jargon, different phases). The definition γ pertains to a suitable region in the material around the location of the geometric interface, typically within a few atomic distances [58]. This is a significant result as it allows us to ignore atomistic details and remain in the realm of thermodynamics and geometric descriptors of grain boundaries. In Section 5.2, prototype models for grain boundaries are described.

5.2 Earlier models of interface migration

In the pre-synchrotron era, ease of generation and visualization made bubble rafts and soap film networks the prototype models of choice for studying grain boundaries [60, 61, 62]. Bubble rafts facilitated the study of defects by selective addition

and/or removal of bubbles. The study of soap films and the constrained minimum energy surfaces therein provided a continuum perspective for the study of grain boundaries. One of the earliest models for grain growth analyzes the motion of interfaces in a 2-dimensional soap froth [63] under the assumption of constant surface tension over the interfaces. It states that:

1. The velocity of the interface is proportional to the driving force which is a result of gas diffusion due to the constant pressure differential across an interface and is given by:

$$v \propto 2\gamma\kappa_m \tag{5.2}$$

where γ is the uniform surface tension over all interfaces in the network and κ_m is the mean curvature.

2. The rate of change of volume V of any one bubble in the froth is proportional to $n-6$, where n is the number of circular arcs forming the shape of the polygonal bubble. Thus, bubbles with fewer sides than six shrink and those with more sides than six grow. If n is the number of sides of the polygonal bubble, then

$$\frac{dV}{dt} =\propto \gamma\left(1 - \frac{n}{6}\right) \tag{5.3}$$

This model by John von Neumann and Mullins asserts that all interfaces migrate towards their center of curvature. Mullins later extended this principle to model the statistics of grain sizes in a coarsening 2-dimensional network [64, 65]. Mullins' principle of statistical self-similarity (SSS) states that a coarsened network of interfaces is statistically identical to its previous uncoarsened state up to a scaling of length. The SSS principle provides an estimate of the average grain size in a coarsening grain network. If the rate of change of dimension of a bubble or grain is likened to its velocity of coarsening ($v = d\langle r\rangle/dt$), then the average grain size is seen to exhibit parabolic growth as a function of time:

$$\frac{d\langle r\rangle}{dt} = 2K\frac{\gamma}{\langle r\rangle}$$
$$\implies \langle r\rangle^2 - \langle r\rangle_0^2 = 4K\gamma\left(t - t_0\right) \tag{5.4}$$

The coarsening of soap bubbles and grains both obey the principle of minimization of interface area and therefore interface energy. The driving force in both cases is the curvature-induced pressure difference on either side of an interface. However, the distinction in their actual boundary migration mechanisms is important. In the former case, coarsening takes place through the diffusion of gas molecules through the interface from one bubble into another while in the latter, boundary migration takes place through an activated process of atomic shuffling that causes the rearrangement of atoms from one crystal orientation into another and as such happens at elevated

temperatures. In fact, central to the kinematics is the grain boundary mobility μ, which by *ad hoc* introduction of an activation energy Q is believed to follow an Arrhenius-like trend with respect to temperature T:

$$\mu = \mu(T) = \mu_0 e^{-\frac{Q}{kT}} \tag{5.5}$$

The mobility appears as the proportionality constant in all relations involving the driving force of interface migration.

The von Neumann-Mullins equation (5.3) was generalized in 2007 by Macpherson and Srolovitz [66] to higher dimensions. They describe the rate of change of d-dimensional volume V_d of a 'domain' $\mathbf{D}_d$ (*i.e.* bubble or grain) that shares the set of topological elements $\mathbf{D}_{d-2}$ of dimension $d-2$ with neighboring domains:

$$\frac{dV_d}{dt} = -2\pi\mu\gamma \left(H_{d-2}(\mathbf{D}_d) - \frac{1}{6} H_{d-2}(\mathbf{D}_{d-2}) \right) \tag{5.6}$$

where H_{d-2} is the Hadwiger measure of dimension $d-2$ [67, 68]. For $d = 3$, this reduces to:

$$\frac{dV}{dt} - 2\pi\mu\gamma \left(\mathcal{L}(\mathbf{D}) - \frac{1}{6} \sum_{i=1}^{N} e_i(\mathbf{D}) \right) \tag{5.7}$$

where $\mathcal{L}(\mathbf{D})$ is the mean domain width and e_i is the length of the i-th of n triple lines shared by the domain with its neighbors.

The von Neumann-Mullins and Macpherson-Srolovitz analyses are based on the assumption of the constancy of the surface energy density γ, which we know is not the case. γ, in fact, depends on the macroscopic geometry of the domain itself, in particular the crystallographic misorientation across the interface as well as its inclination with respect to the crystal axes of the domain (as already established in Section 5.1, the definition of γ permits us to ignore atomic-scale translations). This dependence results in geometric features of the network that cannot be predicted by the von Neumann or MacPherson-Srolovitz theories, for example the unequal dihedral angles at a triple junction. This renders these earlier models inadequate to explain the behavior of grain boundaries in real polycrystalline materials. We address this dependence partially in Section 5.3, in which a generalized vector quantity is introduced that opens the door to an alternative thermodynamic treatment of interfaces, the *Hoffman-Cahn capillarity vector*.

5.3 The Hoffman-Cahn capillarity vector

A priori, not much can be done in the meso-scale to determine the functional form of the grain boundary free energy density, other than postulating that it depends

on the five grain boundary descriptor parameters at a given point. This is justified by realizing that the local free energy depends on the specific atomic arrangement in the vicinity of the region of interest, which in turn depends on the difference in orientation of the two crystal frames on either side of the interface, as well as the local inclination of the interface. Even this simple assumption, however, can lead to computationally intricate problems owing to complicated topology of this 5-parameter space. Understanding of this topology has improved over the years resulting in better descriptions of the landscape of free energy [33]. The free energy density is usually parameterized as: $\gamma = \gamma(\Delta\omega, \hat{\boldsymbol{n}})$ where $\Delta\omega$ is the 3-parameter crystal misorientation across the boundary and $\hat{\boldsymbol{n}}$ is the local boundary inclination. As mentioned earlier, we address only the variation with $\hat{\boldsymbol{n}}$ for a fixed $\Delta\omega$ for the rest of this analysis. The following theory is presented in the seminal papers by Hoffman and Cahn [69, 70].

For a simple closed surface defined in terms of spherical polar coordinates $f(r, \theta, \phi) = 0$ and whose centroid is at the origin of a fixed coordinate frame, the capillarity vector is defined as $\xi \equiv \nabla(r\gamma)$. Knowledge of the gradient in spherical polar coordinates gives us:

$$\nabla \equiv \hat{\boldsymbol{r}}\frac{\partial}{\partial r} + \frac{1}{r}\underbrace{\left(\hat{\boldsymbol{\theta}}\frac{\partial}{\partial\theta} + \hat{\boldsymbol{\phi}}\frac{1}{sin\theta}\frac{\partial}{\partial\phi}\right)}_{\equiv\partial/\partial\hat{\boldsymbol{n}}}$$

$$\xi = \nabla(r\gamma) = \gamma\hat{\boldsymbol{n}} + \frac{\partial\gamma}{\partial\hat{\boldsymbol{n}}}$$

$$\xi(\hat{\boldsymbol{n}}) = \gamma\hat{\boldsymbol{n}} + \nabla_{\hat{\boldsymbol{n}}}\gamma \tag{5.8}$$

where $\hat{\boldsymbol{r}}$ and $\hat{\boldsymbol{n}}$ are used interchangeably and $\partial/\partial\hat{\boldsymbol{n}}$ is the gradient operator on the unit sphere S^2, with the origin being the local center of curvature. It is self-evident that $\gamma = \gamma(\hat{\boldsymbol{n}}) \Rightarrow \xi = \xi(\hat{\boldsymbol{n}})$. Hoffman and Cahn's analysis [69, 70] goes on to describe how this *vector* quantity behaves like a thermodynamic free energy and mediates the distortion of grain boundaries, bulk changes and torsion inclusive, all in an attempt to attain the minimum energy configuration. In particular, an isotropic free energy ($\gamma = \gamma_0$) would result in ξ being locally normal to an interface at all points ($\xi = \gamma_0\hat{\boldsymbol{n}}$) since $\nabla_{\hat{\boldsymbol{n}}}\gamma = 0$ and the only energy minimization mechanism is reduction of area through radial shrinking (i.e. the grain boundary shrinks in the direction of its local center of curvature). If nonzero, the gradient term $\nabla_{\hat{\boldsymbol{n}}}\gamma$ in the capillarity vector mediates the rotation of the surface in order to reorient it into a lower energy configuration. The form of the capillarity vector in Equation (5.8) naturally appears in the variational analysis of grain boundary migration energetics (described in Section 5.4). An appropriate numerical discretization scheme for ξ is critical to the eventual goal of computing grain boundary energy and is the focus of Section 5.5.3.

For high-angle grain boundaries, a minimum of energy is usually known from simulations to be a cusp in one or more parameters [71, 72, 73] and as such the gradient $\nabla_{\hat{n}}\gamma$ does not have a unique value at these points. The formalism presented here ignores this in an attempt to resolve this minimum to experimental resolution.

5.4 Interface dynamics from variational principles

Given here is a variational treatment of grain boundary migration energetics and dynamics. Eventual goals of measuring relevant physical quantities with the computational tools described in earlier sections are set forth. First a few identities involving integrals of scalar and vector fields over moving surfaces are stated and proved (not rigorously), which will form the basis of the subsequent analysis.

5.4.1 Important identities

Consider an open surface Γ, whose boundary is $\partial\Gamma$.

1. Consider a scalar field Φ on Γ. The following identity holds:

$$\boxed{\int_\Gamma dS \ \nabla_\Gamma\Phi = 2\int_\Gamma dS \ \hat{\boldsymbol{n}}\kappa\Phi + \int_{\partial\Gamma} dS' \ \hat{\boldsymbol{m}}\Phi}$$ (5.9)

where $\hat{\boldsymbol{n}}$ is the unit normal, κ is the mean curvature and $\hat{\boldsymbol{m}}$ is the binormal to the surface perimeter: $\hat{\boldsymbol{m}} = \hat{\boldsymbol{t}} \times \hat{\boldsymbol{n}}$, where $\hat{\boldsymbol{t}}$ is the counterclockwise unit tangent to the perimeter. dS is an area element of Γ and dS' is an line element of $\partial\Gamma$.

Proof. Let s_1 and s_2 be the arc lengths on the surface along two orthogonal directions. Unit vectors $\hat{\boldsymbol{s_1}}$ and $\hat{\boldsymbol{s_2}}$ in these directions form a basis of the local tangent space.

$$\int_\Gamma dS \ \nabla_\Gamma\Phi = \int_\Gamma dS \ \left[\frac{\partial\left(\Phi\hat{\boldsymbol{s_1}}\right)}{\partial s_1} + \frac{\partial\left(\Phi\hat{\boldsymbol{s_2}}\right)}{\partial s_2}\right]$$
$$= \int_\Gamma dS \ \left[\left(\frac{\partial\Phi}{\partial s_1}\hat{\boldsymbol{s_1}} + \frac{\partial\Phi}{\partial s_2}\hat{\boldsymbol{s_2}}\right) + \Phi\left(\frac{\partial\hat{\boldsymbol{s_1}}}{\partial s_1} + \frac{\partial\hat{\boldsymbol{s_2}}}{\partial s_2}\right)\right]$$

The terms in the first parenthesis, when integrated over the surface are seen to go to zero everywhere except at the boundary since they are of the form: $\ldots + \left(\Phi^{(n)} - \Phi^{(n-1)}\right) + \left(\Phi^{(n+1)} - \Phi^{(n)}\right) + \ldots$ along both the directions $\hat{\boldsymbol{s_1}}$ and $\hat{\boldsymbol{s_2}}$. This ensures that only the boundary contributes and results in boundary term in Equation (5.9). Next, the Serret-Frenet formulas [74, 75] are applied to

the second parenthesis to get:

$$\frac{\partial \hat{\boldsymbol{s_1}}}{\partial s_1} = \kappa_1 \hat{\boldsymbol{n}}$$

$$\frac{\partial \hat{\boldsymbol{s_2}}}{\partial s_2} = \kappa_2 \hat{\boldsymbol{n}}$$

thereby obtaining the final proof in terms of the mean curvature: $\kappa = (\kappa_1 + \kappa_2)/2$.

$\square$

2. Consider a vector field $\boldsymbol{U}$ on the surface Γ. The following identity holds, with $\nabla_\Gamma \cdot (\bullet)$ being the divergence operator on the surface Γ:

$$\boxed{\int_\Gamma dS \; \nabla_\Gamma \cdot \boldsymbol{U} = 2 \int_\Gamma dS \; \kappa \boldsymbol{U} \cdot \hat{\boldsymbol{n}} + \int_{\partial\Gamma} dS' \; \boldsymbol{U} \cdot \hat{\boldsymbol{m}}} \qquad (5.10)$$

Proof. Proceeding in the same manner as the previous proof,

$$\int_\Gamma dS \; \nabla_\Gamma \cdot \boldsymbol{U} = \int_\Gamma dS \; \left[\frac{\partial (\boldsymbol{U} \cdot \hat{\boldsymbol{s_1}})}{\partial s_1} + \frac{\partial (\boldsymbol{U} \cdot \hat{\boldsymbol{s_2}})}{\partial s_2} \right]$$

$$= \int_\Gamma dS \; \left[\underbrace{\left(\frac{\partial \boldsymbol{U}}{\partial s_1} \cdot \hat{\boldsymbol{s_1}} + \frac{\partial \boldsymbol{U}}{\partial s_2} \cdot \hat{\boldsymbol{s_2}} \right)}_{boundary\; contribution\; only} + \underbrace{(\kappa_1 + \kappa_2)\, \hat{\boldsymbol{n}}}_{Serret-Frenet} \cdot \boldsymbol{U} \right]$$

$$= \int_{\partial\Gamma} dS' \; \hat{\boldsymbol{m}} \cdot \boldsymbol{U} + 2 \int_\Gamma dS \; \kappa \hat{\boldsymbol{n}} \cdot \boldsymbol{U} \qquad (\because \kappa = \tfrac{\kappa_1 + \kappa_2}{2})$$

$\square$

3. For a scalar field Φ and a vector field $\boldsymbol{U}$ on a surface Γ, the following identity holds:

$$\boxed{\int_\Gamma dS \; (\Phi \nabla_\Gamma \cdot \boldsymbol{U} + \nabla_\Gamma \Phi \cdot \boldsymbol{U}) = 2 \int_\Gamma dS \; \kappa \hat{\boldsymbol{n}} \cdot \boldsymbol{U} \Phi + \int_{\partial\Gamma} dS' \; \hat{\boldsymbol{m}} \cdot \boldsymbol{U} \Phi} \quad (5.11)$$

where $\nabla_\Gamma (\bullet)$ is the gradient operator on the surface Γ.

Proof.

$$\int_\Gamma dS \; (\Phi \nabla_\Gamma \cdot \boldsymbol{U} + \nabla_\Gamma \Phi \cdot \boldsymbol{U})$$

$$= \int_\Gamma dS \; \nabla_\Gamma \cdot (\Phi \boldsymbol{U})$$

$$= 2 \int_\Gamma dS \; \kappa \hat{\boldsymbol{n}} \cdot \boldsymbol{U} \Phi + \int_{\partial\Gamma} dS' \; \hat{\boldsymbol{m}} \cdot \boldsymbol{U} \Phi$$

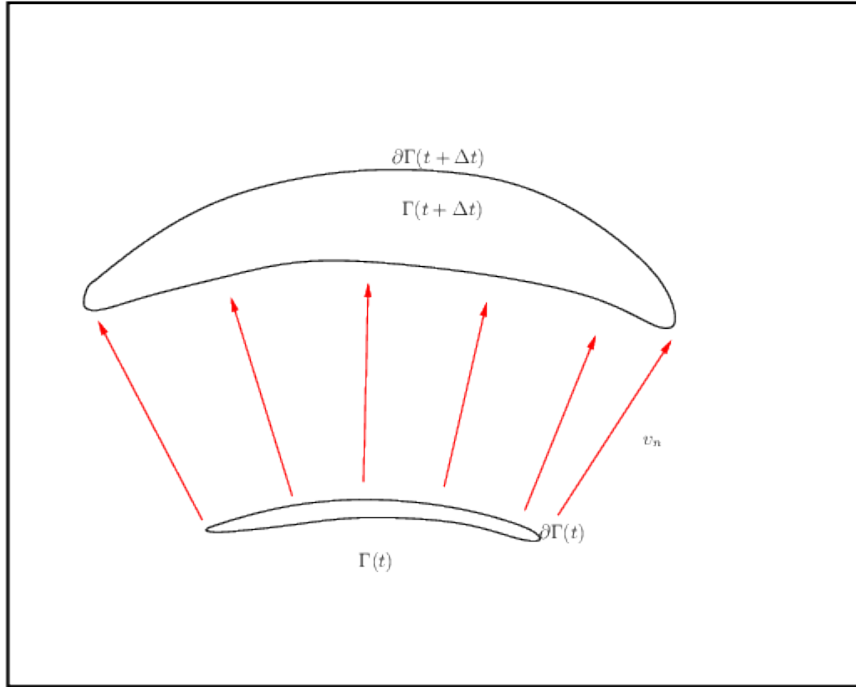(Applying Equation (5.10) to the vector field $\Phi \boldsymbol{U}$)

$\square$

Figure 5.1: Migration of a surface Γ in time Δt by way of local normal velocity v_n, which is a scalar field on Γ (*i.e.* $\boldsymbol{v} \cdot \hat{\boldsymbol{n}}$).

Note that in each of these identities, if the surface is flat ($\kappa = 0$) then only the boundary contributes to the surface integral.

5.4.2 Energetics of boundary migration

In the following analysis an open 3D surface $\Gamma(t)$ at time instant t, whose perimeter is $\partial\Gamma(t)$, is considered as a model for a grain boundary. The boundary energy associated with this surface is a scalar field γ with units of energy per unit area. Of course, in a real grain boundary, this excess energy per unit grain boundary area is a result of the breaking of the translational symmetry of the lattice in a direction normal to the interface. The departure from regular crystal structure at the grain boundary implies that some atoms are removed from their respective local minima in the energy landscape and pushed to higher energy levels.

At a temperature T, let the boundary migrate to a new position $\Gamma(t + \Delta t)$ with a local normal velocity v_n, as shown in Figure 5.1. The rate of change of the surface

energy E is:

$$\frac{dE}{dt} = \frac{d}{dt} \int_{\Gamma} dS \, \gamma(\hat{\boldsymbol{n}})$$

$$= \lim_{\Delta t \to 0} \frac{1}{\Delta t} \left[\int_{\Gamma(t+\Delta t)} dS \, \gamma \left(\hat{\boldsymbol{n}}(t+\Delta t) \right) - \int_{\Gamma(t)} dS \, \gamma(\hat{\boldsymbol{n}}) \right] + \int_{\partial\Gamma(t)} dS' \, \gamma(\hat{\boldsymbol{n}}) \boldsymbol{v} \cdot \hat{\boldsymbol{m}}$$

$$(5.12)$$

The integral over $\partial\Gamma$ results from the time dependence of the migrating surface Γ. The following first-order substitutions are now made:

- $\boxed{\hat{\boldsymbol{n}}(t+\Delta t) \simeq \hat{\boldsymbol{n}}(t) + \frac{d\hat{\boldsymbol{n}}}{dt}\Delta t = \hat{\boldsymbol{n}} - (\nabla_{\Gamma} v_n)\,\Delta t}$, which follows from:

$$\frac{d\hat{\boldsymbol{n}}}{dt} + \nabla_{\Gamma} v_n = 0$$

  where ∇_{Γ} is the 2-dimensional gradient operator on the surface and $v_n \equiv \boldsymbol{v} \cdot \hat{\boldsymbol{n}}$ is the local normal velocity.

- $\boxed{dS(t+\Delta t) \simeq [1 + 2\kappa_m v_n \Delta t]\, dS(t)}$. This is justified by considering a spherical surface of radius R expanding radially to a radius $R + dR$ in time Δt while maintaining the solid angle Ω subtended at the spherical center. The area A_{new} of the new patch is calculated as: $A_{new} = \Omega(R + dR)^2 = \Omega R^2(1 + dR/R)^2 \simeq A_{old}(1 + 2\kappa v_n \Delta t)$. Here the curvature is inversely related to the spherical radius. In case of a general surface, a local ellipsoidal approximation can be made to first order. Therefore the surface has two local principal radii R_1 and R_2. The replacement $\frac{1}{R} \to \frac{1}{2}\left(\frac{1}{R_1} + \frac{1}{R_2}\right) \equiv \kappa_m$ is made. Further, $dR = v_n \Delta t$ is self-explanatory, and the required result is obtained.

With these substitutions, Equation 5.12 becomes:

$$\frac{dE}{dt} = \lim_{\Delta t \to 0} \frac{1}{\Delta t} \int_{\Gamma(t)} dS \, \left[(1 + 2\kappa_m v_n \Delta t)\left(\gamma(\hat{\boldsymbol{n}}) - \nabla_{\hat{\boldsymbol{n}}}\gamma \cdot \nabla_{\Gamma} v_n \Delta t \right) - \gamma(\hat{\boldsymbol{n}}) \right] + \int_{\partial\Gamma(t)} dS' \, \gamma\boldsymbol{v} \cdot \hat{\boldsymbol{m}}$$

$$= \int_{\Gamma} dS \, \left(2\kappa_m v_n \gamma - \nabla_{\hat{\boldsymbol{n}}}\gamma \cdot \nabla_{\Gamma} v_n \right) + \int_{\partial\Gamma} dS' \, \gamma\boldsymbol{v} \cdot \hat{\boldsymbol{m}} \qquad (5.13)$$

Finally Equation 5.11 is applied to the $\nabla_{\hat{\boldsymbol{n}}}\gamma \cdot \nabla_{\Gamma} v_n$ term above, with $\Phi \equiv v_n$ and $\boldsymbol{U} \equiv \nabla_{\hat{\boldsymbol{n}}}\gamma$ and it is noted that $\hat{\boldsymbol{n}} \cdot \nabla\gamma = 0$ because $\nabla\gamma$ lies in the local tangent plane and hence:

$$\frac{dE}{dt} = \int_{\Gamma} dS \, v_n \left[\nabla_{\Gamma} \cdot \nabla\gamma + 2\kappa_m\gamma \right] + \int_{\partial\Gamma} dS' \, \boldsymbol{v} \cdot \left[\gamma\hat{\boldsymbol{m}} - (\nabla\gamma \cdot \hat{\boldsymbol{m}})\,\hat{\boldsymbol{n}} \right]$$

$$= \boxed{\int_{\Gamma} dS \, v_n \nabla_{\Gamma} \cdot \left[\nabla\gamma + \gamma\hat{\boldsymbol{n}} \right] + \oint_{\partial\Gamma} dS' \, \boldsymbol{v} \cdot \left[\gamma\hat{\boldsymbol{m}} - (\nabla\gamma \cdot \hat{\boldsymbol{m}})\,\hat{\boldsymbol{n}} \right]} \qquad (5.14)$$

75

This is the generalized expression for the rate of change of excess energy of a moving surface. The divergence term $\nabla_\Gamma \cdot [\nabla\gamma + \gamma\hat{\boldsymbol{n}}]$ in the first integral is analogous to the pressure difference across a membrane through which diffusion is taking place. The second term describes the dynamics of the one-dimensional perimeter $\partial\Gamma$ under a line tension $\gamma\hat{\boldsymbol{m}} + (\nabla\gamma \cdot \hat{\boldsymbol{m}})\,\hat{\boldsymbol{n}}$. The fact that the variation of the unit normal over the surface is nothing but the curvature $(\nabla_\Gamma \cdot \hat{\boldsymbol{n}} = 2\kappa_m)$ has been exploited here. The expression neatly accounts for contributions from the interior as well as the boundary of the surface. It is noted that its applicability ranges from grain boundary dynamics to those of soap bubble systems, which were historically prototypes for models of grain boundary networks. Also noted is the natural appearance of the capillarity vector $\boldsymbol{\xi} \equiv \nabla\gamma + \gamma\hat{\boldsymbol{n}}$, as detailed by Hoffman and Cahn [69, 70]. The treatment here is similar to the one by Kinderlehrer [76].

5.4.3 Boundary migration as an optimality condition

Having derived the equation (5.14) for the rate of change of surface energy, we postulate that the migration follows an optimal energetic path i.e. the migration ensures that the energy of the surface reaches a minimum at an optimal rate. This is presently shown to be consistent with the existing assumption of grain boundary velocity being proportional to the difference in local 'pressure' across the boundary.

Both integrals in Equation (5.14) are of the following form over a domain Ω:

$$F[v(x)] = \int_\Omega d\Omega\; v(\boldsymbol{x})f(\boldsymbol{x}) \tag{5.15}$$

where $\boldsymbol{x} \in \Omega$. For a non-trivial optimal value of the *linear* functional $F[v]$, the $v(\boldsymbol{x})$ are constrained to be normalized by some weight, which is rather pointedly chosen as $1/2\mu$. Thus, assuming $\int_\Omega d\Omega \frac{v^2}{2\mu} = 1$ and choosing λ as a Lagrange multiplier,

$$\delta \int_\Omega d\Omega \left[vf + \lambda\frac{v^2}{2\mu} \right] = 0$$
$$\Rightarrow v \sim -\mu f \tag{5.16}$$

Applying this to the two integral terms in Equation (5.14), what remains is the following expressions for the velocity of the surface:

$$v_n = -\mu\nabla_\Gamma \cdot [\nabla\gamma + \gamma\hat{\boldsymbol{n}}] \tag{5.17}$$
$$\boldsymbol{v} = -\mu_{TL}\left[\gamma\hat{\boldsymbol{m}} + (\nabla\gamma \cdot \hat{\boldsymbol{m}})\,\hat{\boldsymbol{n}}\right] \tag{5.18}$$

In Equation (5.17), $\nabla_\Gamma \cdot [\nabla\gamma + \gamma\hat{\boldsymbol{n}}]$ is the driving force per unit area of the surface and is proportional to the normal velocity. The constant of proportionality μ is the *mobility* of the surface and in general is a scalar field on it. Similarly, μ_{TL} can be

interpreted as the mobility of the perimeter. The normalization condition of the surface velocity decides the physical unit of the mobility without loss of generality. While while this equation gives the appearance of diffusive behavior (in which the velocity is proportional to the excess pressure across the interface), there is in fact no real diffusion taking place in the sense that the density of the material on either side of the interface is the same. The boundary migrates through atomic rearrangement from one crystal orientation into another.

In a real grain boundary network, a single triple line is shared between 3 grain boundaries. In this case, the velocity of the triple line becomes: $\boldsymbol{v} = -\mu_{TL} \sum_{i=1}^{3} \left[\gamma_i \hat{\boldsymbol{m}}_i + (\nabla\gamma_i \cdot \hat{\boldsymbol{m}}_i) \hat{\boldsymbol{n}} \right]$. In equilibrium, we have

$$\sum_{i=1}^{3} \left[\gamma_i \hat{\boldsymbol{m}}_i + (\nabla\gamma_i \cdot \hat{\boldsymbol{m}}_i) \hat{\boldsymbol{n}}_i \right] = 0 \tag{5.19}$$

This is the generalized version of the *Herring formula* [77], which become Young's equations in the case of isotropic energies ($\nabla\gamma_i = 0$) and alludes to the balance of forces along a junction of grain boundaries.

Of particular significance is the fact that the diffusion-like behavior and the geometry of balanced forces as detailed by Herring's equations is a consequence of mathematical normalization and the very basic physical requirement that the system moves along the energy landscape in a steepest-descent direction. In the light of this optimality-induced development, the dynamical equation (5.14) now becomes:

$$\boxed{\frac{dE}{dt} = -\int_{\Gamma} dS \, \frac{v_n^2}{\mu} + \oint_{\partial\Gamma} dS' \, \boldsymbol{v} \cdot [\gamma\hat{\boldsymbol{m}} - (\nabla\gamma \cdot \hat{\boldsymbol{m}}) \hat{\boldsymbol{n}}]} \tag{5.20}$$

Equation (5.20) links the dynamical quantities γ and μ that mediate the migration of a boundary to its geometry and transport *i.e.* Γ and $\boldsymbol{v}$. The integral over the closed path $\partial\Gamma$ is not subjected to a similar optimality-based simplification because of the difficulty of interpreting physically a mobility term for the junctions of two or more interfaces. At these locations atoms rearrange themselves in a manner that is difficult to model satisfactorily. The following sections describe a numerical scheme to discretize and solve this equation for the dynamical quantities.

5.5 Numerics

5.5.1 Discretization of the dynamical equation

In order to satisfactorily discretize the evolution equation (5.20), we repeat its derivation for a discretized surface. We assume the presence of a sufficiently high-resolution Delaunay mesh on the surface consisting of the set of triangulations $\mathbb{T}$. We

first attempt to derive an expression for the migration of the nodes of the triangulation. If each triangle is described by its plane unit normal $\hat{\boldsymbol{n}}_i$ and area A_i, then the instantaneous energy of the surface is given by:

$$E = \sum_{i \in \mathbb{T}} \gamma(\hat{\boldsymbol{n}}_i) A_i \quad , \tag{5.21}$$

whose rate of change is:

$$\frac{dE}{dt} = \sum_{i \in \mathbb{T}} \nabla\gamma_i \cdot \frac{d\hat{\boldsymbol{n}}_i}{dt} A_i + \gamma_i \frac{dA_i}{dt}$$

$$= \sum_{i \in \mathbb{T}} \nabla\gamma_i \cdot \left[\frac{d}{dt}(A_i\hat{\boldsymbol{n}}_i) - \frac{dA_i}{dt}\hat{\boldsymbol{n}}_i \right] + \gamma_i (\hat{\boldsymbol{n}}_i \cdot \hat{\boldsymbol{n}}_i) \frac{dA_i}{dt}$$

$$= \sum_{i \in \mathbb{T}} \nabla\gamma_i \cdot \frac{d}{dt}(A_i\hat{\boldsymbol{n}}_i) + \gamma_i \hat{\boldsymbol{n}}_i \cdot \left[\frac{d}{dt}(A_i\hat{\boldsymbol{n}}_i) - A_i \frac{d\hat{\boldsymbol{n}}_i}{dt} \right] \qquad (\because \nabla\gamma_i \cdot \hat{\boldsymbol{n}}_i = 0)$$

$$= \sum_{i \in \mathbb{T}} \underbrace{[\gamma_i \hat{\boldsymbol{n}}_i + \nabla\gamma_i]}_{\boldsymbol{\xi}_i} \cdot \frac{d}{dt}(A_i\hat{\boldsymbol{n}}_i) \qquad (\because \hat{\boldsymbol{n}}_i \cdot \frac{d\hat{\boldsymbol{n}}_i}{dt} = 0)$$

The natural appearance of Hoffman and Cahn's capillarity vector $\boldsymbol{\xi}_i = \boldsymbol{\xi}(\hat{\boldsymbol{n}}_i)$ is again noted. Further, the symmetric expression for the vector area $A_i\hat{\boldsymbol{n}}_i$ in terms of the nodes $\{\boldsymbol{x}_\mu^{(i)}, \boldsymbol{x}_\nu^{(i)}, \boldsymbol{x}_\rho^{(i)}\}$ of the triangular element i (taken in right handed order) is given by:

$$A_i\hat{\boldsymbol{n}}_i = \frac{1}{2} \left[\boldsymbol{x}_\mu^{(i)} \times \boldsymbol{x}_\nu^{(i)} + \boldsymbol{x}_\nu^{(i)} \times \boldsymbol{x}_\rho^{(i)} + \boldsymbol{x}_\rho^{(i)} \times \boldsymbol{x}_\mu^{(i)} \right]$$

$$\implies \frac{d}{dt}(A_i\hat{\boldsymbol{n}}_i) = \frac{1}{2} \left[\frac{d\boldsymbol{x}_\mu^{(i)}}{dt} \times \left(\boldsymbol{x}_\nu^{(i)} - \boldsymbol{x}_\rho^{(i)} \right) + \frac{d\boldsymbol{x}_\nu^{(i)}}{dt} \times \left(\boldsymbol{x}_\rho^{(i)} - \boldsymbol{x}_\mu^{(i)} \right) + \frac{d\boldsymbol{x}_\rho^{(i)}}{dt} \times \left(\boldsymbol{x}_\mu^{(i)} - \boldsymbol{x}_\nu^{(i)} \right) \right]$$

The expression for the rate of energy change, therefore, is:

$$\frac{dE}{dt} = \frac{1}{2} \sum_{i \in \mathbb{T}} \sum_{\mu \in i} \boldsymbol{\xi}_i \cdot \left[\frac{d\boldsymbol{x}_\mu^{(i)}}{dt} \times \left(\boldsymbol{x}_\nu^{(i)} - \boldsymbol{x}_\rho^{(i)} \right) \right]$$

$$= \frac{1}{2} \sum_{i \in \mathbb{T}} \sum_{\mu \in i} \frac{d\boldsymbol{x}_\mu^{(i)}}{dt} \cdot \left[\left(\boldsymbol{x}_\nu^{(i)} - \boldsymbol{x}_\rho^{(i)} \right) \times \boldsymbol{\xi}_i \right] \tag{5.22}$$

The last result was obtained using the cyclic property of the scalar triple product. In the inner summation over μ it is to be understood that for every $\mu \in i$, ν and ρ denote the *next two nodes, taken in right-handed cyclic order*.

We see again that the terms in Equation (5.22) are of the form $\boldsymbol{v}_\mu \cdot \boldsymbol{F}_\mu$ where $\boldsymbol{v}_\mu$ is the node velocity and $\boldsymbol{F}_\mu$ is some vector field. As before, we require for non-triviality that this rate of change is optimal subject to a normalization constraint on the set of $\boldsymbol{v}_\mu$.

For completeness, we recall the normalization constraint described in the continuous case:

$$\int_\Gamma dS \; \frac{v_n^2}{2M} = K$$

where M is the mobility. In the same spirit, we formulate the constraint in the case of this discrete mesh:

$$\sum_{\text{All nodes}} \alpha_\mu \frac{v_\mu^2}{2M_\mu} = K$$

A few highly significant points regarding this constraint:

- We require the the values of mobility M_μ at the nodes μ even though it is *a priori* a function of $\hat{\boldsymbol{n}}_i$. We estimate the mobility at the node μ in terms of the set $\mathbb{U}(\mu)$ of the triangular surface elements that share it ($\mathbb{U}(\mu) \in \mathbb{T}$):

$$M_\mu = \frac{\sum_{j \in \mathbb{U}(\mu)} A_j M(\hat{\boldsymbol{n}}_j)}{\sum_{j \in \mathbb{U}(\mu)} A_j}$$

- α_μ is the area associated with the node μ and is not to be confused with the area of the triangular elements A_i defined previously. We estimate:

$$\alpha_\mu = \frac{1}{3} \sum_{j \in \mathbb{U}(\mu)} A_j$$

This ensures that the total surface area is conserved: $\sum_\mu \alpha_\mu = \sum_i A_i$. With these definitions, we seek to solve the variational problem with Lagrange multiplier λ:

$$\delta \left[\frac{1}{2} \sum_{i \in \mathbb{T}} \sum_{\mu \in i} \frac{d\boldsymbol{x}_\mu^{(i)}}{dt} \cdot \left(\boldsymbol{x}_\nu^{(i)} - \boldsymbol{x}_\rho^{(i)} \right) \times \boldsymbol{\xi}_i + \lambda \sum_\mu \frac{\alpha_\mu}{2M_\mu} \left| \frac{d\boldsymbol{x}_\mu}{dt} \right|^2 \right] = 0 \qquad (5.23)$$

$$\lambda = \left[\frac{1}{8K} \sum_\mu \frac{M_\mu}{\alpha_\mu} \left| \sum_{i \ni \mu} \left(\boldsymbol{x}_\nu^{(i)} - \boldsymbol{x}_\rho^{(i)} \right) \times \boldsymbol{\xi}_i \right|^2 \right]^{1/2} \qquad (5.24)$$

where the variation is taken over the Cartesian components of $d\boldsymbol{x}_\mu/dt$ and the Lagrange multiplier is evaluated from the normalization condition. The resultant dynamic equation is (with a convenient choice of K):

$$\boxed{ \frac{d\boldsymbol{x}_\mu}{dt} = -\frac{M_\mu}{\alpha_\mu} \sum_{j \in \mathbb{U}(\mu)} \left(\boldsymbol{x}_\nu^{(j)} - \boldsymbol{x}_\rho^{(j)} \right) \times \boldsymbol{\xi}_j } \qquad (5.25)$$

where the indices $\{\mu, \nu, \rho\}$ maintain their right-handed cyclic order. This formulation ensures in addition that the discretization scheme is independent of mesh size. We
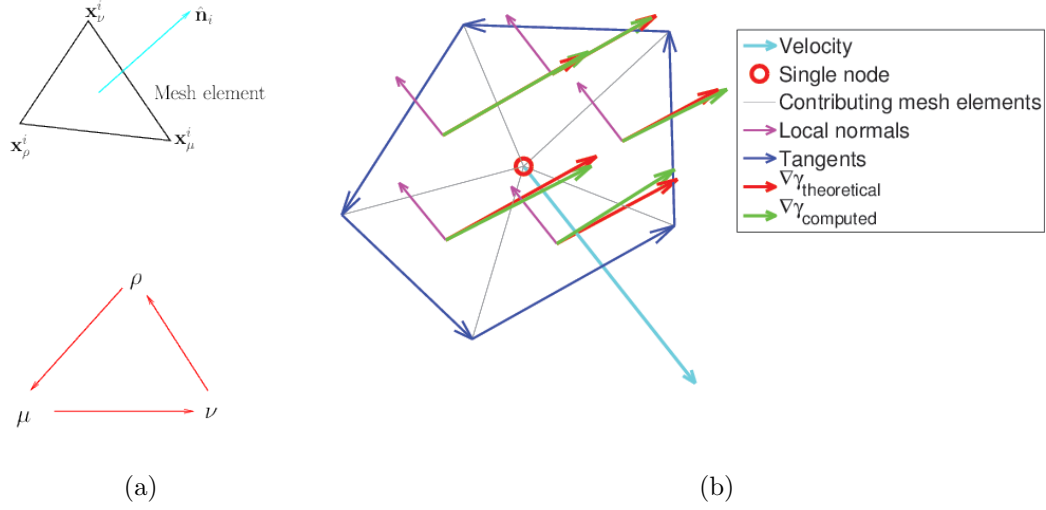
Figure 5.2: **(a)** Right-handed cyclic notation for mesh element nodes, **(b)** Pictorial relation between node velocity $\frac{d\boldsymbol{x}_\mu}{dt}$ (cyan) to local mesh geometry, in particular $\hat{\boldsymbol{n}}_i$ (magenta), $\boldsymbol{x}_\nu^{(j)} - \boldsymbol{x}_\rho^{(j)}$ (blue) and local field gradient $\nabla\gamma$ (red, green).

note that Equation (5.25) provides a prescription for evolving closed surfaces if the free energy density and mobility are known in advance. This is precisely what we apply to evolve a spherical surface under known energy and mobility as a proof of concept. A visual representation of Equation (5.25) which links node migration to the relevant mesh elements is shown in Figure 5.2.

In order to make dynamic equation (5.22) look like the original equation (5.20), we define the set I of mesh nodes interior to the surface Γ, and the set P of perimeter nodes of Γ. This results in:

$$\frac{d}{dt}\sum_{i\in I\cup P}\gamma(\hat{\boldsymbol{n}}_i)\Delta S_i = \left[\sum_{\mu\in I}+\sum_{\mu\in P}\right]\left\{\frac{d\boldsymbol{x}_\mu}{dt}\cdot\sum_{j\in\mathbb{U}(\mu)}\left(\boldsymbol{x}_\nu^{(j)}-\boldsymbol{x}_\rho^{(j)}\right)\times\boldsymbol{\xi}_j\right\}$$

$$\boxed{\frac{1}{\Delta t}\left(\sum_{\Gamma_2}\Delta S_i\gamma_i-\sum_{\Gamma_1}\Delta S_i\gamma_i\right) = -\sum_{\mu\in I}\frac{\alpha_\mu}{M_\mu}\left|\frac{d\boldsymbol{x}_\mu}{dt}\right|^2+\sum_{\mu\in P}\frac{d\boldsymbol{x}_\mu}{dt}\cdot\left\{\sum_{j\in\mathbb{U}(\mu)}\left(\boldsymbol{x}_\nu^{(j)}-\boldsymbol{x}_\rho^{(j)}\right)\times\boldsymbol{\xi}_j\right\}}$$

$$(5.26)$$

As in the original equation (5.20), the sum over I results from the steepest descent condition, and the sum over P is the force balance term described by Herring [77]. The usefulness of Equation (5.26) hinges on a reliable estimate of $\boldsymbol{\xi}_j$ on the given mesh, which in turn depends on an estimate of $\nabla\gamma_j$.

We note that Equation (5.26) is the discrete version of the original evolution equation (5.20), customized to a surface mesh, which is the representation of choice for imaged microstructure data. As before the perimeter term is left in its original form. This equation expresses the rate of energy change in terms of a sum over the internal nodes and external mesh elements.

We now make a crucial interpretation of Equation (5.26) that leads to a way of solving for the unknowns γ_μ and $\chi_\mu \equiv 1/M_\mu$, which correspond to the continuous free energy density $\gamma(\hat{\boldsymbol{n}})$ and inverse mobility $\chi(\hat{\boldsymbol{n}}) \equiv 1/\mu(\hat{\boldsymbol{n}})$ respectively, which are precisely the dynamical quantities we set out to seek in the first place. In other words, we seek discrete approximations to the scalar fields that are γ and $1/\mu$. We imagine the domain of γ_μ and χ_μ, which is an appropriately symmetry-reduced subset of the unit sphere S^2, to be sampled by N points $\{\hat{\boldsymbol{n}}_1,\ \hat{\boldsymbol{n}}_2,\ \dots \hat{\boldsymbol{n}}_N\}$ as uniformly as we can manage. The scalar fields are therefore expressed by the single $2N$-tupled column vector $\mathbf{x} = [\gamma_1\ \gamma_2\ \dots\ \gamma_N\ \chi_1\ \chi_2 \dots\ \chi_N]^T$. Clearly, the higher the value of N, the better sampled the domain is but the more the number of unknowns to solve for. We notice from Equation (5.26) that if a satisfactory linearization of the capillarity vector $\boldsymbol{\xi}_i$ (which contains a derivative term $\nabla\gamma$) were available (we assert that a very elegant linearization can be derived) then the evolution dynamics of the entire surface in question can be expressed *linearly* in the unknowns γ_i and χ_i. The coefficients of this linear, homogeneous equation are noted to be derived from boundary geometry (area ΔS_i of the triangular elements, area α_μ associated with the nodes, line elements $\boldsymbol{x}_\nu^{(j)} - \boldsymbol{x}_\rho^{(j)}$ along the perimeter of the boundary) and boundary transport (node velocity $\partial\boldsymbol{x}_\mu/dt$), all of which are, very happily for us, directly measurable from experimental data.

If we consider a set of N_b grain boundaries, all of the same effective misorientation and differing only in the boundary inclination $\hat{\boldsymbol{n}}$, there are N_b linear homogeneous equations of the type (5.26) describing the evolution dynamics of each one, all predicated upon the same discretized scalar fields denoted by the column vector $\mathbf{x}$ of unknowns. This can be neatly expressed as the simple matrix equation: $M\mathbf{x} = \mathbf{0}$ where M is an $N_b \times 2N$-matrix whose rows consist of the linear coefficients of the unknowns for each grain boundary. Further, the homogeneity of these equations allows us to scale the γ_i and χ_i simultaneously by the same constant without loss of generality. Because of this freedom,we choose to solve the system of linear equations using a constrained least squares method:

$$M\mathbf{x} = \mathbf{0} \implies |M\mathbf{x}|^2 = \mathbf{x}^T M^T M\mathbf{x} = 0$$

$$\mathbf{x}^T W \mathbf{x} = 1 \qquad \text{(Normalization constraint)}$$

$$\implies \delta\left[\mathbf{x}^T M^T M\mathbf{x} + \lambda\mathbf{x}^T W\mathbf{x}\right] = 0$$

$$\implies \boxed{\left(M^T M\right)\mathbf{x} + \lambda W\mathbf{x} = 0} \tag{5.27}$$

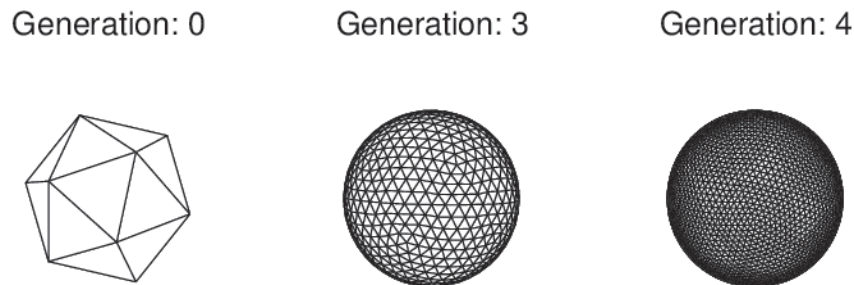Generation: 0   Generation: 3   Generation: 4

Figure 5.3: Recursive bisection of icosahedron edges followed by projection of nodes back to the unit sphere.

Here the matrix W is a positive diagonal matrix that specifies the weight of each sample point in the domain. The normalization constraint is necessary to prevent the trivial outcome of $\mathbf{x} = \mathbf{0}$. λ in the above equation is a Langrange multiplier and can be interpreted as one of the permitted values of $|M\mathbf{x}|^2$. Equation (5.27) is a generalized eigenvalue equation in which the eigenvector corresponding to the smallest eigenvalue (*i.e.* the smallest permissible positive value of λ) is the solution vector that we seek. The inverse problem of determining the energy and mobility from geometric and transport data of imaged grain boundaries has, therefore, been reduced to an easily solvable generalized eigenvalue problem. The most important caveat in this formulation is that the linear problem has to be over-determined *i.e.* $N_b > 2N$ for the smallest eigenvalue to be greater than zero. This

The rest of the chapter is devoted to numerical techniques focused on determining the linear coefficients in the discretized evolution equation (5.26).

5.5.2   Discretization of S^2, search and interpolation

In this section we describe a meshing prescription that can be applied in two cases of relevance: (a) in the case of the entirety of the unit sphere S^2 which is relevant in the evolution of an imagined spherical surface as a proof of concept (mentioned earlier in connection with Equation (5.25) and what we call the 'forward problem') and (b) the chosen subdomain of S^2 which is used in the inverse problem described at the end of Subsection 5.5.1. Both of these schemes rely upon successive bisection of the sides spherical triangles up to the desired resolution.
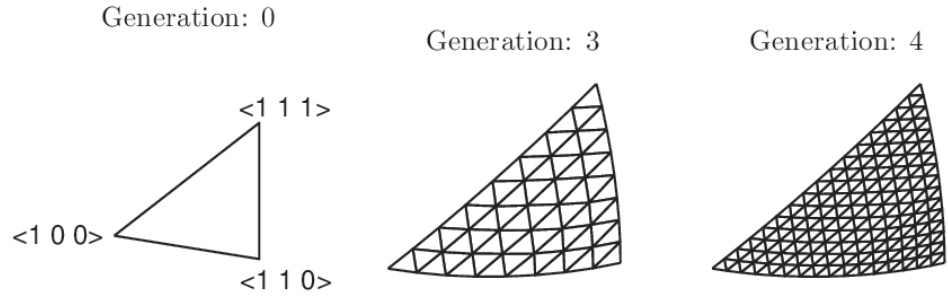
Figure 5.4: Recursive bisection of triangle edges followed by projection back to the unit sphere, for a region of S^2 delineated by the three crystallographic axes $\langle 100 \rangle$, $\langle 110 \rangle$ and $\langle 111 \rangle$.

We first address the case of meshing a symmetry-reduced subspace of S^2, which, for reasons described in Subsection 5.5.4, is a spherical triangle on the unit sphere for cubic symmetries. Suppose this triangle is specified by its vertices $\hat{\boldsymbol{n}}_0, \hat{\boldsymbol{n}}_1, \hat{\boldsymbol{n}}_2 \in S^2$. We choose a recursive scheme of meshing in which the edges of the 3D planar triangle are bisected and projected back on to the unit sphere, until the desired resolution is obtained. In our example, the new mesh nodes would be:

$$\frac{\hat{\boldsymbol{n}}_0 + \hat{\boldsymbol{n}}_1}{|\hat{\boldsymbol{n}}_0 + \hat{\boldsymbol{n}}_1|}, \quad \frac{\hat{\boldsymbol{n}}_1 + \hat{\boldsymbol{n}}_2}{|\hat{\boldsymbol{n}}_1 + \hat{\boldsymbol{n}}_2|}, \quad \frac{\hat{\boldsymbol{n}}_2 + \hat{\boldsymbol{n}}_0}{|\hat{\boldsymbol{n}}_2 + \hat{\boldsymbol{n}}_0|}$$

The generation of such a mesh to the desired generation of nodes is shown in Figure 5.4, for a specific choice of crystallographic axes.

In the case of the entire S^2-space, this prescription applied to the equilateral faces of a regular icosahedron results in a scheme equivalent to that of Fekete [78]. This results in a nearly equal-area sampling of the spherical surface (Figure 5.3).

We observe in both cases that the mesh elements partition the space of solid angles (4π in the case of the full sphere and $\pi/12$ in the case of the bounded subdomain) into a set of non-overlapping solid angles, each subtended by its respective mesh element. A query value of $\hat{\boldsymbol{n}}$ falls into exactly one of these 'bins'. The recursive nature of the binning suggests a similar search technique to determine the constituent bin of $\hat{\boldsymbol{n}}$. Such a search would scale as $log(N)$ where N is the total number of mesh elements in the domain. All that is required is a prescription to determine whether a given sample point $\hat{\boldsymbol{n}}$ lies within a spherical given triangle $\{\hat{\boldsymbol{n}}_0, \hat{\boldsymbol{n}}_1, \hat{\boldsymbol{n}}_2\}$. which we state directly: *$\hat{\boldsymbol{n}}$ lies in the solid angle delineated by $\{\hat{\boldsymbol{n}}_0, \hat{\boldsymbol{n}}_1, \hat{\boldsymbol{n}}_2\}$ if and only if there exists a $\lambda \in \mathbb{R}^+$ such that $\lambda\hat{\boldsymbol{n}}$ lies in the convex span of $\hat{\boldsymbol{n}}_0$, $\hat{\boldsymbol{n}}_1$ and $\hat{\boldsymbol{n}}_2$ i.e. if and only if there exist λ, α, β, γ such that $\lambda > 0$, $0 \leq \alpha, \beta, \gamma \leq 1$, $\alpha + \beta + \gamma = 1$ and $\lambda\hat{\boldsymbol{n}} = \alpha\hat{\boldsymbol{n}}_0 + \beta\hat{\boldsymbol{n}}_1 + \gamma\hat{\boldsymbol{n}}_2$.* It is observed that α, β, γ are in fact the barycentric coordinates [79] of $\lambda\hat{\boldsymbol{n}}$ in the plane of the triangle (Figure 5.5). We use these same barycentric coordinates to interpolate between the nodal values $\{f_0, f_1, f_2\}$ of a scalar field to obtain the estimated field value at $\hat{\boldsymbol{n}}$. This piecewise linear estimation of a continuous field is the same as that adopted by the finite element approach for solving partial differential equations.

5.5.3 Gradient of a piecewise continuous field

Our treatment of energy and inverse mobility as piecewise linear fields on nodes of a spherical mesh requires an estimate of the local gradient, which lies in the local tangent plane of S^2. In this section we provide an estimate of this by differentiating the piecewise linear field with respect to its barycentric parameters. Recall that within a region of S^2 bound by points $\{\hat{\boldsymbol{n}}_0, \hat{\boldsymbol{n}}_1, \hat{\boldsymbol{n}}_2\} \in S^2$, the scalar field is approximated by
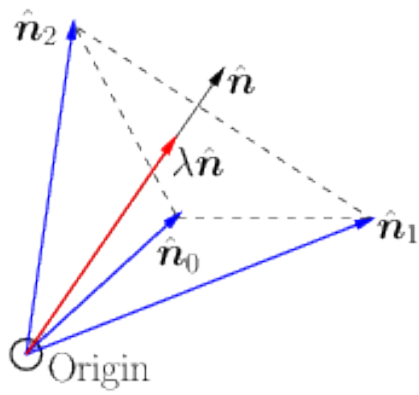
Figure 5.5: The condition for $\hat{n}$ to lie inside the solid angle subtended by $\{\hat{n}_0,\ \hat{n}_1,\ \hat{n}_2\}$: The vector $\lambda\hat{n}$ lies inside the triangle bound by $\{\hat{n}_0,\ \hat{n}_1,\ \hat{n}_2\}$ for some $\lambda > 0$.

linearly interpolating between the scalar values $\{f_0, f_1, f_2\}$ at these nodes:

$$f(\hat{\boldsymbol{n}}) \simeq (1 - \alpha - \beta)f_0 + \alpha f_1 + \beta f_2 \tag{5.28}$$

where $\alpha, \beta \in [0, 1]$ and $\beta \leq 1 - \alpha$. In the following analysis it is convenient to treat $\hat{\boldsymbol{n}}_0$, $\hat{\boldsymbol{n}}_1$ and $\hat{\boldsymbol{n}}_2$ in terms of their Cartesian components. A point inside the 3D triangle spanned by $\{\hat{\boldsymbol{n}}_0, \hat{\boldsymbol{n}}_1, \hat{\boldsymbol{n}}_2\}$ is given by:

$$\boldsymbol{x} = (1 - \alpha - \beta)\hat{\boldsymbol{n}}_0 + \alpha\hat{\boldsymbol{n}}_1 + \beta\hat{\boldsymbol{n}}_2 \tag{5.29}$$

a small in-plane change of which is given by:

$$\delta\boldsymbol{x} = -\left(\delta\alpha + \delta\beta\right)\hat{\boldsymbol{n}}_0 + \delta\alpha\hat{\boldsymbol{n}}_1 + \delta\beta\hat{\boldsymbol{n}}_2 = (\hat{\boldsymbol{n}}_1 - \hat{\boldsymbol{n}}_0)\,\delta\alpha + (\hat{\boldsymbol{n}}_2 - \hat{\boldsymbol{n}}_0)\,\delta\beta \tag{5.30}$$

This displacement can be parameterized in terms of the column vector of barycentric parameters $\boldsymbol{\rho} \equiv [\delta\alpha\ \delta\beta]^T$:

$$\delta\boldsymbol{x} = XD\boldsymbol{\rho} \tag{5.31}$$

$$X = [\hat{\boldsymbol{n}}_0\ \hat{\boldsymbol{n}}_1\ \hat{\boldsymbol{n}}_2]_{3\times3}$$

$$D = \begin{bmatrix} -1 & -1 \\ 1 & 0 \\ 0 & 1 \end{bmatrix}_{3\times2}$$

Further, if we define the column vector of field values $F \equiv [f_0\ f_1\ f_2]^T$, then we seek the gradient in the plane of the triangle as the direction of greatest change of $f(\hat{\boldsymbol{n}})$. The parameterized change in the scalar field is given by:

$$\delta f = F^T D\boldsymbol{\rho} \tag{5.32}$$

We determine the gradient by maximizing the value of δf subject to the constraint that $|\delta\boldsymbol{x}|^2 = 1$. Explicitly with a Lagrange multiplier λ,

$$\delta_{\boldsymbol{\rho}}\left[F^T D\boldsymbol{\rho} - \lambda\boldsymbol{\rho}^T (XD)^T XD\boldsymbol{\rho}\right] = 0 \tag{5.33}$$

$$\implies \boldsymbol{\rho} = \frac{1}{\lambda}\underbrace{\left[(XD)^T XD\right]^{-1}}_{M}D^T F \tag{5.34}$$

We determine the Lagrange multiplier by explicitly enforcing the constraint:

$$|\delta\boldsymbol{x}|^2 = 1$$

$$\implies \lambda = \sqrt{F^T D\left(M^{-1}\right)^T D^T F}$$

This gives the computationally convenient expression for the vector gradient:

$$\nabla f = (\delta f)\,\delta\boldsymbol{x}$$

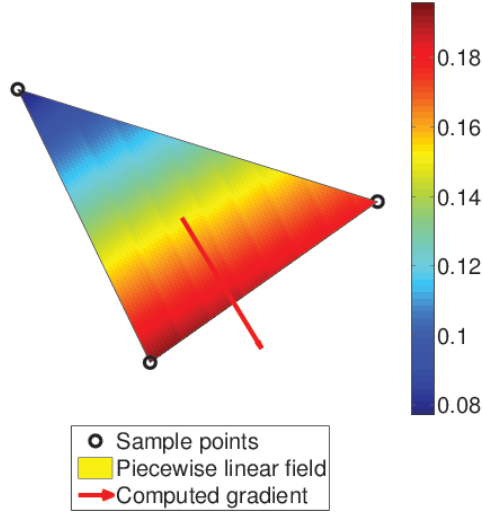$$\boxed{\nabla f(\hat{\boldsymbol{n}}) \simeq XD\left[(XD)^T XD\right]^{-1}D^T F} \tag{5.35}$$

Figure 5.6: Estimated gradient in the plane of a mesh element with linear interpolation over the element area. The gradient is seen to be perpendicular to the level set.

and as expected, it is constant in the plane of the triangle in that is has no dependence on α or β. The results of such a computation for an arbitrary mesh element are shown in Figure 5.6.

We close by describing the application of Equation (5.35) to the derivative term in the numerical evolution equation (5.26), thereby substantiating the earlier claim of elegantly expressing the entire equation linearly in the unknown vector $\mathbf{x}$. The left-hand side and the first term in the right-hand side of (5.26) are trivially linear in the unknowns γ_μ and $\chi_\mu \equiv 1/M_\mu$. We note that the second term is a sum of terms of the form: $\boldsymbol{v}_\mu \cdot \Delta \boldsymbol{t}^j_{\nu\rho} \times \boldsymbol{\xi}_j$, where $\boldsymbol{v}_\mu \equiv d\boldsymbol{x}_\mu/dt$ is the node velocity and $\Delta \boldsymbol{t}^j_{\nu\rho} \equiv \boldsymbol{x}^{(j)}_\nu - \boldsymbol{x}^{(j)}_\rho$ is the segment of the mesh element j opposite to the node μ (the blue 'tangent' segments in Figure 5.2(b)). If we are interested in a query $\hat{\boldsymbol{n}} = n_x \hat{\boldsymbol{x}} + n_y \hat{\boldsymbol{y}} + n_z \hat{\boldsymbol{z}} \in S^2$ whose constituent bin is delineated by $\{\hat{\boldsymbol{n}}_0,\ \hat{\boldsymbol{n}}_1,\ \hat{\boldsymbol{n}}_2\}$ at which points the field values are $\gamma_0, \gamma_1, \gamma_2$ respectively, we express the capillarity vector in the following manner with barycentric interpolation and the gradient formulation in Equation (5.35):

$$\boldsymbol{\xi}_j = \gamma(\hat{\boldsymbol{n}})\hat{\boldsymbol{n}} + \nabla\gamma(\hat{\boldsymbol{n}})$$

$$= \underbrace{[(1 - \alpha - \beta)\gamma_0 + \alpha\gamma_1 + \beta\gamma_2]}_{\text{barycentric interpolation}} \begin{bmatrix} n_x \\ n_y \\ n_z \end{bmatrix} + XD \left[(XD)^T (XD) \right]^{-1} D^T \begin{bmatrix} \gamma_0 \\ \gamma_1 \\ \gamma_2 \end{bmatrix}$$

$$= \underbrace{\left\{ \begin{bmatrix} n_x \\ n_y \\ n_z \end{bmatrix} [1 - \alpha - \beta\ \alpha\ \beta] + XD \left[(XD)^T (XD) \right]^{-1} D^T \right\}}_{\text{capillarity operator } \mathbb{X}} \begin{bmatrix} \gamma_0 \\ \gamma_1 \\ \gamma_2 \end{bmatrix}$$

87

The capillarity is thus approximated as a 3×3 linear operator $\mathbb{X}$ acting on a vector of the unknowns. Further, the cross product with the tangent segment is expressed as another linear operation in terms of the corresponding skew matrix $\mathbb{K}_{\Delta t}$:

$$\Delta \boldsymbol{t} \times \boldsymbol{\xi} = \underbrace{\begin{bmatrix} 0 & -(\Delta \boldsymbol{t})_z & (\Delta \boldsymbol{t})_y \\ (\Delta \boldsymbol{t})_z & 0 & -(\Delta \boldsymbol{t})_x \\ -(\Delta \boldsymbol{t})_y & (\Delta \boldsymbol{t})_x & 0 \end{bmatrix}}_{\mathbb{K}_{\Delta t}} \begin{bmatrix} \xi_x \\ \xi_y \\ \xi_z \end{bmatrix}$$

$$\implies \boxed{\boldsymbol{v}_\mu \cdot \Delta \boldsymbol{t} \times \boldsymbol{\xi} = [v_{\mu,x} \ v_{\mu,y} \ v_{\mu,z}] \, \mathbb{K}_{\Delta t} \mathbb{X} \begin{bmatrix} \gamma_0 \\ \gamma_1 \\ \gamma_2 \end{bmatrix}} \tag{5.36}$$

Equation (5.36) describes in simple terms how to express the derivative term in the evolution equation (5.26) as a linear combination of the unknowns $\gamma_0, \gamma_1, \gamma_2$. These coefficients are, as already mentioned, dependent only on the mesh geometry ($\mathbb{K}_{\Delta t}$ and $\mathbb{X}$) and transport ($\boldsymbol{v}_\mu$). Thus we have established a way to express the entire equation as linear in the unknowns.

5.5.4 Crystal symmetry considerations

The characterization developed thus far of grain boundary geometry and transport as well as the domain S^2 of boundary normals is applicable to all polycrystalline materials irrespective of their crystallographic symmetry, the presence of which results in numerically different misorientations across grain boundaries actually being atomistically equivalent. This implies a highly nontrivial and difficult-to-visualize connectivity imposed on the space of misorientations. In this section we describe the need and method to negotiate this redundancy.

The set of rotation operators that leave a crystal lattice invariant form a group under composition of rotations, a subgroup of the symmetry group of that crystal. Each of these can be expressed as an operator $R(\hat{\boldsymbol{n}}, \theta)$ described by an angle of rotation θ about an axis $\hat{\boldsymbol{n}}$. For example, the cubic rotational symmetry group has 24 elements while the hexagonal one has 12. Given a crystal system with N rotational symmetry operators, the entire space of orientations is divided into N equal-volume subspaces, each of which contains one equivalent copy of every possible unique orientation of the crystal. Materials scientists studying polycrystals restrict themselves to one of these equivalent regions, any lattice orientation in the material being referred to by its equivalent point in this 'fundamental zone'. Equivalent orientations in other zones can be obtained by transforming the fundamental zone orientations by the rotational symmetry operators. A convenient method for calculating a fundamental zone equivalent of a given orientation is to choose that symmetry-transformed orientation that has the least angular deviation from the identity orientation. In
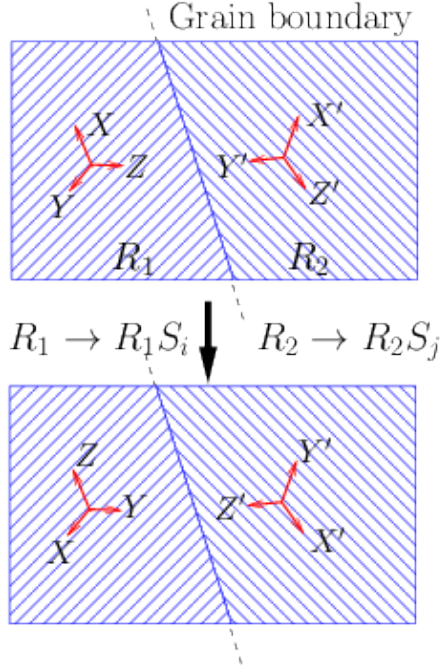
Figure 5.7: Invariance of the atomistic configuration that forms a grain boundary (pictured by crystallographic planes in blue) on transforming each lattice by any of its rotational symmetry operators. The misorientation of lattice 2 with respect to Lattice 1 is $\Delta R = R_2 R_1^{-1}$ in the matrix representation.

short, if $O(\hat{\boldsymbol{n}}, \theta) \in SO(3)$ is an orientation in matrix form of a crystal lattice that has N rotational symmetry operators $S_i \in SO(3)$, $i = 1, 2, \ldots, N$ then the equivalent fundamental zone orientation is given by:

$$O_{FZ} = \left\{ S_i O S_i^{-1} \;\middle|\; S_i = \arg\max_{S_j} \mathrm{Tr}\left(S_j O S_j^{-1}\right) \right\} \tag{5.37}$$

We proceed to describe how crystal symmetry influences the connectivity of the five-parameter space of grain boundary character. Consider a mesoscopically flat patch of an interface between lattices 1 and 2 (Figure 5.7) defined by the set $(\Delta R, \hat{\boldsymbol{n}})$ where $\Delta R \in SO(3)$ is the difference in orientation from 1 to 2 (equivalently, the orientation of 2 in the frame of 1) and $\hat{\boldsymbol{n}}$ is the unit normal to the grain boundary at that point, in frame 1. If $\{S_i\}_{i=1}^N$ and $\{S_i'\}_{i=1}^N$ are the rotational symmetry operators of the lattices 1 and 2 respectively, then $S_i' = (\Delta R)S_i(\Delta R)^{-1}$ $\forall i = 1, 2, \ldots, N$. The transformations S_i acting on the axes of frame 1 and S_j' on those of frame 2 result in the same atomistic structure on either side of the boundary as did the original misorientation ΔR. The new atomistically equivalent misorientation is $\Delta R' = \left(S_j' \Delta R\right) S_i^{-1} = \Delta R S_j S_i^{-1}$ with the new boundary normal in the transformed 1 frame being $\hat{\boldsymbol{n}}' = S_i^{-1}\hat{\boldsymbol{n}}$. The grain boundary descriptors $(\Delta R, \hat{\boldsymbol{n}})$ and $\left(\Delta R S_j S_i^{-1}, S_i^{-1}\hat{\boldsymbol{n}}\right)$ therefore reference the same grain boundary as far as bicrystal structure is concerned. We make use of this redundancy by choosing to transform $\hat{\boldsymbol{n}} \to S_i\hat{\boldsymbol{n}}$ so that we are required to query a minimum subvolume of S^2, with the understanding that the original grain boundary
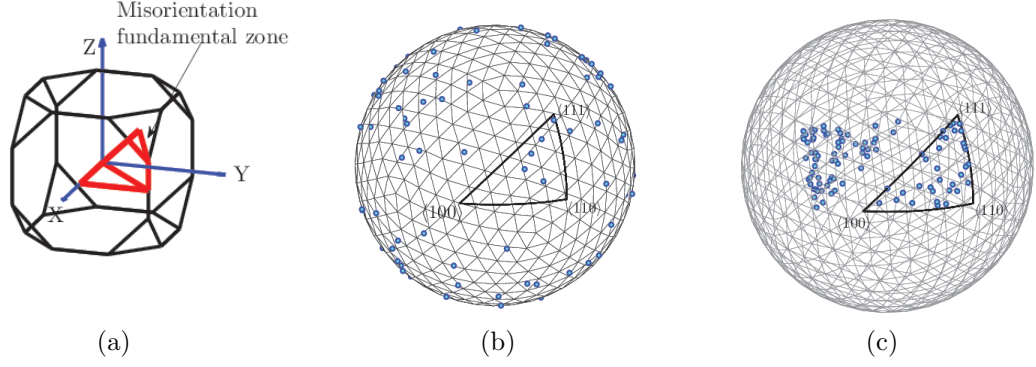
Figure 5.8: **(a)** The smallest complete region of orientation space marked in red, expressed in the Rodrigues-Frank representation. **(b)** 100 random samplings of S^2 with the delineated subregion marked, **(c)** The symmetry reduction of the scattered points into the region of interest according to Equation (5.38). We note that about half the points are on the far side of the unit sphere, owing to the absolute value in Equation(5.38). This is indicative of the additional symmetry due to orientation switching, which are improper rotations.

character can easily be recovered by applying the inverse transformation on $\hat{\boldsymbol{n}}$ as well as the misorientation ΔR. The minimum subvolume requirement directly translates into having fewer unknowns in Equation (5.26), thereby saving on computer resources.

While there exist a generalized prescription for transforming a given $\hat{\boldsymbol{n}}$ into the desired subregion of S^2 [80], *which is in fact misorientation-dependent*, we rely for simplicity on a method that is specific to a 60° misorientation about the $\langle 111 \rangle$ crystallographic axes for the highest-symmetry case, the cubic lattice. It is known that the fundamental zone of misorientations in cubic polycrystals is delineated in Rodrigues-Frank space [81] by the three axes of the standard stereographic triangle (SST) namely $\langle 100 \rangle$, $\langle 110 \rangle$ and $\langle 111 \rangle$ (Figure 5.8**(a)**). We choose the elements of S^2 corresponding to these directions (or crystallographic equivalents thereof) as the boundaries of the subspace that we choose to transform into. We bring a query $\hat{\boldsymbol{n}} \in S^2$ into this spherical triangle by minimizing the sum of its angular deviation from these vectors, with the following objective function involving the set of rotational symmetry operators $\{S_i\}$ and the delineating vectors $\hat{\boldsymbol{a}}_j$:

$$\hat{\boldsymbol{n}}_{\text{transformed}} = S_{\text{max}}\hat{\boldsymbol{n}} \tag{5.38}$$

$$\text{where } S_{\text{max}} = \arg\max_{S_i} \sum_{j=1}^{N} |(S_i\hat{\boldsymbol{n}}) \cdot \hat{\boldsymbol{a}}_j|$$

The particular manner of transformation implemented in Equation (5.38) partitions the space of S^2 into two sections: those points that are accessible by proper symmetry transformations alone and those by improper transformations. This is indicated in the example in Figure 5.8(c) where roughly half of the randomly generated points on the spherical surface have been transformed into the region of S^2 delineated not by the $\hat{\boldsymbol{a}}_j$, but the $-\hat{\boldsymbol{a}}_j$. In order to bring these $\hat{\boldsymbol{n}}$ into the desired region, one would have to reflect them about the origin. This is not because of an inadequate choice of objective function, but indicative of the degeneracy in the definition of the grain boundary descriptor parameters, in particular the 2-parameter boundary inclination. In the larger context of the polycrystal, this is purely a matter of choice, in terms of the local boundary normal $\hat{\boldsymbol{n}}$ extending into one crystal forming the grain boundary or the other.

Thus in our quest to successfully reduce the number of unknowns in the evolution equation (5.26), we are now saddled with the problem of negotiating the set of equivalent configurations on the unit sphere, which number $2N$ in all, the *total* number of symmetry operators of the crystal lattice of the material, rotations and reflections included. These are partitioned into 2 sets of N each, and the members of each set can all be transformed into one another through the application of the N rotational symmetry operators, but they cannot cross-transform, since one would require an improper rotation to do so. This is illustrated in Figure 5.9(a). For cubic symmetry, there are 24 equivalent 'blue' regions that transform into the chosen 'red' region through symmetry rotations of every point in it (one symmetry operation per blue region), and 24 equivalent 'green' regions that transform through improper symmetry operations. 'Blue' and 'red' regions can never inter-transform through rotations alone.

With the need to transform every $\hat{\boldsymbol{n}} \in S^2$ into the chosen region comes the requirement to transform every vector in it appropriately, since they all have unique local identities. These vectors include every constituent part of Equation (5.36), namely the velocity $\boldsymbol{v}_\mu$, local element edges $\Delta\boldsymbol{t}$ and the capillarity vector $\boldsymbol{\xi}$ itself. We address in one stroke all these transformations indirectly by describing how to transform a convenient local basis in which all these vectors can be expressed. This basis is simply the local spherical polar basis $\{\hat{\boldsymbol{e}}_r,\ \hat{\boldsymbol{e}}_\theta,\ \hat{\boldsymbol{e}}_\phi\}$ on the surface of the unit sphere. It is imperative that this transformation of basis be done not by any arbitrary rotation, but through symmetry operations alone, whether proper or improper. This ensures that the set of transformed basis vectors are oriented in the exactly same manner within the target S^2 subregion as they were with their constituent subregion. This is clarified in Figure 5.9(b) and (c). In (b), the blue region transforms into the red region by a proper symmetry operator (namely, rotation of $60°$ about $\langle 111 \rangle$). Through the same transformation, the new basis $\{\hat{\boldsymbol{e}}'_r,\ \hat{\boldsymbol{e}}'_\theta,\ \hat{\boldsymbol{e}}'_\phi\}$ is oriented in the exactly same manner within the red region as the original basis $\{\hat{\boldsymbol{e}}_r,\ \hat{\boldsymbol{e}}_\theta,\ \hat{\boldsymbol{e}}_\phi\}$ was with respect to the blue
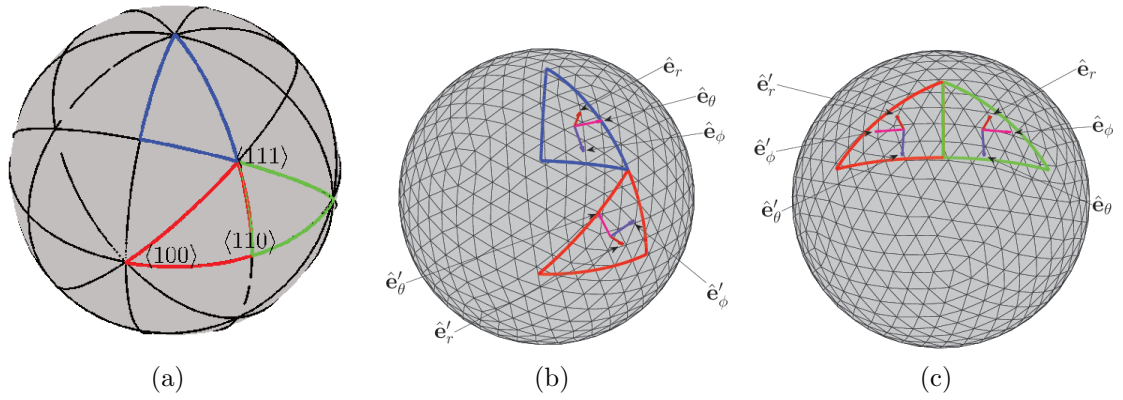
Figure 5.9: **(a)** Chosen subregion delineated by $\langle 100 \rangle$, $\langle 110 \rangle$ and $\langle 111 \rangle$, along with two equivalent zones, one of which transforms into the chosen region through proper symmetry operations (blue), and another through improper symmetry operations (green). Transformation of local spherical polar basis $\{\hat{\boldsymbol{e}}_r,\ \hat{\boldsymbol{e}}_\theta,\ \hat{\boldsymbol{e}}_\phi\} \rightarrow \{\hat{\boldsymbol{e}}'_r,\ \hat{\boldsymbol{e}}'_\theta,\ \hat{\boldsymbol{e}}'_\phi\}$ through **(b)** proper rotations, and **(c)** improper rotations.

region. The transformation being a proper rotation, the handedness of the basis is preserved. The vectors $\boldsymbol{v}_\mu$, $\Delta\boldsymbol{t}$ and $\boldsymbol{\xi}$ whose components in the basis $\{\hat{\boldsymbol{e}}_r,\ \hat{\boldsymbol{e}}_\theta,\ \hat{\boldsymbol{e}}_\phi\}$ were already known, can now be safely projected into the new basis while maintaining their configurations with respect to each other. The same is seen in Figure 5.9(**c**), except that the handedness of the basis changes, reflecting (no pun intended) the improper nature of the transformation. Any vector $\boldsymbol{\chi} = [\chi_0\ \chi_1\ \chi_2]^T$ is transformed from a local spherical polar basis to the corresponding basis in the reduced subregion by the following transformation:

$$\boldsymbol{\chi}' = B_2 B_1^T \boldsymbol{\chi} \tag{5.39}$$

where $B_1 = [\hat{\boldsymbol{e}}_r\ \hat{\boldsymbol{e}}_\theta\ \hat{\boldsymbol{e}}_\phi]_{3\times3}$ is the matrix formed with the polar basis vectors as its columns, and likewise $B_2 = [\hat{\boldsymbol{e}}'_r\ \hat{\boldsymbol{e}}'_\theta\ \hat{\boldsymbol{e}}'_\phi]_{3\times3}$.

We have thus detailed a consistent method for transformation of the local boundary inclination (expressed in one or the other crystal frame associated with the grain boundary) and tangent-plane related physical quantities into a convenient subregion of S^2. For stress again that the transformation into the subregion described in Figure 5.9 is specific to the $60°$ misorientation about $\langle 111\rangle$. The method outlined is however applicable to subregions of S^2 corresponding to any grain boundary misorientation. The choice of underlying misorientation is for illustrative purposes and is explained in chapter 6, Section 6.5.2.

5.6 Interface tracking

We finally prescribe a methodology to estimate the velocity field on an interface on a node-to-node basis (Figure 5.1), given the two snapshots of the interface before and after its *differential* transport (the $d\boldsymbol{x}_\mu/dt = \boldsymbol{v}_\mu$ in Equation (5.26)), what we call the interface tracking problem. As already stated, this is to be applied to imaged grain boundaries and is generalized insofar as to account for changes in the geometry of the interface, such as size (and consequently number of sample points), local curvature, surface orientation and torsion. The emphasis on differential migration is important because it permits us to make a qualitative assumption about the grain boundary transport: that the sample nodes of the interface take the straightest, simplest path in the intervening space to reach the configuration described the the target set of points without 'wiggle'. A schematic of such transport is shown in Figure 5.10 in the presence of a variety of exotic morphological changes. In each case, the original surface has 20 nodes while the target surface has 40 nodes. We state in simple words the interface tracking problem and our proposed solution.

- We are given an M-strong set of 3D sample points $\mathbb{X} \equiv \{\boldsymbol{x}_i\}$ denoting the original interface and another N-strong set $\mathbb{Y} \equiv \{\boldsymbol{y}_j\}$ denoting the target interface.
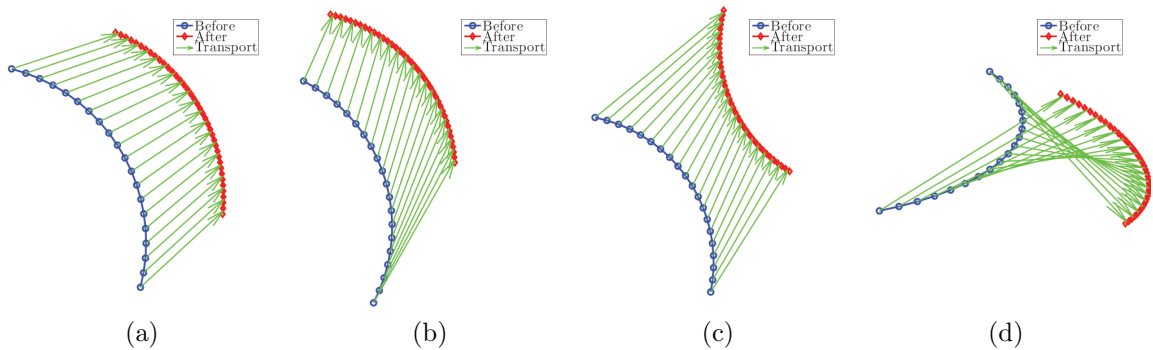
Figure 5.10: **(a)** Schematic of boundary transport illustrating the abilities of the boundary tracking algorithm, particularly with **(b)** target surface oriented differently, **(c)** inverted curvature and **(d)** 3D torsion.

These two sets represent an imaged interface before and after differential migration respectively. Note that M may not be equal to N. In practice this could happen because the size of the grain boundary changed during transport, or the sampling for the different states of the material volume was done at different resolutions, or a combination of both.

- We seek a set of M displacement vectors $\mathbb{D} \equiv \{\Delta \boldsymbol{x}_i\}$ in 3D for each $\boldsymbol{x}_i$ such that the set $\{\boldsymbol{x}_i + \Delta \boldsymbol{x}_i\}$ mimics the configuration of the target surface $\mathbb{Y}$ as closely as possible, with as uniform a sampling as possible.

- Under these conditions, it is assumed that in the time of transport Δt (decided in the particular experiment!), the intermediate positions of the boundary nodes were:

$$\boldsymbol{x}_i^{(\text{inter})} \left(\epsilon \Delta t \right) = \boldsymbol{x}_i + \epsilon \Delta \boldsymbol{x}_i \tag{5.40}$$
$$\text{where } 0 \leq \epsilon \leq 1$$

- The velocity field is then simply given by:

$$\boldsymbol{v}_i = \frac{\Delta \boldsymbol{x}}{\Delta t}$$

We assert that this problem is easily solved using the well-established linear optimization algorithm for which there exist a variety of numerical software packages for easy implementation [82, 83, 56]. We calculate each displacement $\Delta \boldsymbol{x}_i$ as a weighted sum of *all* possible displacements from $\boldsymbol{x}_i \in \mathbb{X}$ to every $\boldsymbol{y}_j \in \mathbb{Y}$:

$$\Delta \boldsymbol{x}_i = \sum_{j=1}^{N} C_{ij} \left(\boldsymbol{y}_j - \boldsymbol{x}_i \right) \tag{5.41}$$
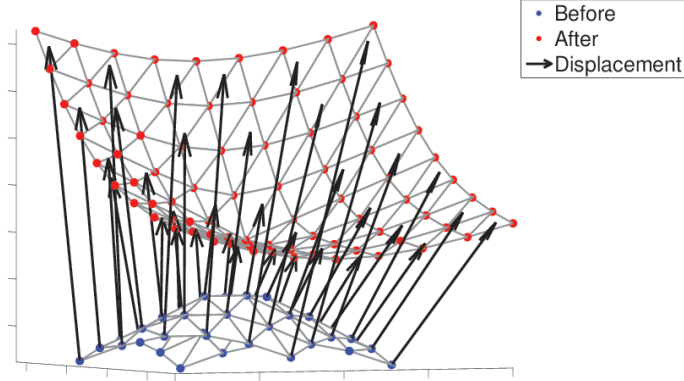
94

Figure 5.11: Example of the optimized transport algorithm acting on a 3D surface with inverted curvature and slight reorientation.

The coefficients C_{ij} are determined by the following linear optimization problem in the unknowns σ_{ij}:

$$C_{ij} = \arg\min_{\sigma_{ij}} \left\{ \sum_{i=1}^{M} \sum_{j=1}^{N} \sigma_{ij} |\boldsymbol{y}_j - \boldsymbol{x}_i|^2 \right\} \tag{5.42}$$

subject to the constraints:

$$\sigma_{ij} \geq 0 \ \forall \ i = 1, 2, \ldots, M \text{ and } j = 1, 2, \ldots, N \tag{5.43}$$

$$\sum_{j=1}^{N} \sigma_{ij} = 1 \ \forall \ i = 1, 2, \ldots M \tag{5.44}$$

$$\sum_{i=1}^{N} \sigma_{ij} = \frac{M}{N} \ \forall \ j = 1, 2, \ldots N \tag{5.45}$$

The objective function in Equation (5.42) attempts to find the shortest possible aggregate displacement emanating from the $\boldsymbol{x}_i$. The positivity constraint (5.43) ensures directionality of the displacements $\Delta \boldsymbol{x}_i$ towards the target surface. Constraint (5.44) ensures that the displacements actually terminate on the target surface and not before or after, while the equi-weighting constraint (5.45) adjusts the displacements so that the final positions sample the target surface as uniformly as can be managed. An instance of this algorithm applied to a meshed surface is shown in Figure 5.11.

We note in Figures 5.10 and 5.11 the edges and corners of the original surface do not actually migrate to their corresponding components in the target surface. This is a consequence of the manner of framing the optimization problem. We circumvent

this difficulty by separately evolving the different topological features (in the case of a grain boundary network, the boundary interiors, triple lines and quad points) using the optimal transport algorithm described above. A more sophisticated treatment of this geometrical constraint takes the problem outside the realm of linear optimization and therefore easy computation.

Chapter 6

Results

In this chapter we present the results of the preliminary processing of the iron data and the subsequent analysis of the obtained microstructure with the tools developed in the chapters thus far. The results are classified into the following broad groups:

1. We begin farthest upstream with particulars of the reconstruction of the α-iron microstructure. These include details concerning the experiment itself, such as the estimated number of Bragg peaks per grain, the reconstruction itself and a qualitative analysis of certain isolated low-confidence regions therein.

2. Bulk statistics of the microstructure are analyzed next: grain volume, orientational and shape texture, number of neighbors and the grain boundary chatacter distribution.

3. The two-step alignment of the pre-anneal and post-anneal microstructure volumes, specifically the layer registration followed by the alignment of select grains and the subsequent tracking of specific grains and their boundaries.

4. Digressing slightly from bulk statistics of polycrystalline α-iron, we present two proof-of-concept validations of the enegry and mobility computation formalism developed earlier in Chapter 5.

6.1   Results from the diffraction experiment

We describe in this section particulars concerning the data collection and the reconstruction. The initial volume scanned was from a sample cut out of a rolled and annealed piece of α-iron (BCC crystal structure) obtained from Center for Iron and Steelmaking Research at Carnegie Mellon University. The energy of the X-ray photons was set to be $E = 65.351$ keV. The scan began at a point $2mm$ below a notch in the sample, which was presumably a consequence of imprecise machining. 66 layers of the sample were scanned at a rotation interval of $0.25°$ at a layer separation of $3\mu m$.

The acquisition time for each detector image was about 0.33 seconds. In this manner, a volume of about $1mm \times 1mm \times 0.195mm$ was scanned. The sample was then removed from its mount and annealed in a tube furnace at a temperature of $600°C$ for half an hour in an atmosphere of forming gas $(N_2 + 3\%H_2)$. After the anneal cycle an attempt was made to remount the sample as closely to the pre-anneal configuration as could be managed by hand. This greatly helped the post-reconstruction digital registration of the volumes (described in Section 6.3). For the post-anneal scan we attempted to capture a larger region of the sample by imaging the diffraction peaks for 10 additional layers, 5 above the original volume and 5 below. The rationale was to be able to capture what happens to specific grains near the edges of the scanned volume. Unfortunately due to time constraints we were able to scan only 65 layers beginning from 5 layers above the starting point of the pre-anneal volume. Any subsequent attempt to track microstructural features through the anneal cycle obviously had to be restricted to the overlapping region between the two volumes, which consists of 60 layers.

On completion of the parameters Monte Carlo step, the relevant geometric parameters of the experiment (defined in Chapter 2) were determined to be:

Parameter	Detector 0	Detector 1	Detector 2
Detector distance L (mm)	5.095(5)	7.083(5)	9.064(5)
Beam center J (pixels)	927	938	950
Beam center K (pixels)	2030	2026	2022

Table 6.1: Parameters of the experimental geometry determined by a Monte Carlo method.

To reiterate, the origin of the detector coordinates is the top left corner of the detector. L denotes the estimated distance between the rotation axis of the sample and the detector. Our first calculation is the estimated number of observed Bragg peaks per grain (or more specifically, per unique orientation in the sample plane), the idea being that for a single voxel in the sample space, optimization of each orientation against a greater number of Bragg peaks makes for a more reliable reconstruction. In order to do this, we require knowledge of the relevant volume in the *reciprocal* lattice that is responsible for scattering through the von Laue criterion. As described in Chapter 2, the maximum size of the reciprocal lattice vector $\boldsymbol{G}$ is estimated by how far up the detector scattering was detected:

$$|\boldsymbol{G}| = \frac{2\pi}{a_0}\sqrt{h^2 + k^2 + l^2} = Q = \frac{4\pi}{\lambda}\sin\theta \qquad (6.1)$$

where $(h, \; k, \; l)$ are the Miller indices of the reciprocal lattice vector. With diffraction being observed as far as about $2.5mm$ up the detector (which is about $3.03mm$ tall

)at distance $L = 5.095mm$, we get:

$$Q_{\max} = \frac{4\pi}{\lambda} \sin \theta_{\max} = \frac{4\pi E}{hc} \sin \left[\frac{1}{2} \tan^{-1} \left(\frac{2.5}{5.095} \right) \right] \simeq 14 \text{Å}^{-1}$$

We thus seek to find the number of relevant Bragg reflections that fall within the reciprocal space sphere of radius $Q_{\max}$. This would be easy to compute in the case of a simple cubic crystal, but is complicated by the fact that a body-centered cubic material has the requirement that $h + k + l$ be even for an allowed diffraction. The task is achieved by the following Matlab code which takes as its input the maximum scattering vector magnitude we choose to consider (`Qmax`) in Å^{-1} and the lattice constant `a0` in Å:

```
function [ SC, FCC, BCC ] = GetBraggPeaksCubic( Qmax, a0 )
    Qmax = round( Qmax );
    [ y, x, z ] = meshgrid( -Qmax:Qmax, -Qmax:Qmax, -Qmax:Qmax );
    x = x(:); y = y(:); z = z(:);
    G = [ x y z ]';
    G( :, (2*pi/a0)*sqrt( sum( G.^2 ) ) > Qmax ) = [];
    G( :, all( G == 0 ) ) = [];
    % simple cubic...
    SC = G';
    % face centered cubic...
    FCC = G( :, all( rem( G, 2 ) == 0 ) | all( rem( G, 2 ) ~= 0 ) )';
    % body centered cubic...
    BCC = G( :, rem( sum( G ), 2 ) == 0 )';
end
```

%%

```
[ ~, ~, bcc ] = GetBraggPeaksCubic( 14, 2.87 ); % lattice constant of bcc iron
bccUniq = bcc( bcc(:,3)>0, : );
```

%%

The final array `bccUniq` returns all the unique (h, k, l) triples that are eligible to produce scattering over a complete rotation of the sample. For our input parameters of $Q_{\max} = 14 \text{Å}^{-1}$ and lattice constant $a_0 = 2.87 \text{Å}$, we see that each sample space orientation corresponds to 243 Bragg peaks on the detector. For comparison, at the same beam energy of 65.351 keV, the orientations are reliably determined in the usual gold wire sample used for calibration of the nf-HEDM apparatus (face-centered cubic, $a_0 = 4.078 \text{Å}$) using about 90 Bragg peaks per orientation at a $Q_{\max}$ of 9Å (*i.e.* using scattering from about halfway up the detector). We can therefore be certain to a very high degree of the orientation map obtained from the diffraction data of the α-iron.

The results of the reconstruction of one layer of the α-iron with these parameters is shown in Figure 6.1. The following qualitative features of the reconstruction and microstructure are observed:

- The high confidence in the middle of the grains and the sharp definition of the grain boundaries with the expected confidence around 0.5 is a testament to the success in determining the geometric parameters of the experiment to a high degree of precision.

- The high confidence is also an indication that the original rolled microstructure was successfully recrystallized to obtain well-ordered grains. Further results on the crystallographic isotropy of the grains thus formed are given in Section 6.2.

- We speculate that the areas of low confidence are voids resulting from internal fracture due to the rolling of the sample in a mill, around which the material recovered and recrystallized into well-ordered grains. Our guess is based on the gradual drop in confidence at the periphery of these features, which is characteristic of imaged edges in nf-HEDM (Figure 6.2). In Figure 6.3, we can see the feature receding as we step through the sample. We observe the same feature in both anneal states (Figure 6.4), which is an indication that the feature is likely not the result of incomplete recovery/recrystallization. It is necessary to perform a tomography scan of the volume to confirm the presence of the crack.

The presence of the voids, if indeed that is what the low confidence regions are, constitute free surfaces inside the sample volume and has implications for the applicability of the energy/mobility theory and computational scheme described in Chapter 5, which assumes that the interfaces in question are grain-grain interfaces, as opposed to free surfaces. The theory of intersecting grain boundaries at free surfaces is more involved [84, 85] and is outside the scope of this thesis. In order to maintain rigor, one would have to exclude the grain boundaries that terminate at a free surface (namely, the insides of such voids as well as the boundaries along the sample edge) from the set of boundaries under consideration.

6.2   Bulk grain statistics

This section deals with statistical features of the α-iron microstructure with focus on the comparison between the pre- and post-anneal states. This is in contrast to explicit quantification of the geometry and transport of grain boundaries with the tools developed in Chapter 5. We begin by stating some simple quantities of interest, namely the number of grains and grain boundaries in the sample; summarized in Table 6.2. The pre-anneal and post-anneal comparisons indicate a large number of grain extinctions.
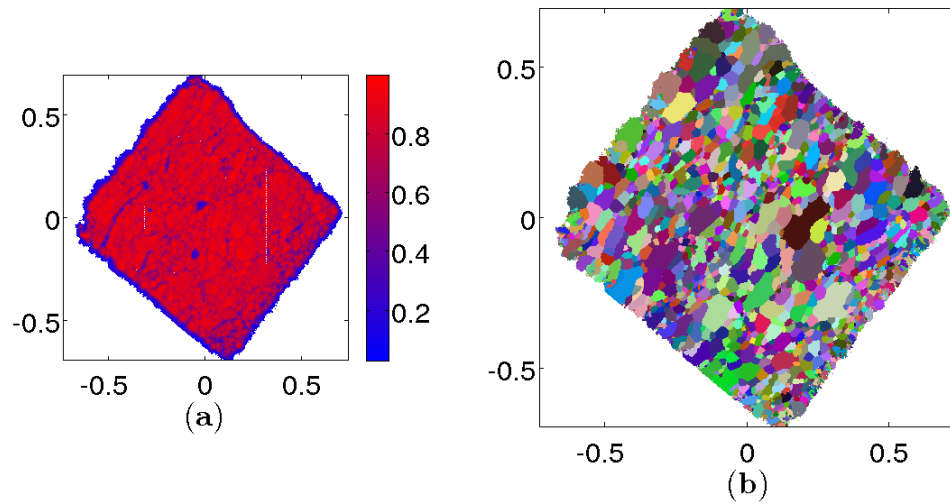
Figure 6.1: **(a)** Confidence metric that expresses the fraction of overlap of simulated diffraction from each sample voxel with observed diffraction. **(b)** Orientation field colored according to Rodrigues-Frank components.
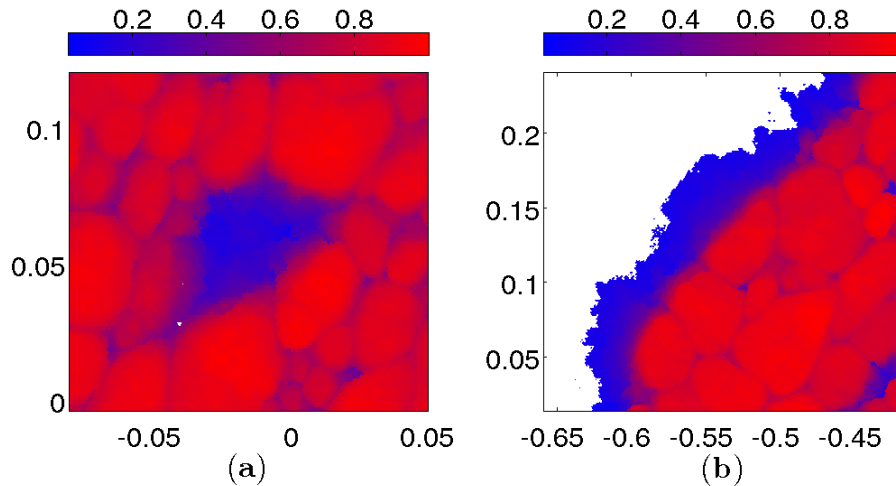

Figure 6.2: Comparison of the reconstruction features of a possible void **(b)** with those of the sample edge **(a)**. nf-HEDM reconstructions at the edge of a sample display not an abrupt discontinuity in the orientation field, but a gradual decrease in the confidence past the sample edge, were microstructure does not exist. This is a result of the forward modeling algorithm attempting to adjust the orientation for maximum overlap of simulated diffraction with observed diffraction. We notice the same features at the periphery of the low confidence region.
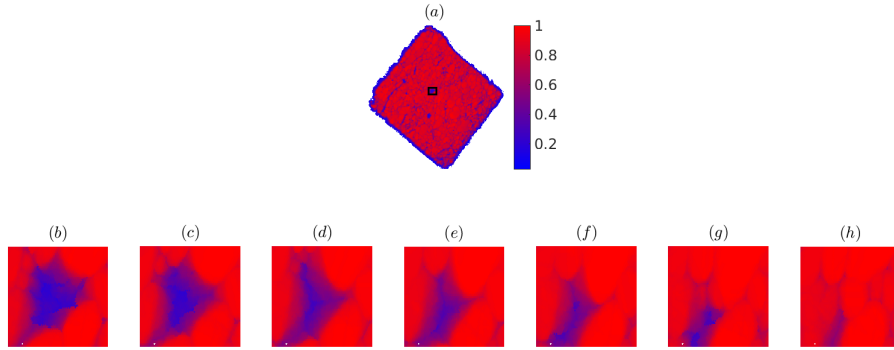
Figure 6.3: Profile of the possible void in the sample layer (position shown in **(a)**), as we step through the layers 1 (**(b)**) through 7 (**(h)**)
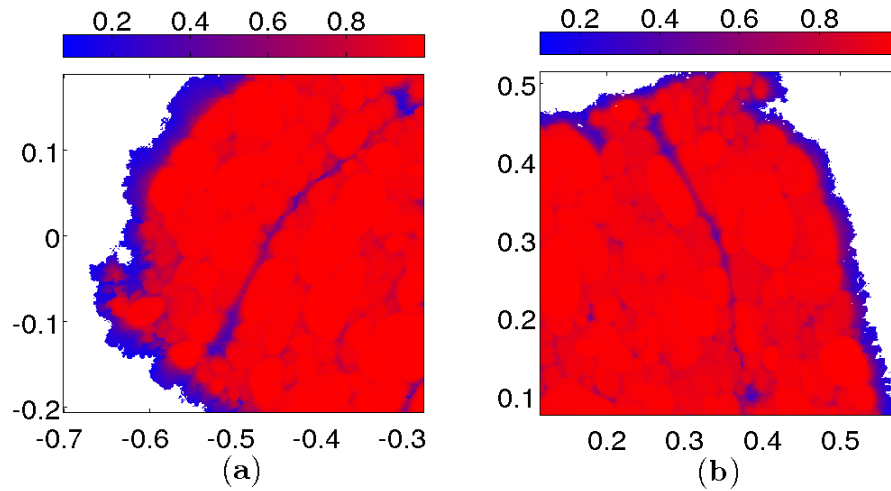
Figure 6.4: Presence of a possible void-like feature nearly unchanged in both the pre-anneal state **(a)** and post-anneal state **(b)**.

Table 6.2: Number of grains and grain boundaries in the sample

	Pre-anneal	**Post-anneal**
Grains	20039	13094
Grain boundaries (internal)	109389	74130
Free surfaces	8030	5078
Mean grain volume (μm^3)	9342	14143
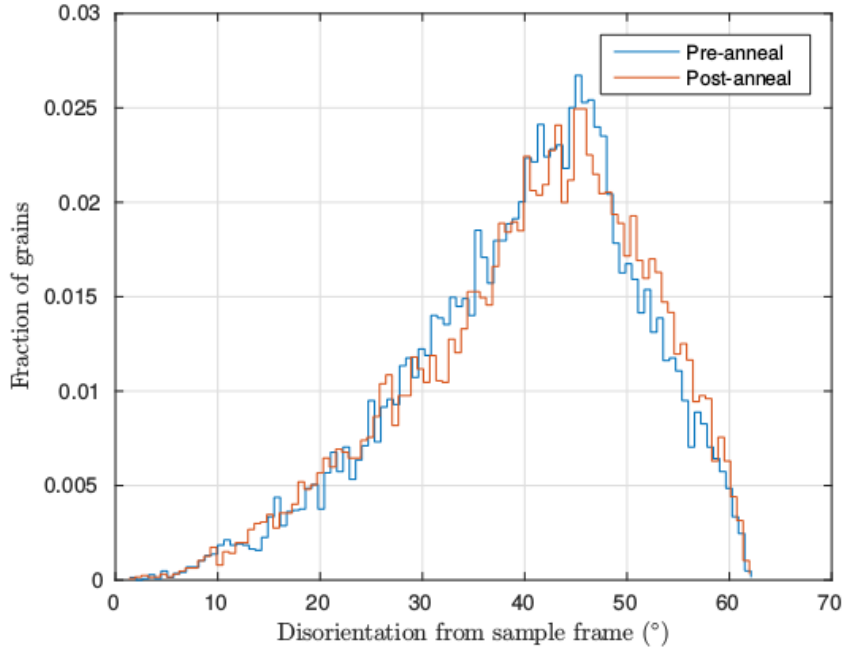
Figure 6.5: Distributions of the angle of disorientation of the grain lattices form the sample frame, before and after anneal. In both cases the distribution is shown to follow the Mackenzie distribution.

We then describe qualitatively the crystallographic texture of the grains in the sample. The distributions of grain disorientations are shown in Figure 6.5 and are seen to follow the Mackenzie distribution characteristic of random orientations [86, 87]. For each anneal state, we plot the pole figures of the $\langle 100 \rangle$ crystal axes corresponding to each grain orientation in Figure 6.6. We see that for both anneal states there is no significant localization of the density of the $\langle 100 \rangle$ poles in both the pre- and post-anneal states. We also address the issue of 'shape texture' of the grains, specifically their elongation with respect to the rolling direction, compared before and after anneal. We do this by computing the moment of inertia tensor $\mathcal{I}$ of the Cartesian sample points $\boldsymbol{r} = [x_0 \ x_1 \ x_2]^T$ of each grain:

$$\mathcal{I}_{ij} = \begin{cases} \int_V d^3r \ \rho(\boldsymbol{r}) \left(r^2 - x_i^2 \right) & \text{If } i = j \\ -\int_V d^3r \ \rho(\boldsymbol{r}) x_i x_j & \text{If } i \neq j \end{cases} \tag{6.2}$$

where $\rho(\boldsymbol{r})$ is the (uniform) mass density of the grain. In the case of a discretized grain, the integral is replaced with a summation with the density being normalized to 1. $\mathcal{I}$ is a symmetric tensor with non-negative eigenvalues whose physical significance is the mass distribution of the grain from the principal axes. These axes roughly correspond to axes of symmetry of the grain and are indicative of directions of elongation or shortening. We see in Figure 6.7 that the pre-anneal state exhibits a preferential
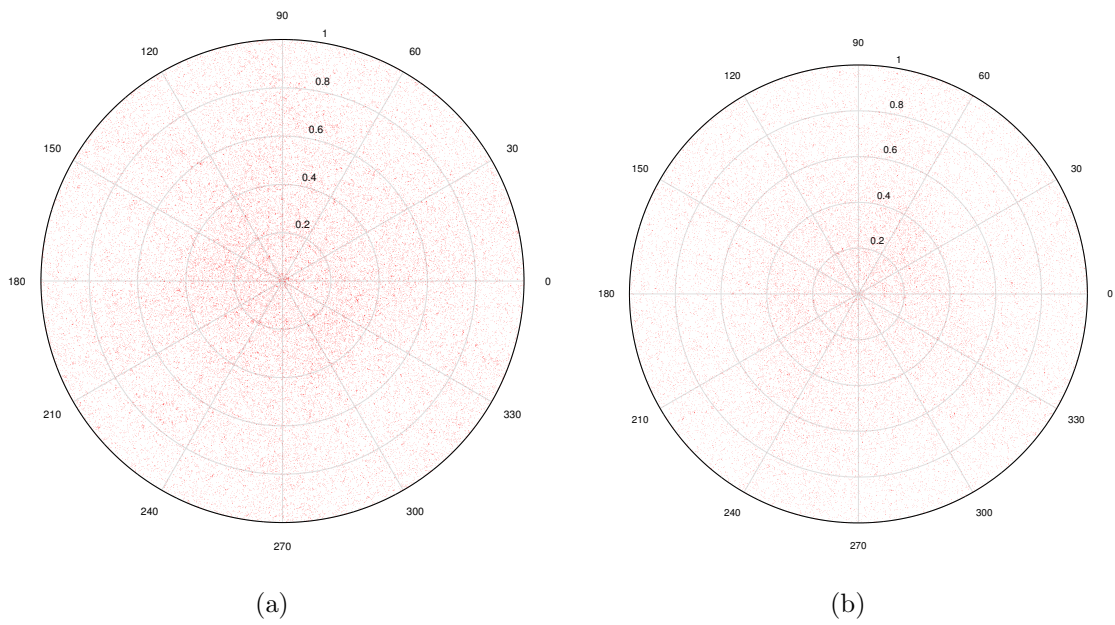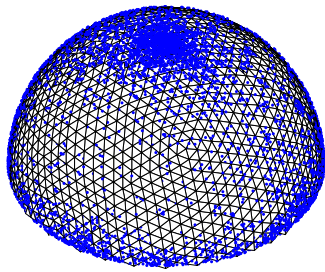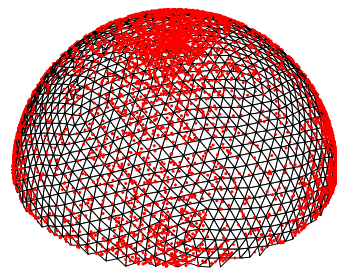
103

Figure 6.6: Pole figure plots of the $\langle 100 \rangle$ crystal axes of each grain, before anneal **(a)**, after anneal **(b)**. The rolling direction emerges from the plane of the figure.

Figure 6.7: Projections of the principal axes of the inertia tensor $\mathcal{I}$ of the grains on to the upper hemisphere, before anneal **(a)** and after anneal **(b)**. The rolling direction is along the Z-axis in both cases.
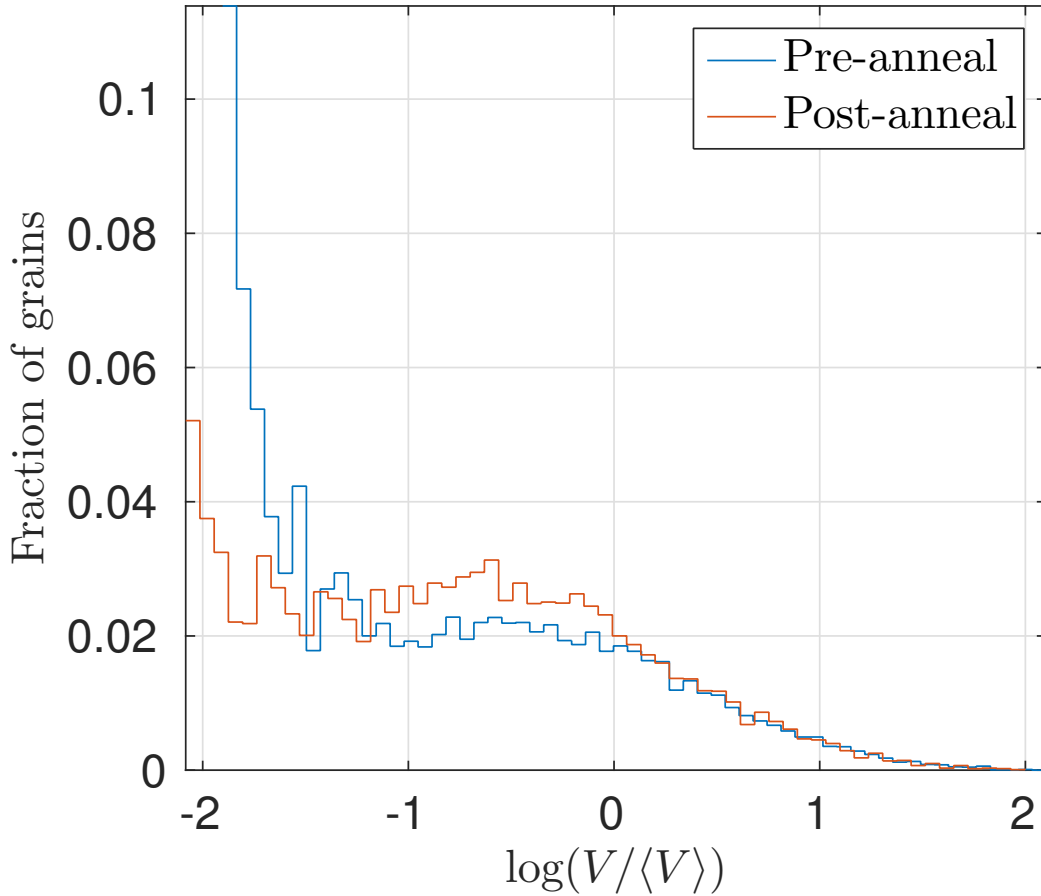
Figure 6.8: Grain volume distributions of α-iron, with the mean volumes given in Table 6.2.

elongation or flattening along the rolling direction, as evidenced by the high density of poles of the grain principal axes. We note that from this diagram alone one cannot tell whether the grains are flattened or elongated along the rolling direction; however, we note that this is somewhat dispersed in the post-anneal state, indicative of the grains being more isotropic. Figure 6.8 shows the distributions of grain volumes.

Table 6.3: List of CSL misorientations for BCC crystals whose GBCDs were queried from the iron sample.

Figure label	Σ	Misorientation angle ($°$)	Misorientation axis
6.9	3	60.0	$\langle 111 \rangle$
6.10	$3b$	19.5	$\langle 100 \rangle$
6.11	5	36.9	$\langle 100 \rangle$
6.12	9	38.9	$\langle 110 \rangle$
6.13	11	50.5	$\langle 110 \rangle$
6.14	$13a$	22.6	$\langle 100 \rangle$
6.15	$17a$	28.1	$\langle 100 \rangle$
6.16	$19a$	26.5	$\langle 110 \rangle$
6.17	$21a$	21.8	$\langle 111 \rangle$

(a) Pre-anneal   (b) Post-anneal
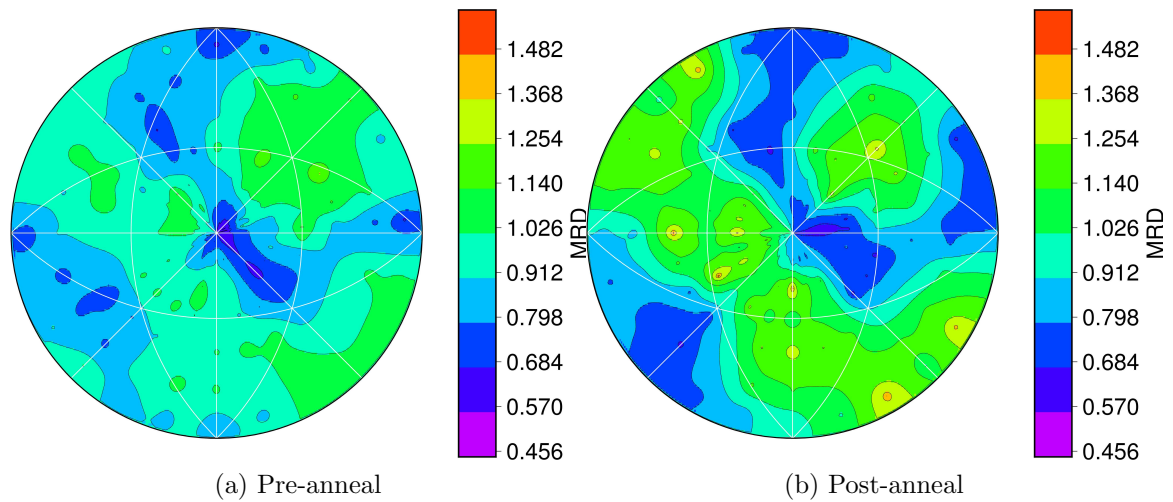
Figure 6.9: $\Sigma 3$ GBCD inverse pole figures

(a) Pre-anneal

(b) Post-anneal

Figure 6.10: Σ3b GBCD inverse pole figures

(a) Pre-anneal

(b) Post-anneal

Figure 6.11: Σ5 GBCD inverse pole figures

(a) Pre-anneal   (b) Post-anneal

Figure 6.12: Σ9 GBCD inverse pole figures

(a) Pre-anneal   (b) Post-anneal

Figure 6.13: Σ11 GBCD inverse pole figures

(a) Pre-anneal

(b) Post-anneal

Figure 6.14: Σ13a GBCD inverse pole figures

(a) Pre-anneal

(b) Post-anneal

Figure 6.15: Σ17a GBCD inverse pole figures

(a) Pre-anneal

(b) Post-anneal

Figure 6.16: Σ19a GBCD inverse pole figures

(a) Pre-anneal

(b) Post-anneal
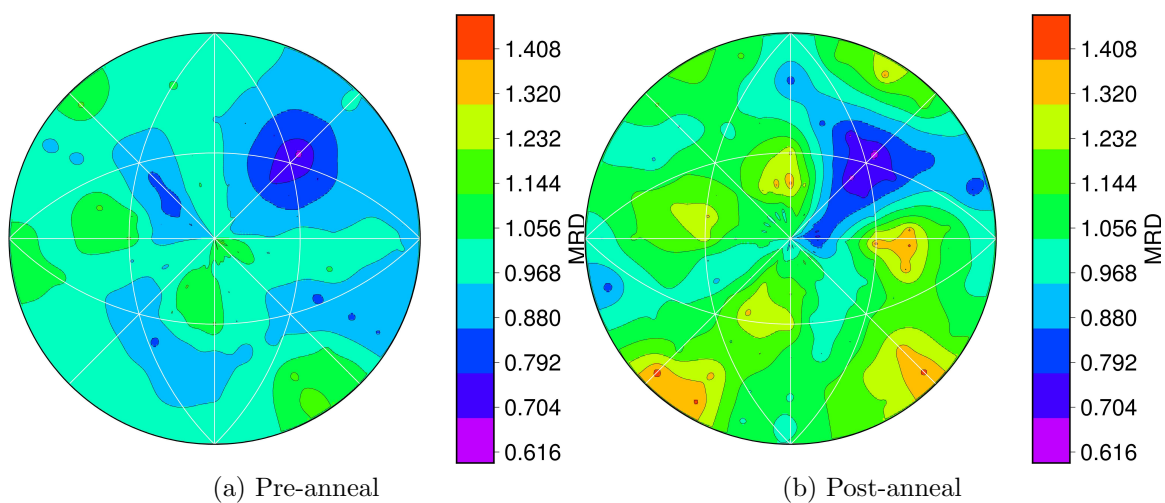
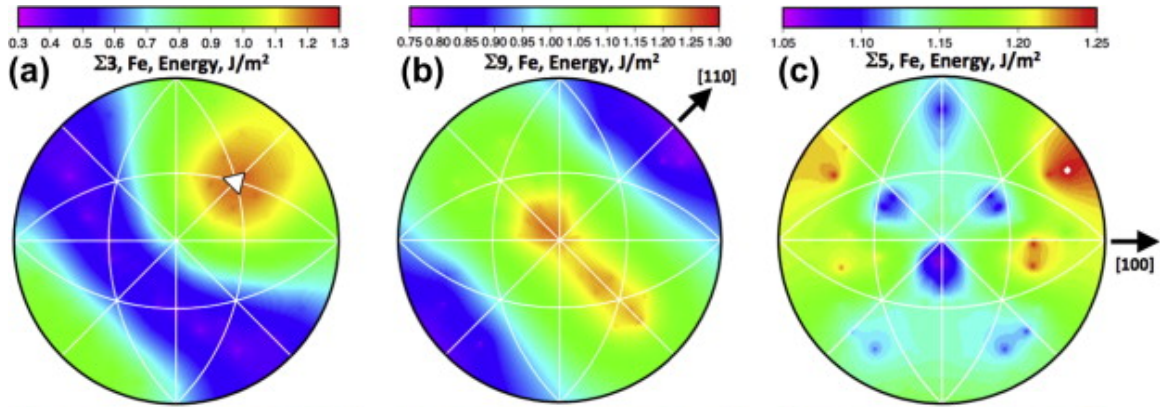Figure 6.17: Σ21a GBCD inverse pole figures

Figure 6.18: GBED for select α-iron CSLs

As a further characterization of the sample we compute parts of the 5 parameter the grain boundary character distribution (GBCD) for select misorientations in which a subset of the atomic positions overlap. The set of these atomic positions form a Bravais lattice by themselves, the so-called 'coincidence site lattice' (CSL) and are characterized by their so-called Σ-number, which is the volume density of overlapping atomic positions. CSL configurations are of special importance in microstructural materials science since the associated grain boundaries in general display special physical properties like low energy and mobility. The GBCD for all grain boundaries of a given misorientation is simply the distribution of boundary area in the space of the local grain boundary normal *i.e.* the remaining two grain boundary descriptors. GBCDs are usually expressed in terms of multiples of a random distribution (MRD) and are plotted on pole figures as stereographic projections. GBCD pole figures for select misorientations (Table 6.3) are shown in Figures 6.9 through 6.17. The relative number and area fractions of the types of grain boundaries in Table 6.3 are shown in Figure 6.19. The GBCDs for $\Sigma 3$, $\Sigma 5$ and $\Sigma 9$ can be compared to the grain boundary energy distributions (GBED) (Figure 6.18) of these CSL misorientations obtained from molecular dynamics simulations [32].

6.3 Volume registration

In this section we describe the procedure of alignment of the pre- and post-anneal volumes. This is a necessary step prior to being able to track microstructural features common to the volumes. There exist many sophisticated methods of image registration based on relative intensity minimization, using control points or manual/automated feature selection. We adopt the simpler two-step method described in Chapter 3, Section 3.3 owing to the specific manner in which the sample was mounted using a rotary clamp (described in Chapter 2). To briefly reiterate,

1. A two-dimensional rigid body transformation (a translation of the centroid fol-
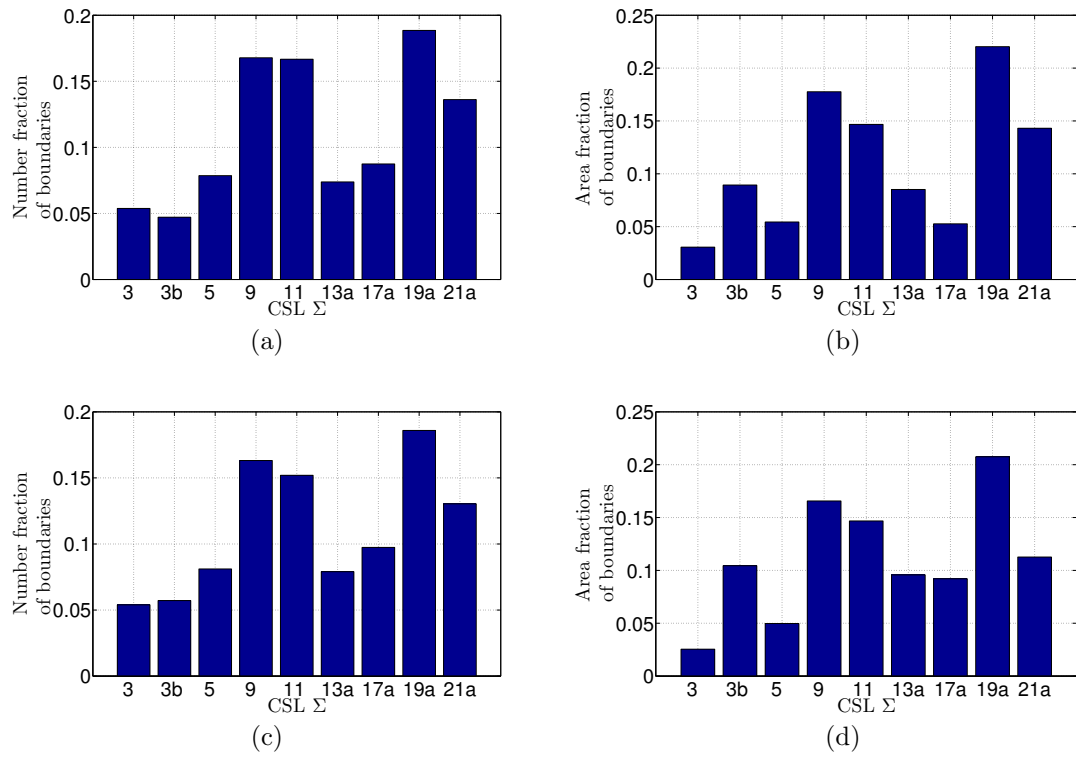
Figure 6.19: Number fractions of grain boundaries for select CSL disorientations: **Left**: Number fraction of boundaries, **Right**: Area fraction of boundaries, **Top**: pre-anneal volume, **Bottom**: post-anneal volume.
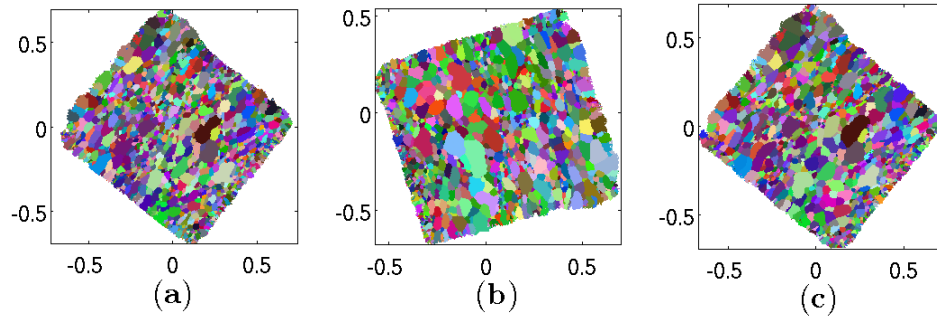
Figure 6.20: Single layer registration by a rigid body transformation: a reconstructed layer of the pre-anneal volume **(a)**, the corresponding layer in the post anneal volume **(b)** and the same layer rotated and translated to overlap the pre-anneal layer **(c)**.

lowed by rotation about it) is determined from the alignment of corresponding layers in the pre- and post-anneal images volumes. This transformation is applied to every layer in the sample, effectively transforming the entire volume identically to the single layer.

2. Then a single grain is chosen that is present in both samples and the volumes are rotated in three dimensions such that the grain has the same orientation in both samples.

We assert that this two-step process is sufficient for registration to within the experimental resolution of nf-HEDM.

In the first of these two steps the layer of choice that dictates the rigid body transformation of the entire volume, was chosen to be in the middle of the overlapping region of the two volumes. The figure of merit of in-plane alignment was chosen to be the number of overlapping 'fit' voxels (*i.e.* determined by the reconstruction software as being inside the bulk of the material). The result of the first of these two steps is shown in Figure 6.20. In the second step, a set of 3261 grains was identified in both volumes and the entire (rigid body transformed) post-anneal volume was reoriented in order to bring the lattice orientations of each of these grains in turn into coincidence. The configuration for which the aggregate misorientation of the 3261 grains was the minimum, was chosen as the final alignment of the post-anneal volume. The distribution of misorientation between corresponding grain versions before and after the optimal grain-based three-dimensional rotation is shown in Figure 6.21. We see that the misorientation angles lie within the experimental angular resolution of $\sim 0.15°$.
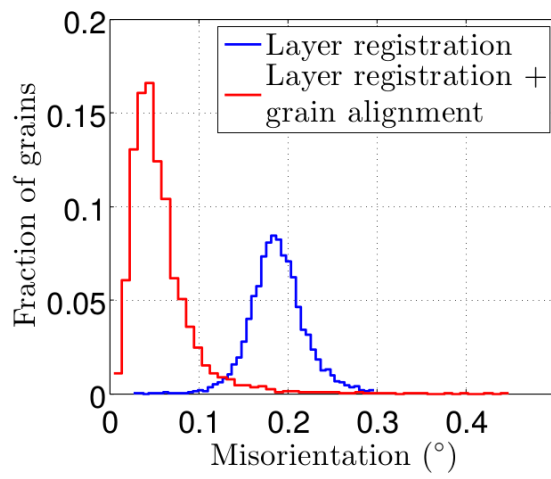
114

Figure 6.21: Distribution of misorientation in corresponding grain lattice prior to and after the three-dimensional rotation.

6.4 Grain and boundary tracking

The registration of the pre- and post-anneal volumes permits us to directly track grains and their boundaries through the anneal process. We present in this section results that are common to sets of grain boundaries that were identified in both volumes. After the crucial step of volume alignment described in Section 6.3, grains present in both volumes were identified by searching for overlapping regions of equal orientation (up to a 2° tolerance). This resulted in a total of 3261 grains in the post-anneal volume that were determined to overlap at least partially in spatial extent with their counterparts in the pre-anneal volume. Some of these grains are shown in Figure 6.22, whose surfaces were smoothed with hierarchical smoothing (Chapter 4). Also shown in Figure 6.23 are examples of boundaries that were tracked through the anneal state and their inferred motion through the optimal transport algorithm developed in Chapter 5, Section 5.6.

With the ability to track boundary motion, we are in a position to test for the influence of interface geometry on boundary migration. We do this by determining the statistical correlation coefficient of the local normal velocity $v_n \equiv \boldsymbol{v} \cdot \hat{\boldsymbol{n}}$ of a grain boundary with the estimated mean curvature κ_m at that point (computed with a nearest neighbor connectivity algorithm [88]). The correlation coefficient for a single grain boundary is given by:

$$\mathrm{Corr}(v_n, \kappa_m) = \frac{1}{N} \sum_{i=1}^{N} \frac{\left(v_n^{(i)} - \langle v_n^{(i)} \rangle\right) \left(\kappa_m^{(i)} - \langle \kappa_m^{(i)} \rangle\right)}{\sigma_{v_n}^{(i)} \sigma_{\kappa_m}^{(i)}} \tag{6.3}$$

where $\langle x \rangle$ and σ_x denote the mean and standard deviation of x respectively, and the sum is taken over the triangular mesh elements that constitute the boundary. We have $\mathrm{Corr}(v_n, \kappa_m) \in [-1, 1]$. Prior to computing this correlation, we briefly review the conventions for boundary inclinations and curvature. Although curvature is a well-defined local property of a curve in 2D or a surface in 3D, its sign depends on the local inclination $\hat{\boldsymbol{n}}$. In the context of closed curves and surfaces (such as grains in 2D and 3D), $\hat{\boldsymbol{n}}$ is taken to be such that its projection in the radially outward direction from the grain centroid is positive. Having set the convention for $\hat{\boldsymbol{n}}$, the sign of the curvature depends on the sense in which $\hat{\boldsymbol{n}}$ changes as one traverses the curve, as seen in Figure 6.24. This 2D visualization is generalized to surfaces in 3D by considering the sense of change in $\hat{\boldsymbol{n}}$ as one traverses the surface along two mutually perpendicular directions given by the eigenvectors of the local shape operator. The eigenvalues of the shape operator are curvatures in these principal directions. The quantity of importance in grain boundary dynamics, the mean curvature κ_m (encountered in Chapter 5), is the average of these two eigenvalues. Since the correlation function changes sign when one of its input random variables changes sign, *i.e.* $\mathrm{Corr}(-a, b) = \mathrm{Corr}(a, -b) = -\mathrm{Corr}(a, b)$, it is easily shown that it remains unchanged under a sign
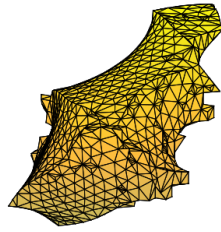
(a)
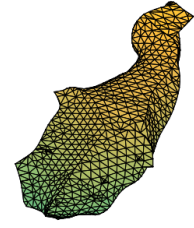
(b)
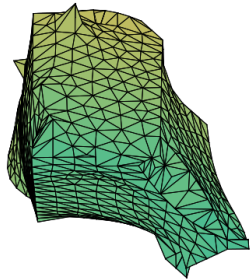
(c)
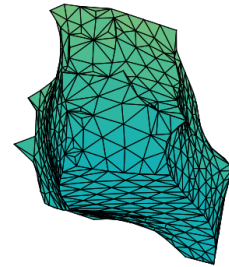
(d)
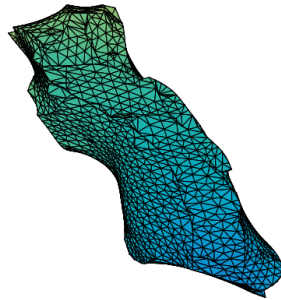
(e)
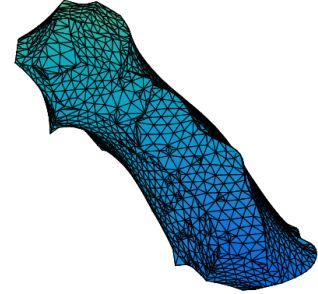
(f)
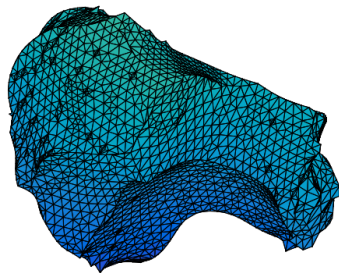
(g)
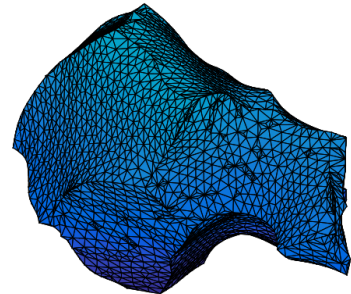
(h)

Figure 6.22: Images of select tracked grains before anneal (left column) and after anneal (right column).

(a)

(b)
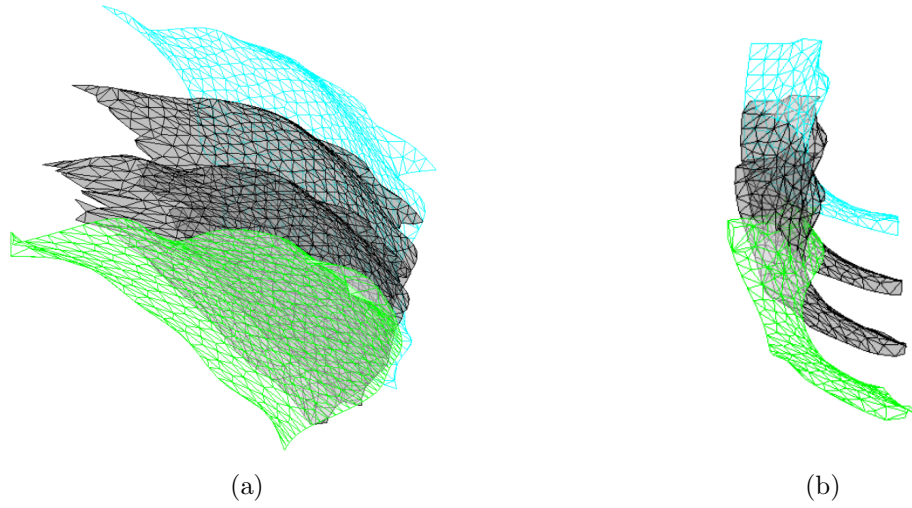
Figure 6.23: Select grain boundaries identified in both microstructure images, with their intermediate states during the annealing process inferred with the optimal transport computation. The cyan boundaries are the pre-anneal boundaries, green are from the post-anneal volume and the translucent gray ones are intermediate.

(a)

(b)
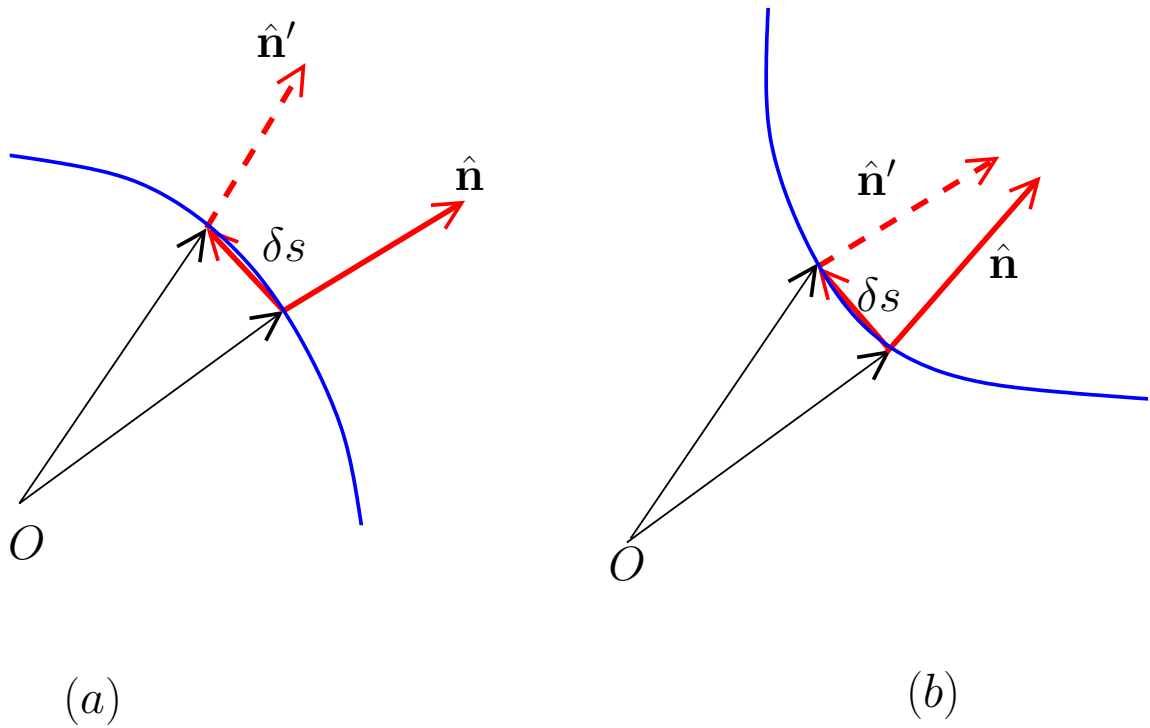
Figure 6.24: **(a)** positive curvature, **(b)** negative curvature.

change of $\hat{\boldsymbol{n}}$ (which physically corresponds to choosing one or the other grain centroid associated with the grain boundary):

$$\hat{\boldsymbol{n}} \longrightarrow -\hat{\boldsymbol{n}}$$
$$\Longrightarrow \text{Corr}(v_n, \kappa_m) \longrightarrow \text{Corr}(-v_n, -\kappa_m)$$
$$= \text{Corr}(v_n, \kappa_m)$$

Once the convention for $\hat{\boldsymbol{n}}$ was set consistent with the sign of κ_m over each grain boundary, the computation of the correlation coefficient was straightforward.

Shown in Figure 6.25 is the correlation coefficient for the tracked boundaries (numbering to about 15500). The computation was restricted to those grain boundary patches whose curvature lay in the range $|\kappa_m| \leq 1/3$ corresponding to a radius of curvature of 3μm (which was approximately the chosen size of the 3D voxel) or greater. We list the possible sources of error in the computation of the correlation coefficient:

- The errors introduced due to the estimation of curvature [88] by fitting a surface locally to a quadratic curve.

- The inaccurate estimate of the true instantaneous boundary velocity due to over-annealing of the sample.

6.5   Energy-mobility proof-of-concept

As mentioned in Chapter 5, a major goal of this thesis is to eventually be able to perform more sophisticated computations on microstructure data in order to extract the relevant parameters that determine boundary migration. The task of establishing numerically the link between measurable quantities like grain boundary geometry, topology and transport (residing in 3D Cartesian space) and the thermodynamic functions that determine said transport (residing in a crystallographically compact subspace of $SO(3)$) is a highly nontrivial inverse problem. As has already been demonstrated in Chapter 5, if one were to consider differential migration of the boundaries in a network, this inverse problem can be linearized (specifically, as a generalized eigenvalue problem) for which there exist known methods of solution. This section presents proof-of-concept validations of the numerical machinery developed in Chapter 5 for certain synthetic data sets that mimic grain boundaries in a sample. We follow the general procedure summarized in Figure 6.26, in which we first generate an ensemble of interfaces and evolve them according to a known energy density γ and mobility μ, then apply the formalism developed in Chapter 5 in order to re-obtain the energy and mobility, or at least quantities proportional thereto.
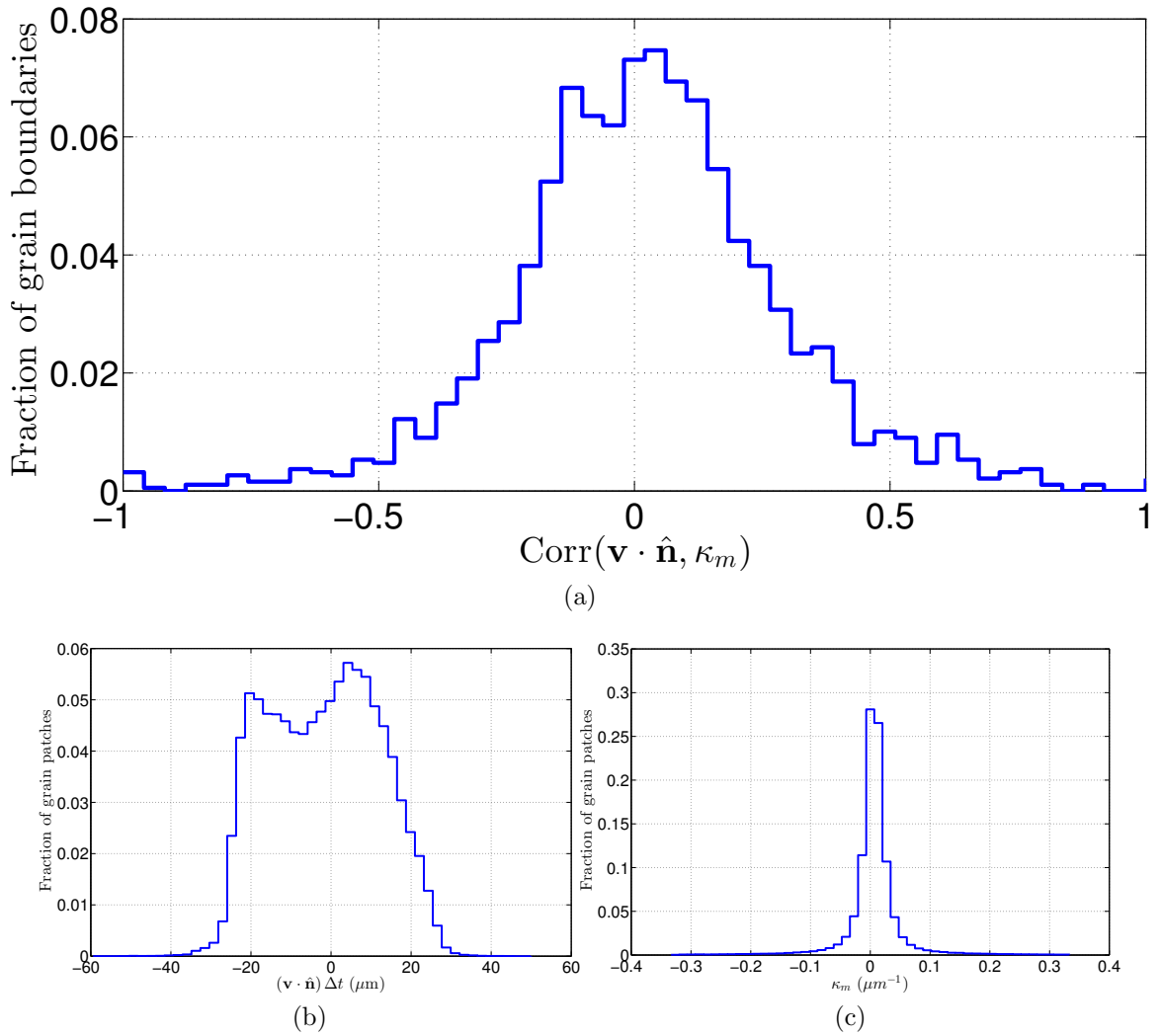
Figure 6.25: **(a)** Correlation coefficient between local normal velocity $\boldsymbol{v}\cdot\hat{\boldsymbol{n}}$ and mean curvature κ_m, computed for different tracked boundaries, **(b)** distribution of local $\boldsymbol{v}\cdot\hat{\boldsymbol{n}}$, **(c)** distribution of local κ_m.
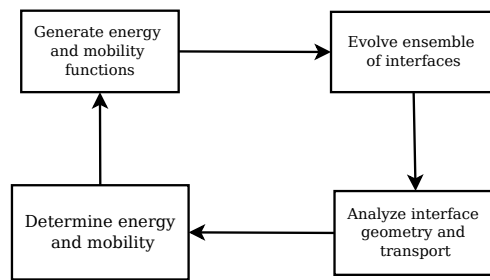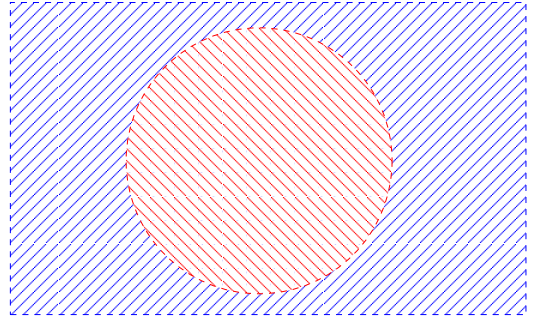
Figure 6.26: Full-circle sequence of steps for validation of the coarsening theory.

Figure 6.27: Schematic of an imaginary spherical grain which contains, by definition, all possible boundary inclinations for a given crystallographic misorientation.

Given all the grain boundaries in a volume of a particular misorientation (and all its equivalents), we require that the corresponding local boundary inclinations populate the chosen symmetry-reduced subdomain of S^2 with sufficient uniformity (see Section 5.5.4). The easiest way to synthesize such data is to imagine a single mesoscopically spherical grain in a polycrystalline material whose interior corresponds to one orientation and the exterior to another (Figure 6.27), such that the misorientation between the interior and exterior is the desired one. The spherical interface thus represents literally all available inclinations of the grain boundary area, with uniform distribution. This will be our prototypical system upon we base our validations of the numerical theory. Since the spherical grain boundary has no terminal features typical of real grain boundaries (*i.e.* junction lines and points), we create an ensemble of imaginary grain boundaries by sectioning the spherical grain boundary into smaller facets and pretending that each one is an independent grain boundary from a volume (Figure 6.28). This construction elegantly satisfies the requirement that the total available grain boundary area uniformly populate the chosen subdomain of S^2 as delineated by $\langle 100 \rangle$, $\langle 110 \rangle$ and $\langle 111 \rangle$ (see Section 5.5.4).

One cautionary point is that *the reduction of all these available unit normals to the chosen crystallographic subdomain described in Section 5.5.4 implies transforming the misorientation as well by the appropriate symmetry operator, in order to preserve the fundamental nature of the grain boundary in an atomistic sense.* Operationally this does not make a difference to our analysis, because the misorientation is never actually used anywhere in the computation, but it is something important to be kept in mind.

We now go on to detail two cases in our validation exercise, which differ in the nature of the assumed interfacial energy density γ. The first case harks back to John von Neumann's original treatment of soap bubble films and the second concerns a more nontrivial energy profile.

(a)   (b)
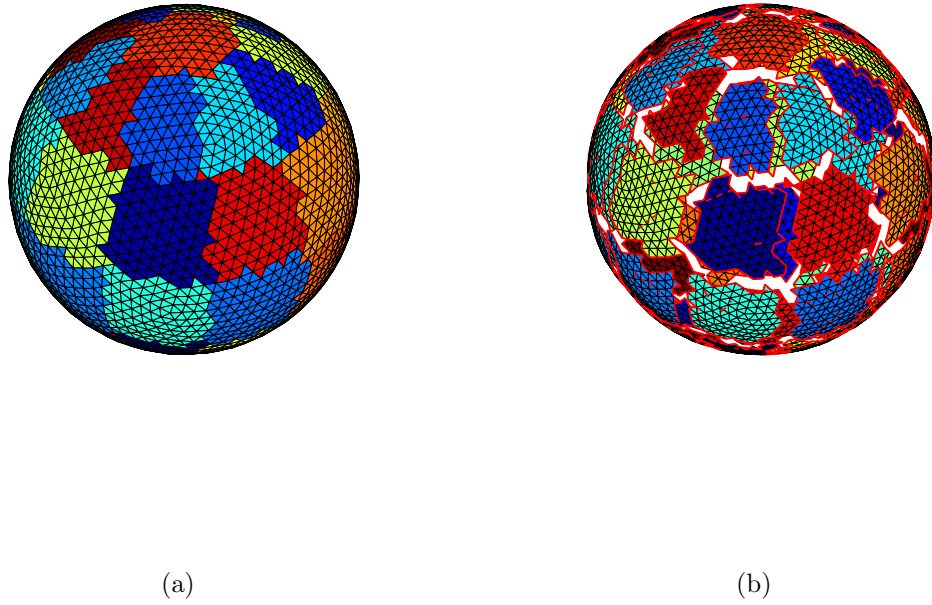
Figure 6.28: Grain boundary ensemble spanning all possible boundary inclinations generated by segmenting a sphere and treating the isolated pieces as grain boundaries, which now have features analogous to triple lines (edges) and quad points (terminal points of edges). **(a)** shows the segmentation of a meshed sphere into imagined grain boundaries, **(b)** shows the same, exploded radially to highlight the perimeter relations between the constituent patches.

6.5.1 von Neumann isotropy in the energy and mobility

We first address the case of constant energy and mobility ($\gamma(\hat{\boldsymbol{n}}) = \gamma_0$ and $\mu(\hat{\boldsymbol{n}}) = \mu_0$) in Equation (5.20), for the spherical patches described in the previous section. Owing to the fact that $\nabla\gamma(\hat{\boldsymbol{n}}) = 0 \; \forall \hat{\boldsymbol{n}}$, there is no in-plane distortion of any of the grain boundaries and the only migration is in the radial direction ($\boldsymbol{v} = v\hat{\boldsymbol{n}}$). Thus along the edges of any interface, we have $\boldsymbol{v} \cdot \hat{\boldsymbol{m}} = 0$ and therefore without the perimeter term, Equation (5.20) is simplified to:

$$\frac{d}{dt}\left(\gamma_0 r^2 \Omega\right) = -r^2\Omega\frac{v^2}{\mu_0}$$

$$2rv\gamma_0\Omega = -r^2\Omega\frac{v^2}{\mu_0} \qquad\qquad (\because \frac{dr}{dt} = v)$$

$$\implies v = -2\kappa\gamma_0\mu_0 \qquad\qquad\qquad (6.4)$$

where Ω is the solid angle subtended by the boundary, $\kappa \equiv 1/r$ is the constant mean curvature. Equation (6.4) is precisely the result of von Neumann's 1952 work [63]. This equation simultaneously demonstrates that for isotropic physics, grain boundaries migrate towards their centers of curvature (evidenced by the negative sign) and that the velocity of migration is proportional to the interfacial energy density, mobility (sometimes considered together as the 'reduced mobility' $\gamma_0\mu_0$) and the local mean curvature. We seek to establish in this subsection that radially inward von Neumann migration of spherical (synthetic) grain boundaries does indeed return constant γ and μ values for all $\hat{\boldsymbol{n}}$. This is the simplest check that can be performed on the numerical technique developed in Chapter 5.

We choose for simplicity a value of 1 for r and v in arbitrary units which gives: $\gamma_0\mu_0 = 1/2$ which mean we should expect the interfacial energy density to be half the inverse mobility. This is coupled with the normalization constraint specified in Equation (5.27), specifically $\mathbf{x}^T W \mathbf{x} = 1$ where $\mathbf{x} = [\gamma_0 \; \gamma_0 \; \ldots \; \gamma_0 \; 1/\mu_0 \; 1/\mu_0 \; \ldots \; 1/\mu_0]^T$. The weighting matrix W is of the form:

$$W = \begin{bmatrix} W_0 & 0 \\ 0 & W_0 \end{bmatrix} \qquad\qquad (6.5)$$

where W_0 is a diagonal matrix whose diagonal elements are the (normalized) areas of the triangular elements in Figure 5.4. Shown in Figure 6.29 is the computed result compared against the theoretical value for the case of $\gamma_0 = 1/2\mu_0$. Figure 6.30 shows another representation of the same information, namely the energy and mobility fields plotted on the relevant subdomain of S^2, which is suitable for cubic symmetry.

We thus establish the ability of the energy-mobility numerical machinery to solve the simplest problem in its class, that of isotropic energy and mobility. We study its performance next in a specific case of anisotropy in the energy density.

124
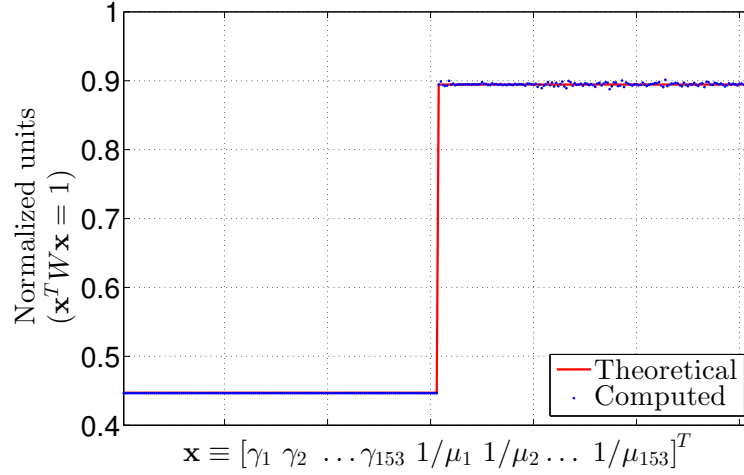
Figure 6.29: Plot of the solution vector $\mathbf{x}$ for the case of $\gamma(\hat{\boldsymbol{n}}) = \gamma_0$ and $\mu(\hat{\boldsymbol{n}}) = \mu_0$, when the radius r of the evolved sphere and its local normal velocity v are both set to 1 (arbitrary physical units). In this case, $\gamma_0 = 1/2\mu_0 \implies \gamma_0 = \chi_0/2$
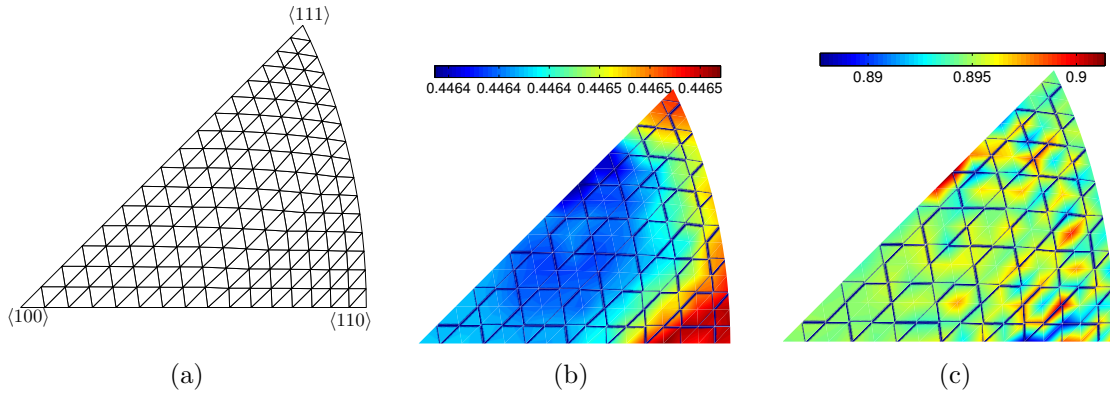
Figure 6.30: **(a)** Mesh on the symmetry-reduced sub-region of grain boundary normals, **(b)** interfacial energy density $\gamma(\hat{\boldsymbol{n}})$ re-computed from isotropic migration, **(c)** inverse mobility $\chi(\hat{\boldsymbol{n}}) = 1/\mu(\hat{\boldsymbol{n}})$ re-computed from isotropic migration.

125

6.5.2 Energy minimum about a symmetry axis

We now perform the same full-circle analysis described in Section 6.5.1, but for an energy/mobility profile that is not a constant function of $\hat{\boldsymbol{n}}$. This is an inconvenient truth about polycrystalline materials as opposed to other interface network systems like soap films, one which instantly complicates the dynamics and therefore the kinematics of moving interfaces. Owing to the fact that surface torsion can no longer be ignored ($\nabla\gamma \neq 0$), we can no longer remain content with the assumption of migration towards the grain boundary center of curvature. We are now faced with the *forward* problem of determining the local transport of each 'boundary' in our synthetic ensemble according to an assumed $\gamma(\hat{\boldsymbol{n}})$ and $\mu(\hat{\boldsymbol{n}})$ before we can work backwards and recover numerically the γ and μ as we did in Section 6.5.1.

Fortunately, this has already been addressed in the numerical formalism developed in Chapter 5, Section 5.5.1. We simply use Equation (5.25) with analytical expressions for $\gamma(\hat{\boldsymbol{n}})$ and $\mu(\hat{\boldsymbol{n}})$ (and therefore $\boldsymbol{\xi}(\hat{\boldsymbol{n}})$ as well) in order to evolve each interface node-by-node for a sufficiently small time interval dt. The ensemble is generated in the same manner as in the previous section: segmentation of the surface of a triangulated sphere with each individual patch or segment considered as an independent grain boundary (Figure 6.28).

We now turn our attention to the nature of the energy density function. As already stated, we choose for simplicity the grain misorientation of 60° about $\langle 111 \rangle$, which is a twist misorientation. This permits us to generate an energy density function $\gamma(\hat{\boldsymbol{n}})$ that adheres to the cubic crystal symmetry. In other words, If S_i is a cubic symmetry operator, then $\gamma(S_i\hat{\boldsymbol{n}}) = \gamma(\hat{\boldsymbol{n}})$ and therefore use the highly compact subregion of S^2 delineated by [100], [110] and [111] and already described in Figure 5.9. We note that this is in general *not* true for all misorientations, owing to the fact that the symmetry operators associated with one side of a grain boundary are not the same as those on the other side. Given a certain grain misorientation, a generalized prescription of determining the 'fundamental zone' on the surface of the unit sphere is given by Patala *et al.* [80] and must be adhered to in order to analyze grain boundaries with different misorientations.

We choose a *differentiable* field that has a minimum at all the crystallographic $\langle 111 \rangle$. Strictly, the assumption of differentiability flies in the face of what is known about the interfacial energy density for cubic materials [33], namely that these minima are actually cusps where the gradient $\nabla\gamma$ is multiply defined [69, 70]. We ignore this condition in favor of numerical tractability.
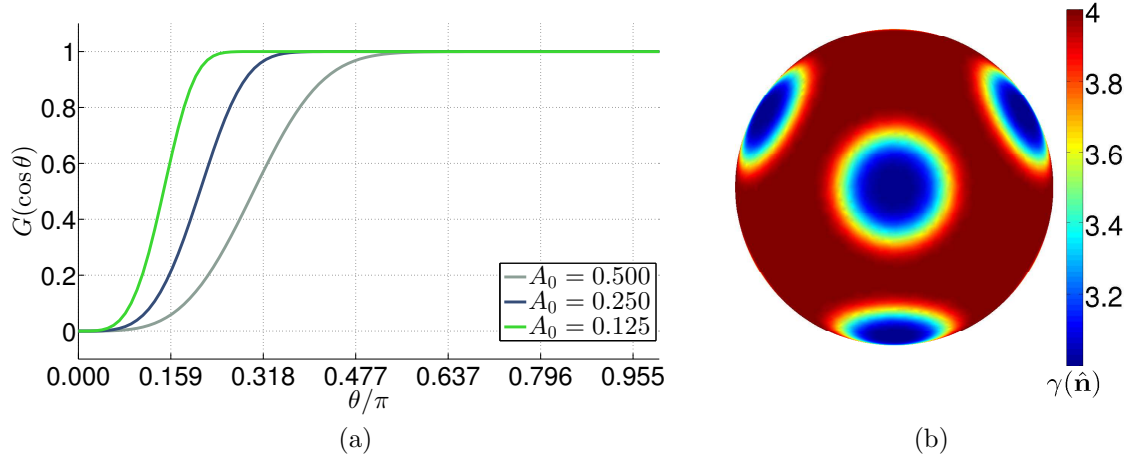
Figure 6.31: **(a)** The function G plotted as a function of angular separation θ from a minimum at 0; **(b)** the energy density field $\gamma(\hat{\boldsymbol{n}})$ with minima at the crystallographic $\langle 111 \rangle$, and a baseline value of 3.0.

We define the interfacial energy density in terms of an analytic function G of $\hat{\boldsymbol{n}}$ that exhibits a minimum at a fixed point $\hat{\boldsymbol{n}}_0$:

$$\gamma(\hat{\boldsymbol{n}}) = \prod_{i=1}^{N} G(\hat{\boldsymbol{n}} \cdot \hat{\boldsymbol{n}}_i) \tag{6.6}$$

$$\text{where } G(x) = 1 - \exp\left[-\left(\frac{x-1}{A_0} \right)^2 \right]$$

Here the $\hat{\boldsymbol{n}}_i$ denote the $\langle 111 \rangle$ axes and A_0 is related to the width of the energy density well. The quantity $\hat{\boldsymbol{n}} \cdot \hat{\boldsymbol{n}}_0 - 1$ measures the angular separation of the query point $\hat{\boldsymbol{n}}$ from the local minimum $\hat{\boldsymbol{n}}_0$. Shown in Figure 6.31 is the function G that dictates the nature of the differentiable function with a minimum, as well as the resultant scalar field when this minimum is present at each of the crystallographic $\langle 111 \rangle$. The function G can be modified to reflect different behaviors. For example, a true cusp at $\hat{\boldsymbol{n}}_0$ of estimated width A_0 can be modeled by setting: $G(\hat{\boldsymbol{n}}) = \tanh\left[(\hat{\boldsymbol{n}} \cdot \hat{\boldsymbol{n}}_0 - 1)/A_0 \right]$.

Before presenting the results of the full-circle treatment in the case of the anisotropic energy density field, we describe the actual evolution of the sphere of Figure 6.28 in response to the said field. Under the energy minimization scheme developed in Chapter 5 if there is a variation of the interfacial energy density, we would expect the sphere to distort progressively in time according to the following mechanisms of energy minimization:

- There should be a general bulk shrinking of the sphere since $\gamma(\hat{\boldsymbol{n}})$ is in general

127

an excess and therefore non-negative. This is identical to the radial migration from Section 6.5.1.

- The sphere should now also exhibit local surface torsion as it tries to apportion more and more surface area to the lower energy inclinations.

These physical expectations are fulfilled in Figure 6.32 in which the meshed sphere evolves in response to the anisotropic energy field (mobility was held at a constant value of 1 for simplicity). The flattening of the sphere at the $\langle 111 \rangle$ axes is indicative of the lower-energy boundary inclination becoming more prominent. Less dramatic but also observable is the bulk shrinking of the sphere radius as can be seen by comparing the sizes of the sphere in **(b)** and **(i)**. We caution, however, that while the basic physical behavior is as expected, the sequence of images in Figure 6.32 is exaggerated in time for the viewer's benefit and as such is not strictly a differential process. True evolution for a finite time interval would involve remeshing the surface to obtain equal-sized mesh elements at each step before the next iteration.

We now present the best result for energy density and mobility obtained for an anisotropic boundary evolution in Figure 6.33. The figure shows the computed parameters γ and μ for the symmetry-reduced subregion of S^2, with the understanding that the same energy and mobility variation is present in all symmetry-equivalent regions of S^2. A discussion of these results is deferred to the concluding section of this thesis.
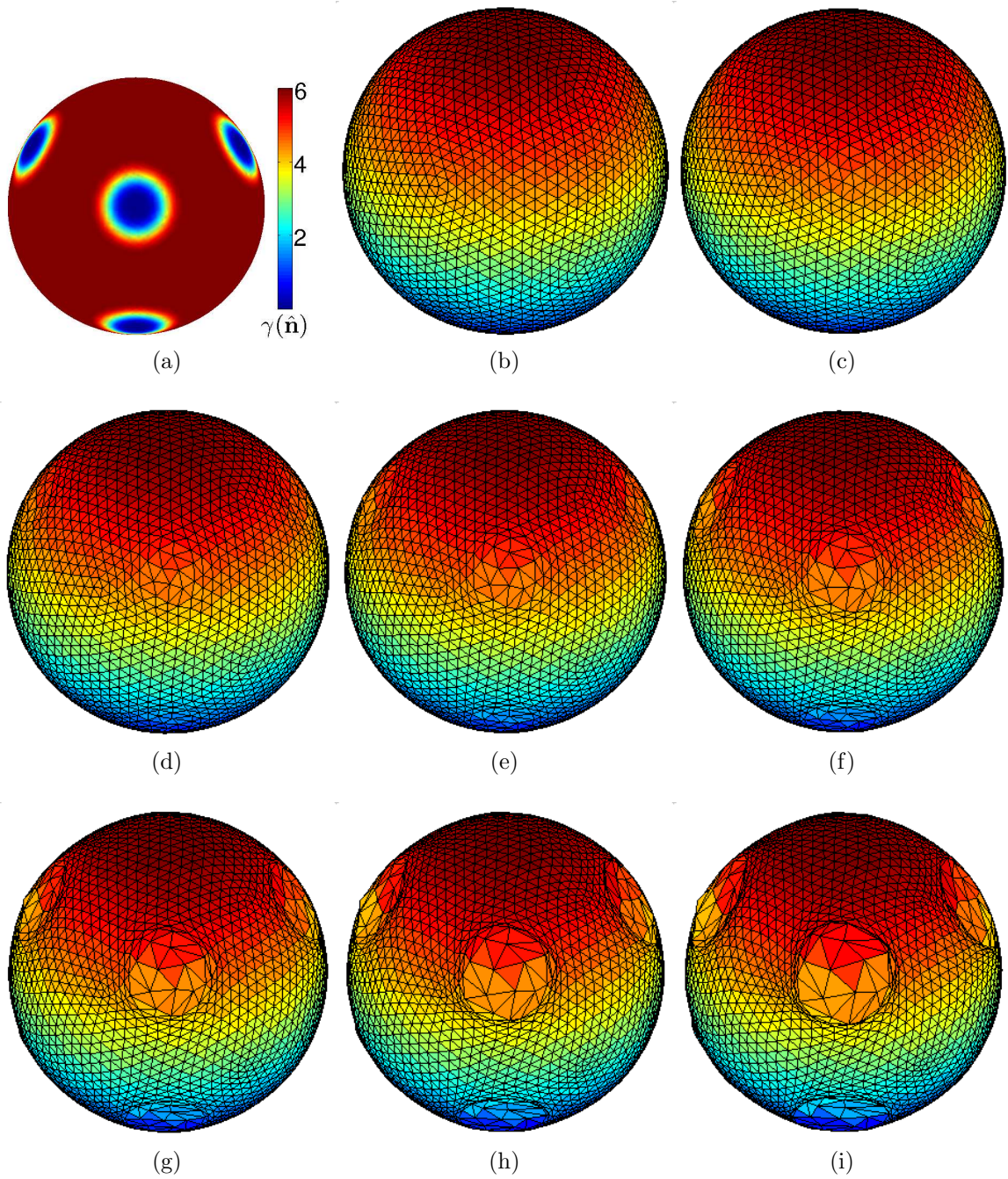
Figure 6.32: **(a)** Energy density used for demonstration of sphere evolution. The mobility was fixed at a constant value of 1. **(b) - (i)** Evolution of the sphere in Figure 6.28 under this energy.
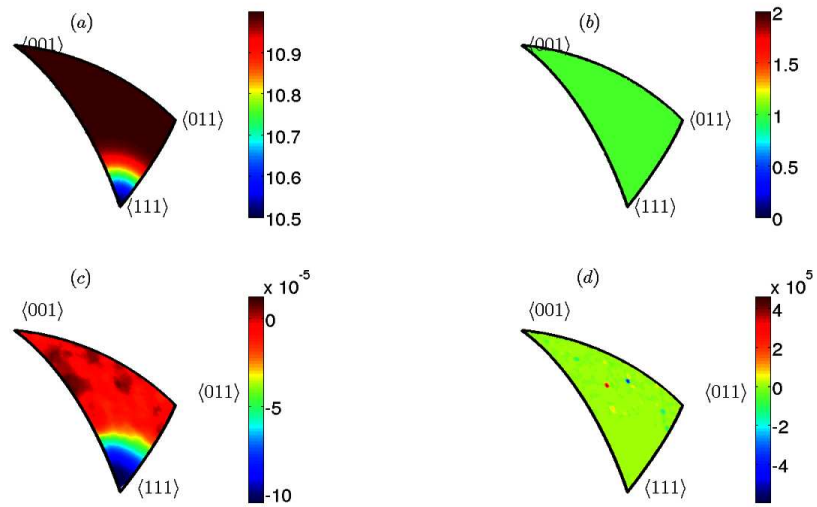
Figure 6.33: **(a)** Theoretical energy density γ in the repeating triangular subregion delineated by the [001], [011] and [111] axes; **(b)** Theoretical mobility μ (constant) in the same region; **(c)** computed energy density, **(d)** computed mobility.

Chapter 7

Conclusions

In this chapter we discuss the experimental and computational results presented in Chapter 6. Our discussion follows the sequence in Chapter 6, starting with a discussion of the microstructural features as seen in the image reconstructions, followed by a lengthier discussion of the bulk material statistics of α-iron determined from the nf-HEDM experiment. This latter discussion covers the following:

- Texture with respect to grain orientation and shape and the ramifications for further statistical computations.

- The qualitative aspects of the grain boundary character distribution for different CSL misorientations and their relation to published results of the distribution of grain boundary energy γ.

- The extent of agreement of the observed grain boundary motion to known models of curvature-driven migration. The possible sources of error are discussed along with arguments supporting the observed results.

7.1   Voids in the imaged microstructure

The original intent of preparing and experimentally measuring a material sample was to eventually obtain real polycrystal data as input for the numerical techniques developed in Chapter 5. The theory upon which these techniques are predicated makes a fundamental assumption about the interfaces in question, namely that they are internal interfaces between grains and not free surfaces. The intersection of a polycrystal interface with a free surface results in grooving in order to achieve thermodynamic equilibrium, a comprehensive analysis of which is outside the scope of this thesis.

An important step in the material preparation was mill-rolling in order to destroy the existing columnar grain structure. Accordingly we sought to minimize the sizes of

the inevitable micro-fractures by rolling the sample to smaller and smaller thicknesses in multiple steps. As already mentioned, the voids in the bulk material resulting from these micro-fractures are characterized in the nf-HEDM maps as a gradual decrease in the confidence metric $\mathcal{C}$ as one traverses the map into the region of the fracture. Since the orientation search algorithm described in Section 3.2 automatically adjusts voxel orientations, the characterization of a low-$\mathcal{C}$ region as a void from nf-HEDM maps alone is anecdotal at best and must be rigorously verified with density mapping techniques such as absorption tomography. The presence of voids is an undesirable consequence of this particular material processing routine and the free surfaces along these voids must be excluded from the list of candidates that are part of the energy/mobility analysis. However, their presence in statistically significant populations may prove useful in studies of recovery and recrystallization tendencies along void peripheries, for which synchrotron imaging techniques such as HEDM and absorption tomography are perfectly suited.

7.2   Material texture

The two main concerns in our attempts to recreate a relatively isotropic grain structure was the residual crystallographic and shape textures of the sample grains due to the mill-rolling. Both these phenomena are a result of the initial microstructure being plastically deformed in a single direction systematically and tend to be offset through the anneal process. From Figure 6.5 the distribution of grain disorientations from the sample frame is seen to follow the Mackenzie distribution characteristic of a random ensemble of orientations for a cubic material, for both anneal states. This is further verified by the $\langle 100 \rangle$ pole figure plots of the grain orientations in Figure 6.6. A sample with significant texture would contain high-density 'clumps' in the pole distributions.

The shape texture, on the other hand, was determined by computing the principal axes of the inertia tensor $\mathcal{I}$ of each grain and plotting their pole figures. It is well known that the principal axes of $\mathcal{I}$ tend to be directed along symmetry axes of the grains. A high density of principal axis poles is indicative of elongation or compression of many grains along a fixed direction. The plot of the principal axis poles over the upper hemispheres in Figure 6.7 shows a relatively higher concentration of poles along the rolling direction and an annulus of poles about the azimuth, with the intermediate space relatively pole-free. This is indicative of prolate grains, which is to be expected upon the rolling of the sample in a fixed direction. The concentration of poles along the rolling direction is seen to be partially dispersed in the post-anneal image, indicative of the grains becoming more spherical.

Thus it is seen that while the anneal cycle partially removed the grain elongation, there was still a directional bias of the principal axes of $\mathcal{I}$ and therefore of the local grain boundary inclinations. We conclude that the generation of an ideal isotropic grain structure through annealing while simultaneously trying to ensure differential grain boundary migration requires a much more sophisticated material processing routine than was implemented here. Consequently, the usage of the grain boundaries of this α-iron sample in the energy/mobility computation of Chapter 5 would have to be done judiciously only after ensuring that the set of eligible grain boundaries sufficiently populates the subregion of S^2 corresponding to the chosen grain boundary disorientation. At the time of writing this thesis, efforts in this direction are underway.

7.3 GBCD and GBED

An important statistical characterization of a grain boundary network in its five-dimensional descriptor space is the relative distribution of grain boundary area in the space of boundary inclinations (the grain boundary character distribution, GBCD), for all sample grain boundaries of a given disorientation. Although in theory one can generate such a distribution for any chosen disorientation, microstructure literature abounds in GBCD plots for measured grain boundaries of a given CSL misorientation. CSL misorientations are associated with special physical characteristics such as markedly lowered boundary energy and mobility [89], on account of their being geometrical idealizations in which a fraction of the atomic positions overlap after disorientation. In this section we summarize the qualitative features of the GBCDs shown in Figures 6.9 through 6.17 and in select cases, compare the results to grain boundary energy distributions (GBEDs) of the α-iron material obtained from molecular statics simulations [32]. The GBCDs were computed with an angular tolerance of 5°.

- The area distribution for most of the plotted GBCDs is seen to remain within 0.45 and 1.92 times the relative distribution of a random orientation ensemble, with the exception of the GBCD of the $\Sigma 13a$ misorientation, which ranges up to ~ 8 MRD (Figure 6.14). This is largely in contrast to the measured GBCDs of ferritic and interstitial-free steel [90, 91], which range from ~ 4 MRD to ~ 20 MRD. One can conclude that the presence of solute elements greatly skews the GBCD by changing the energy landscape.

- In a typical relaxed system and for a given disorientation, one would expect an inverse correlation between the GBCD and GBED (*i.e.* $\gamma(\hat{\boldsymbol{n}})$ as a function of $\hat{\boldsymbol{n}}$). This is observed qualitatively in the GBCDs for $\Sigma 3$, $\Sigma 5$ and $\Sigma 9$ (Figures 6.9, 6.11 and 6.12) when compared to their corresponding GBEDs (Figure 6.18). The notable departure from this tendency is observed in the vicinity of the $\langle 111 \rangle$

inclination of the $\Sigma 3$ disorientation, where the GBCD is seen to be in direct correlation with the computed GBED.

- Between anneal states for these three CSL disorientations, the GBCDs is seen to shift towards the lower energy configuration, again with the exception of the $\langle 111 \rangle$ for $\Sigma 3$. This shift in distribution is to be compared with predictions of steady state GBCDs made from finite element simulations during curvature-driven grain growth [92].

7.4 The driving force of boundary migration

In this section we address the issue of the driving force of grain boundary migration. We describe the historical context and the current state of understanding of the physics of interface motion, along with the difficulties that exist in mathematically modeling these phenomena even in the present day, recalling in the process some of the definitions and ideas elucidated in Chapter 5. We discuss the significant advances in the ability to image boundary migration in two and three dimensions and then argue the case for the results of the correlation analysis presented in Section 6.4.

Since von Neumann and Mullins' simplified model of two-dimensional interface migration [63, 65] based on the assumptions of isotropic surface energy and mechanical equilibrium at boundary junctions, it has been generally accepted that the velocity of boundary motion in 2D is proportional to the local curvature. Through surface experiments, it became possible to measure the effect of impurities, misorientation and the temperature and curvature dependence of migration rate for a variety of simple bicrystal interface geometries like a quarter-loop, half-loop, wedge and planar bicrystal [93, 94, 95]. Experiments designed to determine the curvature dependence of 2D grain boundaries tend to omit the caveat that that two-dimensional grain growth is actually an idealization, and that physical experiments involving surface imaging or thin films have to contend with nontrivial secondary effects like thermal grooving and free surface boundary conditions.

With the advent of modern computers, simulation work in the field of interface migration has exploded. A variety of simple mathematical models were tested such as the Allen-Cahn [96] and time-dependent Landau-Ginzburg equations [97]. Molecular dynamics simulations [98, 99, 100] use different analytical forms for the atomic interactions, while vertex dynamics [101, 102] and phase field simulations [103] are predicated upon a limited dependence of the grain boundary energy on the five-dimensional space of grain boundary descriptors. The difficulty in simulating grain boundary migration in three dimensions with nontrivial dependence of the grain boundary energy and mobility on grain boundary parameters along with the geometric constraints imposed by triple and quadruple junctions is fully appreciated.

Before the era of nondestructive three-dimensional measurements of microstructure, inferences on the local velocity-curvature relation of grain boundaries in three dimensions were predicated on such simplified simulations alone. With such techniques at hand, we are now in a position to observe these phenomena under the full influence of anisotropic energy and mobility as well as the highly complicated effects of the geometric constraints due to junctions. The reconstructed and sufficiently well-aligned α-iron dataset described in this thesis represents the early ability to directly track a statistically significant number of three-dimensional grain boundaries and measure the influence of local curvature on boundary velocities.

We begin by reiterating the possible sources of error in the measurements of boundary geometry and transport that inform the curvature-velocity correlation study.

- The local curvature is estimated by fitting a small set of connected mesh elements to a quadratic surface [88]. Some of the mesh elements returned by the hierarchical smoothing algorithm (Chapter 4), while representative of the true contour of the grain boundary interfaces, tend to be elongated in one direction in favor of another, a fact that inevitably affects the computation of mean curvature.

- The heat treatment may have resulted in some grain boundaries migrating farther than can be managed mathematically by the first-order approximation of migration dynamics.

- Owing to resolution constraints, the candidate grains boundaries ($15, 500$ in number) that were considered had a minimum radius of curvature in order to ensure reliability of the surface smoothing and this may have excluded many of the smaller grains. The sampling may therefore be biased towards the larger grains.

The three-dimensional curvature-velocity correlation results in Figure 6.25, being observed for the first time in a macroscopic sample are likely indicative of the enormous complexity introduced in a migrating grain boundary network due to the presence of common junctions such as triple lines and quad points. The issue of these additional geometric constraints is addressed at best in passing in existing simulation literature. As already alluded to in Chapter 4, this is further complicated in the case of impurities, where solute drag and boundary pinning is non-negligible. The fact that some boundaries display a negative correlation between curvature and velocity, seemingly contrary to the von Neumann-Mullins model, is further indication of the forces at play along junctions. As described in the dynamic theory in Chapter 5, the mean curvature is far from the only influence on boundary migration: there is the $\nabla \gamma$ term in the case of anisotropic energy, as well as the Herring force balance, all of which have a nontrivial effect. We speculate that grain growth in three dimensions

assumed to be driven by curvature alone without due regard to the geometry of the interface and the appropriate boundary conditions provides an incomplete picture. Incorporating all these effects into a simulation is a gargantuan task which is predicated upon knowing the grain boundary energy $\gamma(\Delta\omega, \hat{\boldsymbol{n}})$ and mobility $\mu(\Delta\omega, \hat{\boldsymbol{n}})$ function in the *entire* five-dimensional space of the grain boundary descriptors. This task is being addressed at the time of writing of this thesis using the theory developed in Chapter 5 and is a work in progress.

Chapter 8

Bibliography

[1] W. Kohl. *Handbook of Materials and Techniques for Vacuum Devices*. AVS Classics in Vacuum Science and Technology. American Inst. of Physics, 1997.

[2] W.. Ludwig, S. Schmidt, E. M Lauridsen, and H. F. Poulsen. X-ray diffraction contrast tomography: a novel technique for three-dimensional grain mapping of polycrystals. i. direct beam case. *J. Appl. Crystallogr.*, 41(2):302–309, 2008.

[3] G. Johnson, A. King, M. G. Honnicke, J Marrow, and W. Ludwig. X-ray diffraction contrast tomography: a novel technique for three-dimensional grain mapping of polycrystals. ii. the combined case. *J. Appl. Crystallogr.*, 41(2):310–318, 2008.

[4] Shiu Fai Li. Imaging of orientation and geometry in microstructures: Development and applications of high energy x-ray diffraction microscopy. PhD Dissertation, 2011.

[5] C. M. Hefferan. Measurement of annealing phenomena in high purity metals with near-field high energy x-ray diffraction microscopy. *PhD Dissertation*, 135., 2012.

[6] J. F. Lind. In-situ high-energy diffraction microscopy study of zirconium under uni-axial tensile deformation. *PhD Dissertation*, 301, 2013.

[7] U. Lienert, S.F. Li, C.M. Hefferan, J. Lind, R.M. Suter, J.V. Bernier, N.R. Barton, M.C. Brandes, M.J. Mills, M.P. Miller, B. Jakobsen, and W. Pantleon. High-energy diffraction microscopy at the advanced photon source. *JOM*, 63(7):70–77, 2011.

[8] S. F. Li and R. M. Suter. Adaptive reconstruction method for three-dimensional orientation imaging. *J. Appl. Crystallogr.*, 46(2):512–524, Apr 2013.

[9] B.E. Warren. *X-ray diffraction*. Addison-Wesley series in metallurgy and materials. Addison-Wesley Pub. Co., 1969.

[10] A.R. Verma and O.N. Srivastava. *Crystallography Applied to Solid State Physics*. Wiley Eastern Limited, 1991.

[11] M. Ladd and R. Palmer. *Structure Determination by X-ray Crystallography: Analysis by X-rays and Neutrons*. Springer US, 2014.

[12] C. M. Hefferan, S. F. Li, J. Lind, and R. M. Suter. Tests of microstructure reconstruction by forward modeling of high energy x-ray diffraction microscopy data. *Powder Diffr.*, 25:132–137, 6 2010.

[13] SF Li, J Lind, CM Hefferan, R Pokharel, U Lienert, AD Rollett, and RM Suter. Three-dimensional plastic response in polycrystalline copper via near-field high-energy x-ray diffraction microscopy. *Journal of Applied Crystallography*, 45(6):1098–1108, 2012.

[14] C. M Hefferan, J. Lind, S. F. Li, U. Lienert, A. D Rollett, and R. M Suter. Observation of recovery and recrystallization in high-purity aluminum measured with forward modeling analysis of high-energy diffraction microscopy. *Acta Materialia*, 60(10):4311–4318, 2012.

[15] J. Lind, A.D. Rollett, R. Pokharel, C. Hefferan, S.-F. Li, U. Lienert, and R. Suter. Image processing in experiments on, and simulations of plastic deformation of polycrystals. In *Image Processing (ICIP), 2014 IEEE International Conference on*, pages 4877–4881, Oct 2014.

[16] An K. Kanjarla R. A. Lebensohn S. F. Li P. Kenesei R. M. Suter A. D. Rollett R. Pokharel, J. Lind. Polycrystal plasticity: Comparison between grain - scale observations of deformation and simulations. *Annual Review of Condensed Matter Physics*, 5(1):317–346, 2014.

[17] C. A Stein, A. Cerrone, T. Ozturk, S. Lee, P. Kenesei, H Tucker, R. Pokharel, J Lind, C. Hefferan, R. M Suter, et al. Fatigue crack initiation, slip localization and twin boundaries in a nickel-based superalloy. *Current Opinion in Solid State and Materials Science*, 18(4):244–252, 2014.

[18] Anna Yershova and Steven M. LaValle. Deterministic sampling methods for spheres and $so(3)$, 2004.

[19] K Shoemake. Animating rotation with quaternion curves. *SIGGRAPH Comput. Graph.*, 19(3):245–254, July 1985.

[20] Leandra Vicci. Quaternions and rotations in 3-space: The algebra and its geometric interpretation, 2001.

[21] M. Groeber and M. Jackson. Dream.3d: A digital representation environment for the analysis of microstructure in 3d. *Integrating Materials and Manufacturing Innovation*, 3(1):5, 2014.

[22] S. Boyd and L. Vandenberghe. *Convex Optimization.* Cambridge University Press, 2004.

[23] G.B. Dantzig and M.N. Thapa. *Linear Programming 1: Introduction.* Springer Series in Operations Research and Financial Engineering. Springer New York, 2006.

[24] N. Karmarkar. A new polynomial-time algorithm for linear programming. *Combinatorica*, 4(4):373–395, 1984.

[25] G.B. Dantzig and M.N. Thapa. *Linear Programming 2: Theory and Extensions.* Springer Series in Operations Research and Financial Engineering. Springer New York, 2006.

[26] F. A. Potra and S. J. Wright. Interior-point methods. *Journal of Computational and Applied Mathematics*, 124(12):281 – 302, 2000. Numerical Analysis 2000. Vol. IV: Optimization and Nonlinear Equations.

[27] MJ McCready, E. Vassiliadou, and TJ Hanratty. Computer simulation of turbulent mass transfer at a mobile interface. *AIChE J.*, 32(7):1108–1115, 1986.

[28] T. McInerney and D. Terzopoulos. A dynamic finite element surface model for segmentation and tracking in multidimensional medical images with application to cardiac 4d image analysis. *Comput. Med. Imaging Graph.*, 19(1):69–83, 1995.

[29] H. et al. Lyklema. *Fundamentals of Interface and Colloid Science.* Academic Press, 2005.

[30] D. L. Olmsted, S. M. Foiles, and E. A. Holm. Survey of computed grain boundary properties in face-centered cubic metals: I. grain boundary energy. *Acta Materialia*, 57(13):3694 – 3703, 2009.

[31] D. L. Olmsted, E. A. Holm, and S. M. Foiles. Survey of computed grain boundary properties in face-centered cubic metalsii: Grain boundary mobility. *Acta Materialia*, 57(13):3704 – 3713, 2009.

[32] S. Ratanaphan, D. L. Olmsted, V. V. Bulatov, E. A. Holm, A. D. Rollett, and G. S. Rohrer. Grain boundary energies in body-centered cubic metals. *Acta Materialia*, 88:346 – 354, 2015.

[33] V. V. Bulatov, B. W. Reed, and M. Kumar. Grain boundary energy function for fcc metals. *Acta Materialia*, 65(0):161 – 175, 2014.

[34] D. M. Saylor, A. Morawiec, and G. S. Rohrer. The relative free energies of grain boundaries in magnesia as a function of five macroscopic parameters. *Acta Materialia*, 51(13):3675 – 3686, 2003.

[35] D. M. Saylor, A. Morawiec, and G. S. Rohrer. Distribution of grain boundaries in magnesia as a function of five macroscopic parameters. *Acta Materialia*, 51(13):3663 – 3674, 2003.

[36] D. M. Saylor, B. El Dasher, Y Pang, H. M. Miller, P. Wynblatt, A. D. Rollett, and Gregory S. R. Habits of grains in dense polycrystalline solids. *J. Am. Ceram. Soc.*, 87(4):724–726, 2004.

[37] J. Li, S. J. Dillon, and G. S. Rohrer. Relative grain boundary area and energy distributions in nickel. *Acta Materialia*, 57(14):4304 – 4311, 2009.

[38] A. H. King. Triple lines in materials science and engineering. *Scripta Materialia*, 62(12):889 – 893, 2010. Viewpoint set no. 46 Triple Lines.

[39] B. Bokstein, V. Ivanov, O. Oreshina, A. Peteline, and S. Peteline. Direct experimental observation of accelerated zn diffusion along triple junctions in al. *Materials Science and Engineering: A*, 302(1):151 – 153, 2001.

[40] T.P. Swiler, V. Tikare, and E.A. Holm. Heterogeneous diffusion effects in polycrystalline microstructures. *Materials Science and Engineering: A*, 238(1):85 – 93, 1997. Microstructure Evolution in Bulk Phases F.

[41] A D Rollett, R A Lebensohn, M Groeber, Y Choi, J Li, and G S Rohrer. Stress hot spots in viscoplastic deformation of polycrystals. *Modelling and Simulation in Materials Science and Engineering*, 18(7):074005, 2010.

[42] J.L.W. Carter, N. Zhou, J.M. Sosa, P.A. Shade, A.L. Pilchak, M.W. Kuper, Y. Wang, H.L. Fraser, M.D. Uchic, and M.J. Mills. *Characterization of Strain Accumulation at Grain Boundaries of Nickel-Based Superalloys*, pages 43–52. John Wiley & Sons, Inc., 2012.

[43] S-B Lee, G S Rohrer, and A D Rollett. Three-dimensional digital approximations of grain boundary networks in polycrystals. *Modelling and Simulation in Materials Science and Engineering*, 22(2):025017, 2014.

[44] G. Taubin. Curve and surface smoothing without shrinkage. In *Proceedings of the Fifth International Conference on Computer Vision*, ICCV '95, pages 852–, Washington, DC, USA, 1995. IEEE Computer Society.

[45] J. Wang and Y. Zeyun. A novel method for surface mesh smoothing: Applications in biomedical modeling. In BrettW. Clark, editor, *Proceedings of the 18th International Meshing Roundtable*, pages 195–210. Springer Berlin Heidelberg, 2009.

[46] E J Lieberman, A D Rollett, R A Lebensohn, and E M Kober. Calculation of grain boundary normals directly from 3d microstructure images. *Modelling and Simulation in Materials Science and Engineering*, 23(3):035005, 2015.

[47] A. J. Schwartz, M. Kumar, B. L. Adams, and D. P. Field, editors. *Electron Backscatter Diffraction in Materials Science*. Springer Science + Business Media, 2009.

[48] R. M. Haralick and L. G. Shapiro. *Computer and Robot Vision*. Addison-Wesley Longman Publishing Co., Inc., Boston, MA, USA, 1st edition, 1992.

[49] L. Lam, S-W Lee, and C. Y. Suen. Thinning methodologies-a comprehensive survey. *IEEE Trans. Pattern Anal. Mach. Intell.*, 14(9):869–885, September 1992.

[50] T. Y Kong and A. Rosenfeld, editors. *Topological Algorithms for Digital Image Processing*. Elsevier Science Inc., New York, NY, USA, 1996.

[51] S D Sintay and A D Rollett. Testing the accuracy of microstructure reconstruction in three dimensions using phantoms. *Modelling and Simulation in Materials Science and Engineering*, 20(7):075005, 2012.

[52] A. Khorashadizadeh, D. Raabe, S. Zaefferer, G. S. Rohrer, A. D. Rollett, and M. Winning. Five-parameter grain boundary analysis by 3d ebsd of an ultra fine grained cuzr alloy processed by equal channel angular pressing. *Advanced Engineering Materials*, 13(4):237–244, 2011.

[53] S. Ratanaphan, Y. Yoon, and G. S. Rohrer. The five parameter grain boundary character distribution of polycrystalline silicon. *J. Mater. Sci.*, 49(14):4938–4945, 2014.

[54] P. J. Frey and H. Borouchaki. Surface mesh quality evaluation. *International Journal for Numerical Methods in Engineering*, 45(1):101–118, 1999.

[55] R. E. Bank. *PLTMG: a software package for solving elliptic partial differential equations*, volume 7 of *Frontiers in Applied Mathematics*. Society for Industrial and Applied Mathematics (SIAM), Philadelphia, PA, 1990. Users' guide 6.0.

[56] MATLAB. *version 8.5 (R2015a)*. The MathWorks Inc., Natick, Massachusetts, 2015.

[57] F.J. Humphreys and M. Hatherly. Chapter 11 - grain growth following recrystallization. In F.J. HumphreysM. Hatherly, editor, *Recrystallization and Related Annealing Phenomena (Second Edition)*, pages 333 – 378. Elsevier, Oxford, second edition edition, 2004.

[58] A.P. Sutton and R.W. Balluffi. *Interfaces in Crystalline Materials*. Oxford Classic Texts in the Physical Sciences. OUP Oxford, 2006.

[59] G. Gottstein and L. S. Shvindlerman. *Grain Boundary Migration in Metals*, chapter Thermodynamics of Grain Boundaries, pages 1–109. Materials Science & Technology. CRC Press, 2009.

[60] J. F. Nye L. Bragg. A dynamical model of a crystal structure. *Proceedings of the Royal Society of London. Series A, Mathematical and Physical Sciences*, 190(1023):474–481, 1947.

[61] F. Stellacci and A. Mortensen. Materials science: Pleated crystals. *Nature*, 468(7326):906–907, Dec 2010.

[62] Q. H. Wei and X. L. Wu. Grain boundary dynamics under mechanical annealing in two-dimensional colloids. *Phys. Rev. E*, 70:020401, Aug 2004.

[63] J. von Neumann. Curvature driven grain growth in two dimensions. *American Society for Metals*, pages 108–118, 1952.

[64] W. W. Mullins. The statistical selfsimilarity hypothesis in grain growth and particle coarsening. *J. Appl. Phys.*, 59(4):1341–1349, 1986.

[65] W.W. Mullins. On idealized two dimensional grain growth. *Scripta Metallurgica*, 22(9):1441 – 1444, 1988.

[66] R. D. MacPherson and D. J. Srolovitz. The von neumann relation generalized to coarsening of three-dimensional microstructures. *Nature*, 446(7139):1053–1055, Apr 2007.

[67] H. Hadwiger. *Vorlesungen über Inhalt, Oberfläche und Isoperimetrie*. Springer, Berlin, 1957.

[68] D.A. Klain and G.C. Rota. *Introduction to Geometric Probability*. Lezioni Lincee. Cambridge University Press, 1997.

[69] D. W. Hoffman and J. W. Cahn. *A Vector Thermodynamics for Anisotropic Surfaces I. Fundamentals and Application to Plane Surface Junctions*, pages 289–292. John Wiley & Sons, Inc., 1972.

[70] D. W. Hoffman and J. W. Cahn. *A Vector Thermodynamics for Anisotropic SurfacesII. Curved and Faceted Surfaces*, pages 315–324. John Wiley & Sons, Inc., 1974.

[71] S. P. Chen, D. J. Srolovitz, and A. F. Voter. Computer simulation on surfaces and [001] symmetric tilt grain boundaries in ni, al, and ni3al. *J. Mater. Res.*, 4:62–77, 1989.

[72] O. A. Shenderova, D. W. Brenner, A. Omeltchenko, X. Su, and L. H. Yang. Atomistic modeling of the fracture of polycrystalline diamond. *Phys. Rev. B*, 61:3877–3888, Feb 2000.

[73] F. Sansoz and J.F. Molinari. Mechanical behavior of tilt grain boundaries in nanoscale cu and al: A quasicontinuum study. *Acta Materialia*, 53(7):1931 – 1944, 2005.

[74] J. A. Serret. Sur quelques formules relatives à la théorie des courbes à double courbure. *J. De Math*, 16., 1851.

[75] F. Frenet. Sur les courbes à double courbure, Thèse. *Toulouse. Abstract in J. de Math*, 17, 1852.

[76] David Kinderlehrer, Irene Livshits, and Shlomo Taasan. A variational approach to modeling and simulation of grain growth .

[77] C. Herring. *The Physics of Powder Metallurgy*. McGraw Hill, New York, 1951.

[78] G. Fekete. Rendering and managing spherical data with sphere quadtrees. In *Proceedings of the 1st Conference on Visualization '90*, VIS '90, pages 176–186, Los Alamitos, CA, USA, 1990. IEEE Computer Society Press.

[79] C.J. Bradley. *The Algebra of Geometry: Cartesian, Areal and Projective Co-Ordinates*. Highperception Limited, 2007.

[80] S. Patala and C. A. Schuh. Symmetries in the representation of grain boundary-plane distributions. *Philos. Mag.*, 93(5):524–573, 2013.

[81] F.C. Frank. Orientation mapping. *Metallurgical Transactions A*, 19(3):403–408, 1988.

[82] R. Lougee-Heimer. The Common Optimization INterface for Operations Research: Promoting open-source software in the operations research community. *IBM Journal of Research and Development*, 47(1):57–66, January 2003.

[83] GLPK (GNU linear programming kit), 2006.

[84] W. W. Mullins. Theory of thermal grooving. *J. Appl. Phys.*, 28(3):333–339, 1957.

[85] D.J. Allen. Thermal grooving at migrating grain boundaries. *Scripta Metallurgica*, 16(1):5 – 9, 1982.

[86] J. K. Mackenzie. Second paper on statistics associated with the random disorientation of cubes. *Biometrika*, 45(1/2):229–240, 1958.

[87] J.K. Mason and C.A. Schuh. The generalized mackenzie distribution: Disorientation angle distributions for arbitrary textures. *Acta Materialia*, 57(14):4186 – 4197, 2009.

[88] J. Goldfeather and V. Interrante. A novel cubic-order algorithm for approximating principal direction vectors. *ACM Trans. Graph.*, 23(1):45–63, January 2004.

[89] A. H. King and S. Shekhar. What does it mean to be special? the significance and application of the brandon criterion. *Journal of Materials Science*, 41(23):7675–7682, 2006.

[90] H. Beladi and G. S. Rohrer. The distribution of grain boundary planes in interstitial free steel. *Metallurgical and Materials Transactions A*, 44(1):115–124, 2013.

[91] H. Beladi and G. S. Rohrer. The relative grain boundary area and energy distributions in a ferritic steel determined from three-dimensional electron backscatter diffraction maps. *Acta Materialia*, 61(4):1404 – 1412, 2013.

[92] J. Gruber, D. C. George, A. P. Kuprat, A. D. Rollett, and G. S. Rohrer. *Mater Sci Forum 2004*. 2004.

[93] J.W Rutter and K.T Aust. Migration of 100 tilt grain boundaries in high purity lead. *Acta Metallurgica*, 13(3):181 – 186, 1965.

[94] R.C Sun and C.L Bauer. Measurement of grain boundary mobilities through magnification of capillary forces. *Acta Metallurgica*, 18(6):635 – 638, 1970.

[95] D.A. Molodov, U. Czubayko, G. Gottstein, and L.S. Shvindlerman. Mobility of 111 tilt grain boundaries in the vicinity of the special misorientation =7 in bicrystals of pure aluminium. *Scripta Metallurgica et Materialia*, 32(4):529 – 534, 1995.

[96] Samuel M. Allen and John W. Cahn. A microscopic theory for antiphase boundary motion and its application to antiphase domain coarsening. *Acta Metallurgica*, 27(6):1085 – 1095, 1979.

[97] Danan Fan and L-Q Chen. Computer simulation of grain growth using a continuum field model. *Acta Materialia*, 45(2):611–622, 1997.

[98] M. Upmanyu, D.J. Srolovitz, L.S. Shvindlerman, and G. Gottstein. Misorientation dependence of intrinsic grain boundary mobility: simulation and experiment. *Acta Materialia*, 47(14):3901 – 3914, 1999.

[99] A.J Haslam, S.R Phillpot, D Wolf, D Moldovan, and H Gleiter. Mechanisms of grain growth in nanocrystalline fcc metals by molecular-dynamics simulation. *Materials Science and Engineering: A*, 318(12):293 – 312, 2001.

[100] M Upmanyu, DJ Srolovitz, LS Shvindlerman, and G Gottstein. Molecular dynamics simulation of triple junction migration. *Acta materialia*, 50(6):1405–1420, 2002.

[101] D Weygand, Y Bréchet, J Lépinoux, and W Gust. Three-dimensional grain growth: a vertex dynamics simulation. *Philosophical Magazine B*, 79(5):703–716, 1999.

[102] M Syha and D Weygand. A generalized vertex dynamics model for grain growth in three dimensions. *Modelling and Simulation in Materials Science and Engineering*, 18(1):015010, 2009.

[103] C.E. Krill-III and L.-Q. Chen. Computer simulation of 3-d grain growth using a phase-field model. *Acta Materialia*, 50(12):3059 – 3075, 2002.